MAGNETO-THERMAL CONDUCTIVITY OF INDIUM ANTIMONIDE

by

Parviz Fozooni B.Sc.,M.Sc.

Department of Physics

Bedford College

University of London

A thesis submitted in partial fulfilment of the requirements for the degree of Doctor of Philosophy at the University of London.

April 1980

ABSTRACT

Measurements of the lattice thermal conductivity of indium antimonide ($n = 10^{14}$ to 10^{17} and $p = 10^{15}$ to 10^{17} cm^{-3}) single crystal samples have been performed in the temperature range of 1.2 to $10^{o}K$, and for the lower temperatures in magnetic fields up to 40 KG. A new 8-bit microprocessor controlled system was constructed to make fully automatic measurements under optimised conditions. This enabled thermal conductivity measurements to be made to an accuracy of 2% absolute and 0.1% relative. The zero field results are in good agreement with theory and with previous measurements.

The thermal conductivity of the p-InSb decreased with increase of magnetic field. The acceptor ground state is four fold degenerate and the thermal phonons could only be scattered by transition within the quartet of energy levels. It was found that Ge doped sample ($p = 2.8 \times 10^{15}$ cm^{-3}) at $1.23^{o}K$ exhibited a broad minimum when the field reached about 40 KG which was due to the first order Zeeman splitting of the acceptor ground state.

Quantum oscillations of thermal conductivity of highly doped n-type samples were observed in a magnetic field. The period of oscillation was the same as the Shubnikov-de Haas oscillation of electrical conductivity and it is shown that the oscillation occurs because the electron-phonon interaction oscillates with magnetic field as the Fermi level crosses successive Landau levels.

TABLE OF CONTENTS

Table of Contents (cont'd)

Table of Contents (cont'd)

LIST OF TABLES

LIST OF FIGURES

List of figures (cont'd)

List of figures (cont'd)

ACKNOWLEDGEMENT

The author wishes to express his most sincere gratitute to Dr.R.A.Mansfield for his active assistance and guidance throughout the course of this research.Warmest thanks and gratitute are offered to Dr.H.Tokumoto for his continuing advice and enlightening discussion.Thanks to Mr.A.K.Betts for the construction of the digital control system.The assistance of all the technical staff in the department of physics at Bedford College is gratefully acknowledged.

CHAPTER 1

Introduction

The purpose of this investigation is to extend the measurement of the thermal conductivity of indium antimonide single crystal (n, p-type) in magnetic fields up to the extreme quantum limit, and to determine the scattering mechanisms which are affected by the magnetic field.

Previous measurements of the thermal conductivity of InSb and other III-V compounds, with varying amounts of impurities, in zero magnetic field were reported by Geballe[1], Challis et al[2,3], Holland[4], Kosarev et al[5,6] and by Grenier[7]. Similar measurements by Carruthers et al[8] on pure and doped specimen of Germanium offer also interesting points of comparison. The first basic observation is that the lattice thermal conductivity below the conductivity maximum is sensitive to the excess carrier concentration. The effect of the carriers is to act as scattering centres for phonons. Their own contribution to the heat current being negligible for the doping levels and temperature range considered here. The second observation is that for InSb the introduction of excess carriers has a much greater effect in p-type speciments than in n-type specimens. This was investigated by Challis et al[3] who found that the thermal conductivity of five n-type specimens (tellurium-doped) covering the range 3.8×10^{14} - 4.0×10^{18} carriers/cm^3 varies by a factor of about 2.5 while that of 6-p-type specimens (germanium-doped) covering the range 6.7×10^{14} - 4.5×10^{17} carriers/

cm^3 changes by a factor of more than 10. In this regard it is interesting to note that Kosarev[6] has offered a new model for the scattering of phonons by charged carriers in the field of a charged impurity, and shown that in semiconductors with a small effective mass, for example n-InSb, this mechanism of scattering would not be very effective. The zinc blend lattice for the III-V compounds consists of two fcc sub-lattices, formed with atoms of group V and group III elements, respectively. The basic difference between this lattice and the diamond lattice of the group IV semiconductors is the absence in this case of the inversion symmetry. Another fundamental difference between the III-V compounds and the elemental semiconductors is the crystal binding. X-ray diffraction experiments have shown that, for InSb, there is a charge transfer of -0.45e, indicating that negative charge is being passed from the Sb atom to the In atom; therefore the binding is partially polar and polar scattering will play an appreciable role in transport properties, limiting the carrier mobility because the relative motion of the 2 different atoms causes a polarization of the crystal, and a strong interaction with the carriers may result. The III-V compounds have band structures of the same type as the group IV semiconductors though there are some differences which arise from the lack of inversion symmetry in the compounds.

The conduction band structure varies considerably from compound to compound. Experiments show that the minimum of the conduction band in InSb lies at the centre

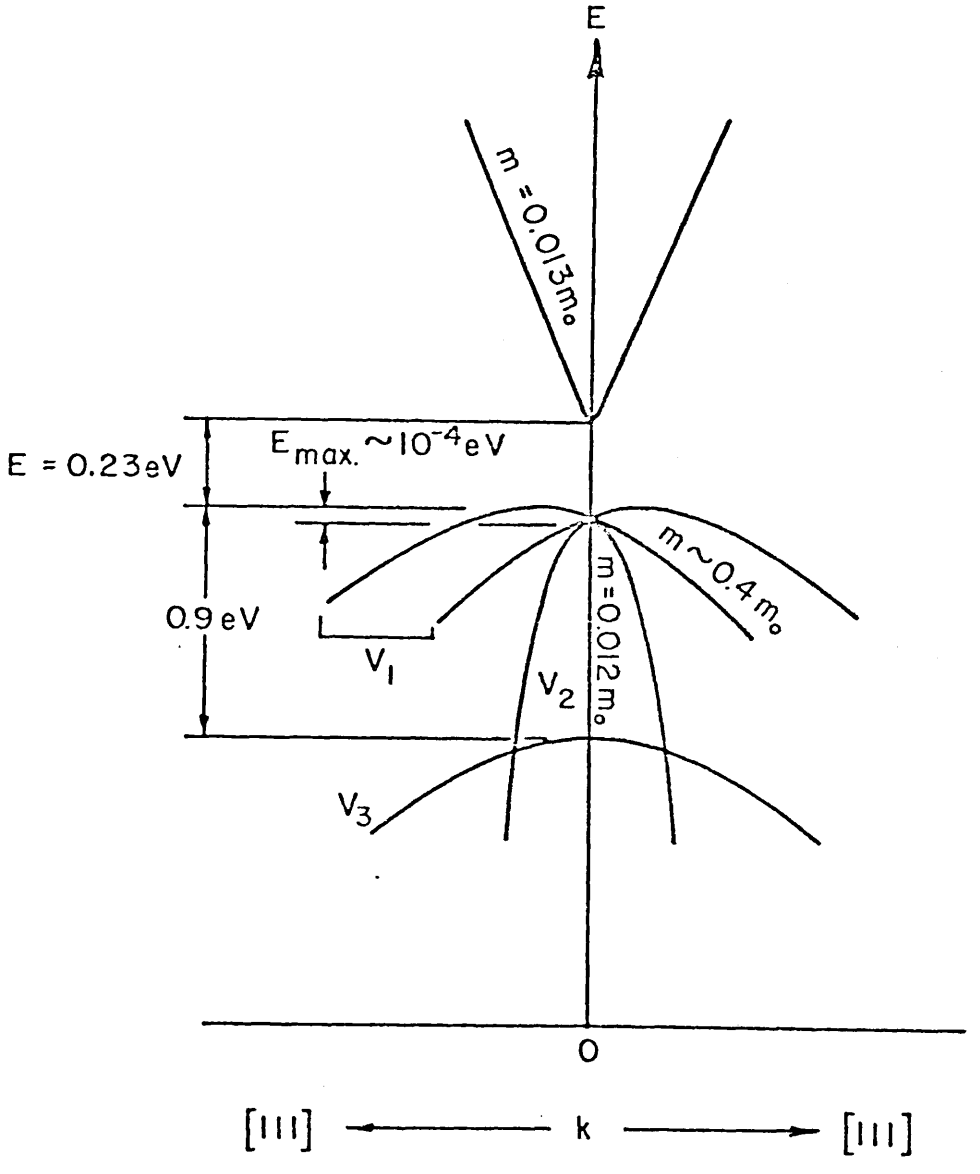

Figure 1. Band structure of InSb (From reference 10).

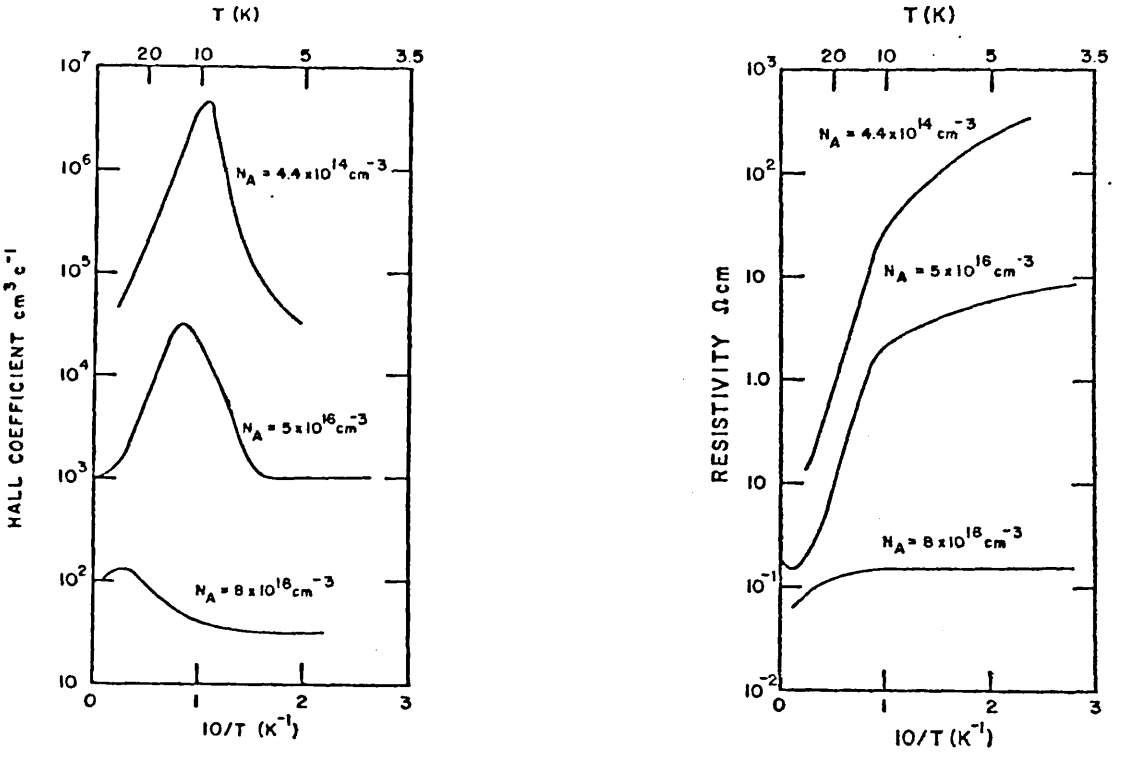

Figure 2.Hall constant and electrical resistivity of P-InSb versus reciprocal temperature.

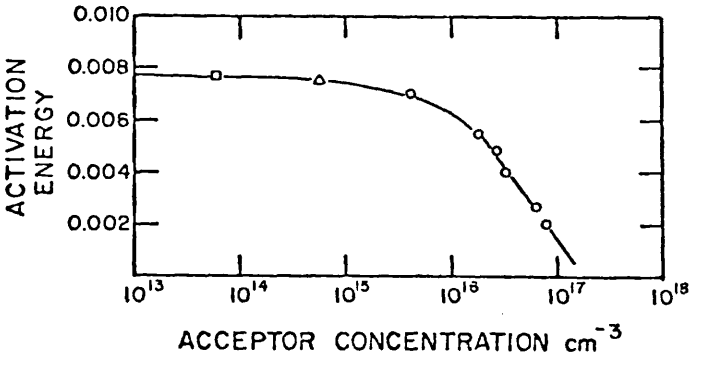

Figure 3.Ionization energy of acceptor impurities versus acceptor concentration(From reference 10).

of the zone and that the band is spherically symmetrical. There is a high curvature at the minimum, giving a very small effective mass for electrons at the bottom of the band, but the band is non-parabolic, the curvature decreasing rapidly with increasing energy[10], see Fig. (i).

Concerning the valence band, which is also important for the present work, detailed quantitative information is unfortunately not as precise as for the conduction band. The experimental results appear to be consistent with a valence band structure like that of Ge or Si in its general features. The theoretical work on InSb suggests, as shown in Fig. (1), the existence of 3 bands, a heavy-hole band, V_1, a ligh-hole band, V_2, degenerate with V_1 at K = 0 and a band V_3 split off by spin-orbit coupling. There is still some doubt about the value of the effective masses of heavy hole in InSb. It appears, on the present evidence, that the most probable value of the effective mass of heavy holes at low temperatures is more than $0.4\ m_o$[11]. Our use of this value at helium temperature is questionable. The maxima of the heavy-hole band lie slightly away from the centre of the zone, probably on the III axes. Kane[12] has calculated that these maxima lie at about 0.3% of the distance to the zone boundary and at about 10^{-4} eV above the energy at k = 0. The hole effective masses are not isotropic and this "warping" may have noticeable effects on some transport properties like longitudinal magneto-resistence. The energy gap between the conduction and valence bands is $E = 0.23$ eV at $T = 0K$.

Isolated acceptors in InSb have levels that lie above the top of the valence band. From the variation of Hall coefficient with temperature, Putley deduced an activation energy of about 0.008 eV in specimens containing Zn or Cd impurities. At acceptor concentration greater than about 10^{15} cm^{-3} there is appreciable interaction between the impurities and p-type InSb containing more than this number of impurities shows behaviour typical of impurity band conduction. Fig (2) shows that as the temperature is reduced, the contribution to the conductivity from the carriers in the impurity band increases relative to that from the carriers in the valence band; the Hall coefficient passes through a maximum, and below this point the resistivity ceases to rise rapidly as the temperature is lowered. Because of the smaller effective mass of holes in InSb, impurity band conduction occurs at lower impurity concentrations than in Ge, though the ground state of shallow acceptors in InSb are four fold degenerate as in Ge or Si. At acceptor concentrations greater than about 10^{17} cm^{-3} it merges with the valence band, This is shown in Fig. (3).

The measurements of magnetothermal conductivity of p-type Ge and Si[13] revealed the linear Zeeman effect of the acceptor ground stae for Si and recent investigation of thermal conductivity[14] and ultrasonic attenuation[15] under high magnetic field suggested a second order Zeeman splitting of the quartet in Ge. The effect observed from magnetothermal conductivity of p-InSb was very similar to that of Si but the minimum of the reduced thermal conductivity (K_H/K_0) occurred at a higher field. This

could be due to a smaller g factor for acceptor states in InSb than in Si.

In n-type InSb the effective mass m* is small and the dielectric constant large, so that for a hydrogen-like model of a donor centre the activation energy

$$E_D = \frac{m^*}{m} K^{-2} \text{ Ry} = 0.7 \text{ meV}$$

where Ry = 13.6 eV, $\frac{m^*}{m} = 0.0138$ and K = 16. At the same time the Bohr radius is very large and as a result the donor centres for a band of levels which overlap the bottom of the conduction band. This is the case for doping level down to less that 10^{15} cm^{-3}. Consequently even at the lowest temperature free carriers are present. When a magnetic field is applied Yafet, Keyes and Adams[17] have shown that the hydrogen-like donor centres have activation energy which increases with the field causes the overlap of the band to be lifted and this is magnetic freeze-out of the electrons.

N_D greater than 5×10^{15} cm^{-3} indium antimonide is degenerate up to the highest fields present and the effect of the magnetic field is to change the distribution of energy levels in the conduction band. Sub-bands of Landau levels are produced as and the magnetic field is increased successive Landau levels pass through the Fermi level according to the expression

$$E_F = (n + \tfrac{1}{2}) h \omega_c$$

where n = 0, 1, 2,... and ω_c is the cyclotron frequency. This causes oscillations in those properties which depend on the free electrons such as de Haas-van Alphen, Shubnikov-de Haas effects. Oscillation would occur in the electron

contribution to the thermal conductivity but, as already mentioned, this contribution is negligible compared to the lattice conductivity for doping levels up to 10^{18} cm^{-3}. Oscillation can occur, however in the free electron scattering of the phonons which may cause a small oscillation in the total sensitivity if the electron-phonon contribution to the thermal sensitivity becomes observable.

The present work was principally aimed at resolving the following questions:

1. Is the theory of Suzuki and Mikosiba[18] for zero field scattering by the acceptor quartet valid for p-InSb and whether the acceptor ground state splits under magnetic field or not?

2. How strong the electron-phonon interaction in n-InSb is, and whether the oscillatory effect of electrical conductivity in a magnetic field can be observed for thermal conductivity despite the weak coupling of electrons with phonons?

And also to achieve the accuracy necessary to solve these problems a fully automatic system has been developed. This led to an improved understanding of the zero magnetic field conductivity.

CHAPTER 2

A Review of Thermal Conductivity

2.1 Introduction

The thermal conductivity K in an isotopic solid is given by the relation:

$$\vec{Q} = -K \overrightarrow{\text{grad}}\, T$$

where $\vec{Q}$ represents the rate of flow of heat across unit cross-section perpendicular to $\vec{Q}$, T is the temperature. When there are no free electrons, heat is transmitted by phonons, which are the quanta of energy in each mode of vibration, and the mean free path is a measure of the rate at which energy is exchanged between different phonon modes. By analogy with kinetic theory the thermal conductivity of solids can be analysed using the expression:

$$K = \tfrac{1}{3} C v \ell$$

where C is the heat capacity contributed by the lattice, v is the velocity of sound and ℓ is the phonon mean free path. When an excess of phonons is generated at the hot end they diffuse to the cold end . However, if the harmonic approximation was exactly valid, and the crystal was perfect, there would be no resistance to the heat flow and thermal conductivity would be infinite. It is necessary to introduce anharmonic forces, or imperfections or both to obtain a finite thermal conductivity. Thus the study of lattice thermal conductivity is of considerable importance for the study of anharmonic effects.

The phonon mean free path ℓ is determined principally by two process; geometrical scattering and scattering by other phonons. In the low temperature range the interaction

of phonons by phonons is negligible, but the geometrical effects and imperfections are important in limiting the mean free path. Now if we generalize the mean free path to $\ell = v(q,\lambda)t(q,\lambda)$ where v is the velocity of phonons and $t(q,\lambda)$ is the relaxation time for the phonon (q,λ) in which q is the wave vector and λ is the polarization of the phonons. If there are several types of excitation, K is the sum of a contribution from each. If the mean free path is limited by several scattering processes the effective mean free path is given by $\ell^{-1} = \sum_J \ell_J^{-1}$. If the specific heat per normal phonon mode is given by C_{Ph} and we add up the contribution due to each mode we obtain the total specific heat as follows:

$$C = \sum_\lambda \int_q C_{Ph}\, dq$$

Now, by substituting for phonon mean free path and the total specific heat in the equation $K = \frac{1}{3}Cv\ell$ the following general form for thermal conductivity is obtained:

$$K = \tfrac{1}{3}\left(\frac{1}{2\pi^2}\right)\sum_\lambda \int_o^{\omega_\lambda} v(q,\lambda)\, C_{Ph}(\omega,\lambda)\, \left[v(q,\lambda)t(q,\lambda)\right] \frac{\omega^2 d\omega}{v^3(q,\lambda)} .$$

In the above equation the frequency and wave vector have been related in the Debye approximation for low wave vector by $\omega = qv$, and have assumed an isotopic phonon spectrum. At the lowest temperature range when there is just boundary scattering (ℓ=const) K changes as T^3 ($C \simeq T^3$).

Now consider the effect of doping on the thermal conductivity. The thermal conductivity of doped III-V compounds is altered as the impurity content is changed. As the impurity content is increased, the maximum thermal conductivity is depressed, so that in the lower temperature range the drop of thermal conductivity is considerable.

When the phonon mean free path in the impure specimens is much less than the size of the specimen, there is considerable variation both in magnitude and functional behaviour of the K vs T.

In the interpretation and analysis of the lattice thermal conductivity we follow Callaway's[19] phenomenological theory in which it was assumed that all phonon scattering processes can be represented by relaxation times which are functions of frequency and temperature. It was also assumed that there is isotropy in the phonon spectrum and the dispersion in the vibrational spectrum is neglected. The expression given for thermal conductivity is:

$$K = \frac{k}{6\pi^2}\left(\frac{kT}{\hbar}\right)^3 \sum_{t=1}^{3} \frac{1}{v_t} \int_0^{\frac{\Theta}{T}} \tau_t \frac{x^4 e^x}{(e^x - 1)^2}\, dx \qquad (2.1)$$

in which the specific heat per normal phonon mode is considered:

$$C_{Ph}(x) = \frac{kx^2 e^x}{(e^x - 1)^2}$$

where $x = \frac{\hbar\omega}{kT} = \frac{\hbar vq}{kT}$. q is the magnitude of the phonon wave vector, k and $\hbar$ are the Boltzman and Planck constants respectively and v is sound velocity. In expression (2.1) τ is a combined relaxation time considering the boundary scattering, normal three phonon process, impurity and charge-carrier phonon scattering and Θ is the Debye temperature (Θ for InSb is 208K[20]). At low temperature the upper limit of integration Θ/T is large and can be taken as infinity.

The phonon relaxation time t can be obtained from the principle of additivity of the resistive scattering

relaxation frequencies $\tau^{-1} = \sum_j \tau_j^{-1}$ and the scattering mechanisms which are common for dielectric crystals are as following: phonon-phonon, isotops and impurities, charge-carriers and boundary scattering. These will be explained briefly here and more detailed treatment of those most relevant to the system under study will be given elsewhere.

2.2 Phonon-Phonon Scattering

Phonons interact with one another because of the anharmonic nature of the lattice forces and due to this interaction the energy is exchanged between different modes. The simplest type of phonon scattering is the three phonon process which in term is distinguished into three types of Normal and Umklapp process. In Normal process two phonons collide to produce a single phonon in which both energy and momentum is conserved and the direction of the energy does not alter. Peierls[21] pointed out that the important three-phonon processes for thermal conductivity are not of the form of N-process, but are of the form of U-process in which the momentum is destroyed and the direction of energy flow changes. Thus U-processes provide thermal resistance to phonon flow and can thermalize a phonon distribution. At low temperatures, only the regions of momentum space close to the centre of the Brillouin zone remain heavily populated with phonons; yet a U-process cannot occur unless the total wave vector of the two phonons extend beyond the zone boundary. According to Peierls the probability of U-process would fall off as

$\exp(-\Theta_D/2T)$ at low temperatures where Θ_D is the Debye temperature. This is quite different from the low temperature probability of N-processes, which should fall off as T^5 well below Θ_D. The phonon-phonon interaction term for thermal conductivity employed by Callaway[19] is

$$\tau_P^{-1} = B\omega^2 T^3$$

where B is a constant which can be calculated.

Kosarev[5] argued that the above expression is valid only in the extreme case of $\hbar w \ll kT$ for the longwave phonons.

Below the conductivity maximum ($T = 10^oK$) where the subthermal and thermal phonons are scattered by boundaries, only superthermal phonons $\hbar\omega \gg kT$ participate in phonon-phonon processes and different relaxation times should be considered. Slonimski[35] considered a scattering frequency for longitudinal phonons as

$$\tau_\ell^{-1} = B_\ell x^5 T^5$$

And the expression for transverse phonons in which

$$\vec{q}_{t1} + \vec{q}_{t2} \leftrightarrows \vec{q}$$

are the most efficient processes has been found by Orbach et al[36] as

$$\tau_t^{-1} = B_t x^5 T^5 \exp\left(\frac{v_t - v_\ell}{v_t + v_\ell} x\right)$$

When expressions τ_ℓ^{-1} and τ_t^{-1} are used, the temperature range where normal phonon-phonon processes remain efficient is widened and the temperature where boundary scattering is effective shifts toward lower temperature.

2.3 Phonon-Boundary Scattering

The scattering relaxation frequency due to crystal boundaries and surface dislocation τ_b^{-1} is described by a constant which is the ratio of the velocity of sound to Casimir's length Λ and is given by:

$$\tau_b^{-1} = b = \frac{v_s}{\Lambda}$$

where $\Lambda = \sqrt{\frac{4}{\pi} l_1 l_2}$ l_1, l_2 are dimensions of the cross-section of the crystal and it is assumed that the sample's walls are perfectly rough, so that the scattering is perfectly diffused and phonons are not specularly reflected. The sample is also considered to be long enough, so that there is no scattering from end-faces, and v_s is the average phonon velocity taking into account one longitudinal and two transverse modes according to:

$$\frac{3}{v_s} = \frac{1}{v_\ell} + \frac{1}{v_{Ft}} + \frac{1}{v_{st}}$$

where $v_\ell = 3.835 \times 10^5$ cm/sec, $v_{Ft} = 2.335 \times 10^5$ cm/sec and $v_{st} = 1.68 \times 10^5$ cm/sec as measured by heat pulse experiments[22].

Casimir assumed that walls of the sample acted as diffuse scatterers of phonons, i.e. a phonon striking the surface of the crystal would be reradiated with random direction. However, in general, one expects that a certain fraction of the phonons will be specularly reflected. It has been shown[23] that this effect increases the conductivity by a factor $\frac{(1 + P)}{(1 - P)}$, where P varies with the surface condition and may also depend upon temperature. The variation with temperature occurs because with decreasing temperature the average phonon wavelength

increases and consequently a surface of given roughness appears smoother. Thus the phonon mean free path is increased. Berman et al. shows that Λ should be changed by $\Lambda(2 - f)/f$ where f, the roughness parameter, is the fraction of the phonons which are diffusely scattered. In the low temperature region, where boundary scattering dominates (ℓ constant), the specific heat C changes as T^3 so that thermal conductivity also varies as T^3.

2.4 Impurity Scattering

In between the two extremes of high and low temperatures where phonon-phonon and boundary scattering dominate respectively the conductivity achieves a maximum and scattering by defects in the crystal like dislocations and isotopic impurities become important. The extent of this type of scattering determines the height of the maximum in the conductivity. The impurity scattering frequency τ_i^{-1} is somewhat complex and can be considered as the sum of terms

$$\tau_i^{-1} = \tau_{iso}^{-1} + \tau_{im}^{-1} + \tau_{ir}^{-1} + \tau_k^{-1} + \tau_{is}^{-1}$$

The first three terms are Rayleigh-type scattering, i.e. proportional to the fourth power of phonon frequency, which is

$$\tau_i^{-1} = A\omega^4$$

where A is the constant of proportionality. More specifically, τ_{iso}^{-1} and τ_{im}^{-1} are the mass-difference scattering due to isotope and impurities substitution and combined τ_i^{-1} for mass-difference scattering is given by

$$\tau_i^{-1} = v\Gamma\omega^4/4\pi v^3 = A_m\omega^4$$

where

$$\Gamma = \sum_{x,y\ldots} \left(\frac{x}{x+y+z+..}\right)\left(\frac{M_A}{\overline{M}}\right)^2 \Gamma(A) + \left(\frac{y}{x+y+z+..}\right)\left(\frac{M_B}{\overline{M}}\right)^2 \Gamma(B) + \ldots$$

$$\Gamma(A) = \sum_i f_i \left(\frac{\Delta M_i}{\overline{M}_A}\right)^2$$

For the compound $A_x B_y C_z \ldots$, v is the molecular volume, and

$$\overline{M} = \frac{xM_A + yM_B + zM_C + \ldots}{(x + y + z + ..)}$$

Here the molecule is InSb and the summation is carried over all the kinds of molecules AB formed by the different isotope and impurity atoms.

The other Rayleigh-type scattering term τ_{is}^{-1} is a strain scattering caused by force-constant difference and volume difference[26] associated with the impurities.

$$\tau_{is}^{-1} = A_s\omega^4 = \frac{v}{2\pi N^2}\sum_i N_i \left(\frac{\Delta F}{F} - \frac{4\Delta V}{V}\right)_i^2$$

where N_i is the number of i-type impurities and $\Delta F/F$ and $\Delta V/V$ are, the added stress and added dilatation introduced by the impurity. The addition of A_s, for which there is not sufficient information to calculate, may account for part of the discrepancy between the experimentally determined value A and calculated value for A_M.

A resonance scattering term τ_{ir}^{-1} was formulated by Pohl[27] and is

$$\tau_{ir}^{-1} \propto \frac{\omega^2 T}{(\omega_o^2 - \omega^2)^2 + (\Omega/\pi)^2\omega^2\omega_o^2}$$

where ω_o is the resonance frequency and Ω describes damping of the resonance may modify the simple Rayleigh-type behaviour, but its effect is expected in a temperature

range higher than the range measured here, and therefore will not be considered.

Keyes[28] proposed a resonance-like bound electron-phonon process:

$$\tau_k^{-1} \alpha \omega^4 \left[\omega^2 - (4\Delta/\hbar)^2\right]^{-2} \left[1 + a^{*2}\omega^2/4v^2\right]^{-8}$$

where a* is the effective radius of the localized state and Δ is the chemical shift related to the splitting of electronic states.

In summary, the impurity scattering frequency τ_i^{-1} can be approximated by a Rayleigh term $\tau_i^{-1} = A\omega^4$. The deviation from this simple behaviour due to τ_{ir}^{-1} and τ_k^{-1} will be neglected.

2.5 Charge Carrier-Phonon Scattering

The electron-phonon interaction concerns transport properties which involve the flow of electricity and of heat. Concerning the effect of the charge carriers-phonon interaction in thermal conductivity Challis[3] et al showed that the thermal conductivity of indium antimonide of p-type samples is much less than that of n-type with the same concentration of the charge carriers. The analysis of thermal conductivity revealed that the effect of doping impurities could not be explained just by the ordinary Rayleigh-type scattering of phonons by point defects[29]. In consequence a number of theoretical papers have been presented to deal with phonon scattering with charge carriers. Ziman[30] derived the relaxation time for scattering of phonons by the free charge carriers in a more heavily doped semiconductors where wave functions

of carriers are markedly overlapped and also they are contained in a parabolic isotopic band. The scattering frequency is of the form

$$\tau_{e-Ph}^{-1} = \frac{m^{*2}c^2\eta_{l,t}^2 kT}{2\pi\rho v\hbar^4} \ln \frac{1+\exp\left\{(kT)^{-1}\left[\frac{1}{2}\hbar qv-(\hbar^2/8m)(4k_F^2-q^2)\right]\right\}}{1+\exp\left\{(kT)^{-1}\left[-\frac{1}{2}\hbar qv-(\hbar^2/8m)(4k_F^2-q^2)\right]\right\}}$$

where m^* is the effective mass, c deformation potential, ρ crystal density, and $\eta_{l,t}$ is the cosine of the angle between $\vec{q}$ and the polarization vector $\vec{e}_q$ of longitudinal or transverse phonons averaged over the solid angle:

$$\eta_{l,t}^2 = \frac{1}{4\pi}\int (\vec{q}_{l,t}\cdot\vec{e}_{q_{l,t}})^2 \frac{d\Omega}{q^2}$$

In τ_{e-Ph}^{-1} the logarithmic part is considered as a cut off function which takes account of the fact that not every phonon can be scattered. In Ziman's theory the effectiveness of phonon-electron interaction is limited by the laws of conservation of energy and momentum. When the electron is scattered from a state characterized by a vector $\vec{k}$ to a state characterized by $\vec{k}'$, with $\vec{k}' = \vec{q} + \vec{k}$, the limit $q \ll 2k_F$ is set on $\vec{q}$ owing to the upper limit k_F taken by both $\vec{k}'$ and $\vec{k}$. When the above theory is applied to p-InSb with proper adjustment of parameters a relatively good fit is obtained. However at the low temperature end the result is not satisfactory and according to Kosarev[6] the limit of $\vec{q} \leqslant 2\vec{k}_F$ is responsible for the inadequacy of the theory. If the field of the ionized impurity, in which the interaction of the phonons with carriers take place is taken into account, this violates the condition for the closure of the carrier-phonon system which leads to a lifting of the limitation $\vec{q} \leqslant 2\vec{k}_F$. A

similar situation is known in optics: Absorption of light by free carriers in semiconductors within the limit of one band is possible only in the presence of interaction of carriers with phonons or impurities[31]. Pyle[32] considered processes of second order of perturbation theory, namely virtual absorption and emission of phonons:

$$\vec{k} + \vec{q} \rightarrow \vec{k}' \rightarrow \vec{k}'' + \vec{q}'.$$

And as far as the energy is not conserved in the intermediate state which in consequence lifts the limitation $\vec{q} < 2\vec{k}_F$. However, Pyle's theory is not consistant with experiment at lower temperature, though it was an improvement over that of Ziman in terms of physical realism. Suzuki et al[33] considered the phonon scattering by holes within the four fold degenerate acceptor states which is in rather good agreement with experiment. Electron-phonon interaction will be described in more detail elsewhere.

CHAPTER 3

Experimental Details

3.1 Samples

Rectangular parallel piped samples of Tellerium doped single crystal of InSb were used. Samples B, C have dimensions 1 x 2 x 25mm and samples D, E are 2 x 2 x 25 and 1 x 2 x 17mm with the $(11\bar{1})$ axis perpendicular to within five degrees of the large face which were cut and supplied by Royal Radar Establishment. Two slices of p-type InSb, Ge doped were obtained from M.C.P. The X-ray photographs, for these slices, Fig. (4) shows the $(\bar{1}11)$ axis is perpendicular to the large face. The bar shaped samples were cut using spark erosion with a gap voltage kept at the minimum of 50 volts to minimize the depth of the damage to the crystal surface. Samples were polished after cutting using 5 micron alumina powder to remove the damaged area. They were cut in such a direction that the (110) axis is parallel to the long axis or along the heat current and applied magnetic field. Two p-type samples F and G have dimensions 2 x 2 x 25mm and all samples were etched by cp4 etchant for 3 seconds as final treatment and washed in pure water for 2¼ hours. Carrier concentrations of the samples varied between $10^{14}cm^{-3}$ to $10^{17}cm^{-3}$ and are given in the following table.

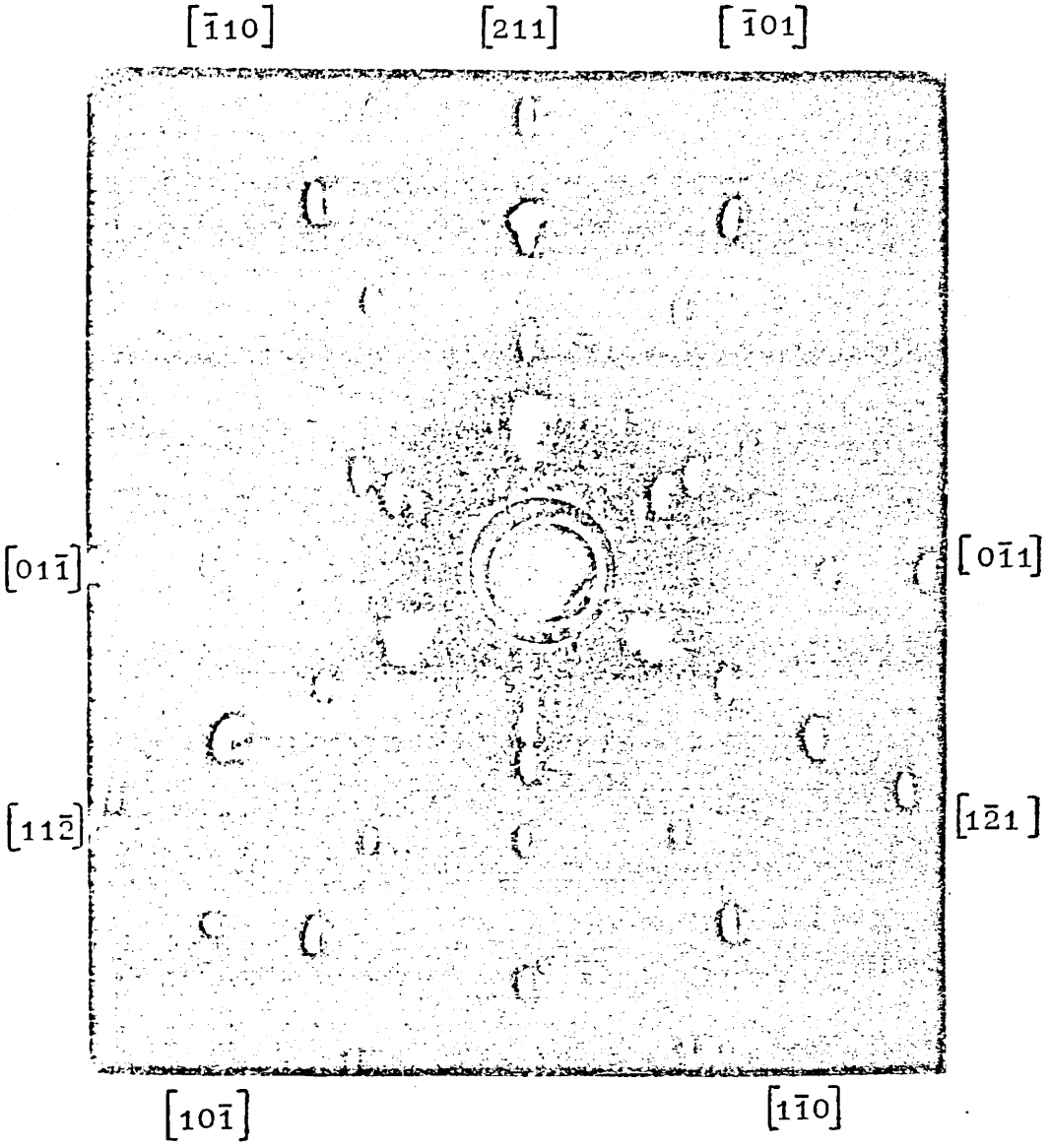

Figure 4. X-ray photograph in the direction [111] perpendicular to the large face of sample F.

Sample	n, p = cm^{-3}	k_F cm^{-1}	77K		E.P.D.cm^{-2}
			μ cm^2/v sec	ρ ohmcm	
B	$n = 3.5 \times 10^{14}$	2.08×10^5	365000	0.056	1000
C	$n = 4.4 \times 10^{15}$	5.07×10^5			
D	$n = 3.5 \times 10^{16}$	1.01×10^6			
E	$n = 1.2 \times 10^{17}$	1.53×10^6			
F	$p = 2.8 \times 10^{15}$	4.38×10^6	6500	0.34	100
G	$p = 2.4 \times 10^{17}$	1.92×10^6	1049	0.025	1000

(Table I)

3.2 Cryostat

To cover the temperature range from 1.3°K to 10°K a new cryostat was designed and built. Since most of the measurements were made in a magnetic field, it was essential to make the cryostat as versatile as possible to carry out the experiments in the desired temperature range and also in the magnetic field. Fig. (5) represents a block diagram of the system.

A stainless steel cryomagnetic system made by Oxford Instruments, which was originally used for a He^3 cryostat, was available so the cryostat was build to fit in this equipment. Unfortunately, in order to accomodate thermometers used to measure the specimen temperature outside the magnetic field, the He^4 pot had to be raised which reduced the volume available for liquid He and it was necessary to transfer He during each run.

The cryostat was similar to the one described by Challis et al[13] and is shown in figures (6) and (7). Note

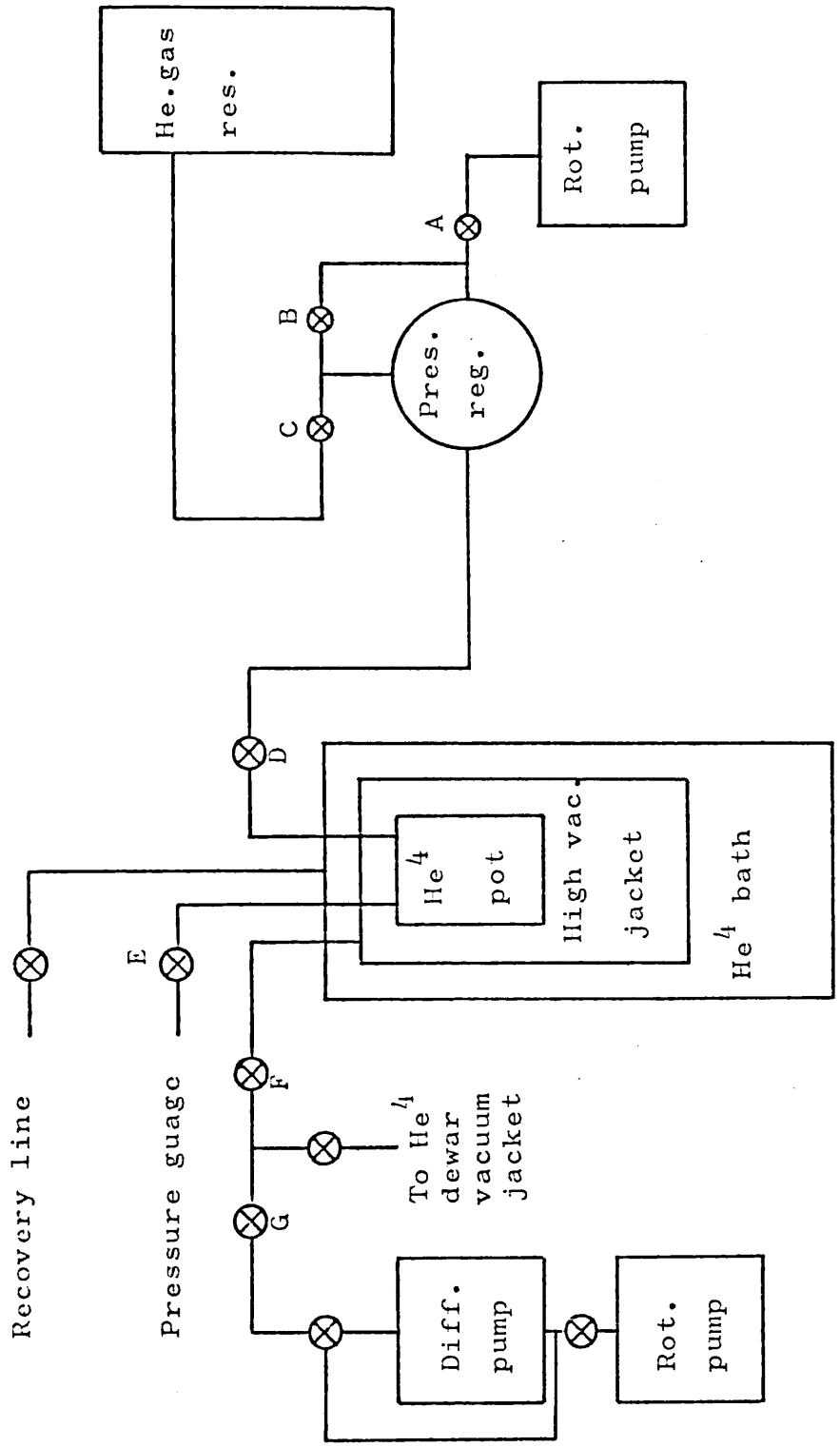

Figure 5. A block diagram of the system

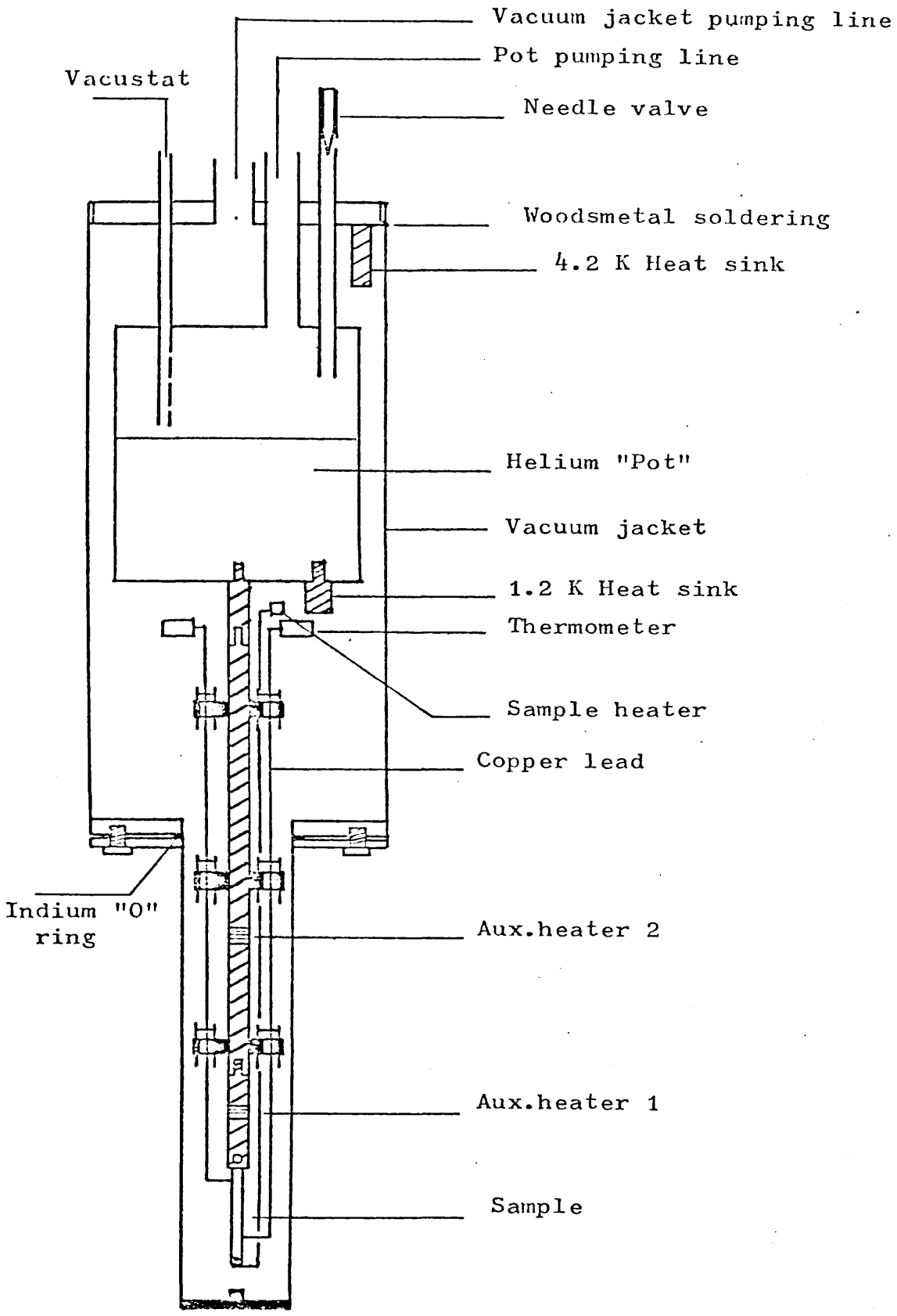

Figure 6.Schematic diagram of the cryomagnetic system.

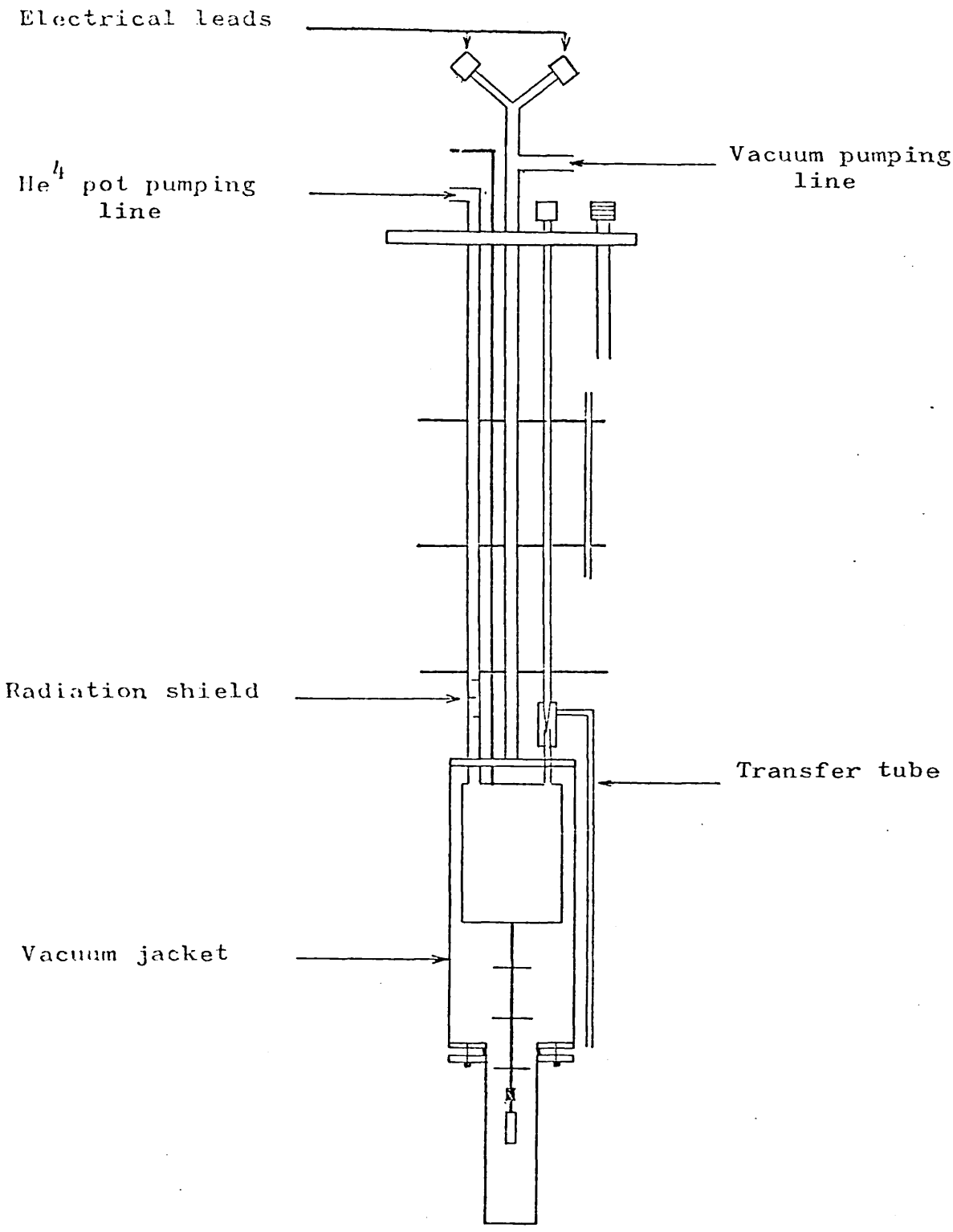

Figure 7. Schematic diagram of He^4 pot and sample holder of the cryomagnetic system.

that the specimen chamber had a demountable O-ring indium seal which provided easy access to the specimen. The temperature of the He^4 pot could be controlled by a manostat shown in figure (8) which controlled accurately the pumping speed so that the vapour pressure in and hence the temperature of the pot was constant. This device made it possible to vary the ambient temperature of the specimen without having to use electrical heating with its consequent rapid evaporation of the liquid helium.

The lead wires from room temperature to the $4.2^{o}K$ heat sink were 44 gauge enamel copper wire running in the tube used for pumping on the vacuum jacket. After the $4.2^{o}K$ heat sink super-conducting wires were used and glued to the wall of helium pot using 7031 GE varnish and finally anchored at $1.2^{o}K$ on the bottom of the pot.

In order to make measurements in the magnetic field and also at temperatures higher than $4.2^{o}K$, a copper rod with brass rings soldered along it was prepared, and could be screwed into the copper plate of the helium pot, see Fig. (9).

Copper wire (22 gauge) was used to link the thermometers and the sample heater with the sample. To avoid vibration of these wires, which could directly increase the noise level, the wires were fastened by very thin nylon thread to the stainless steel pegs on each brass ring. Two auxillary heaters were wound in a bifilar manner on the main copper rod to control the temperature at any point.

3.3 Thermometry

Thermal conductivity measurements were made in two different ranges, 1.2 to $4.2^{o}K$ and 4.2 to $10^{o}K$.

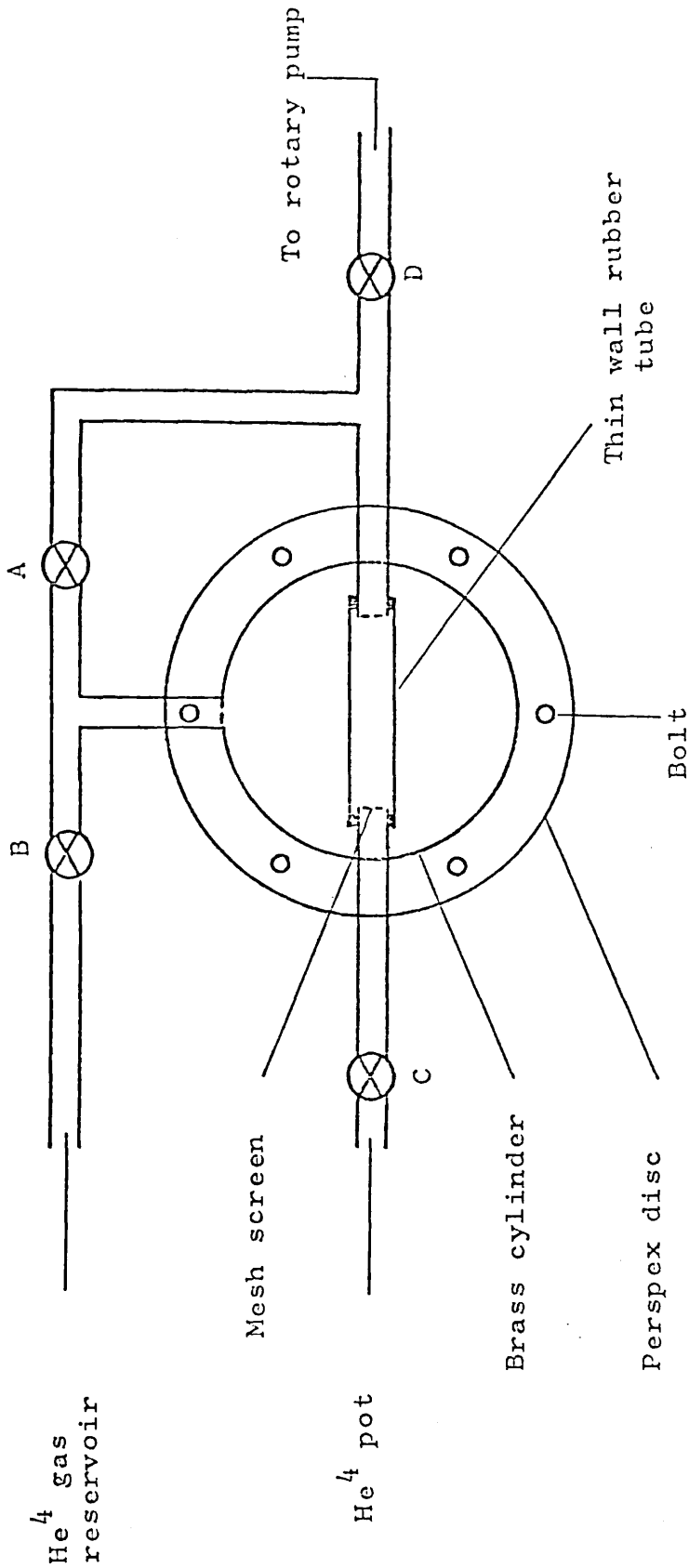

Figure 8. Schematic diagram of the pressure controller.

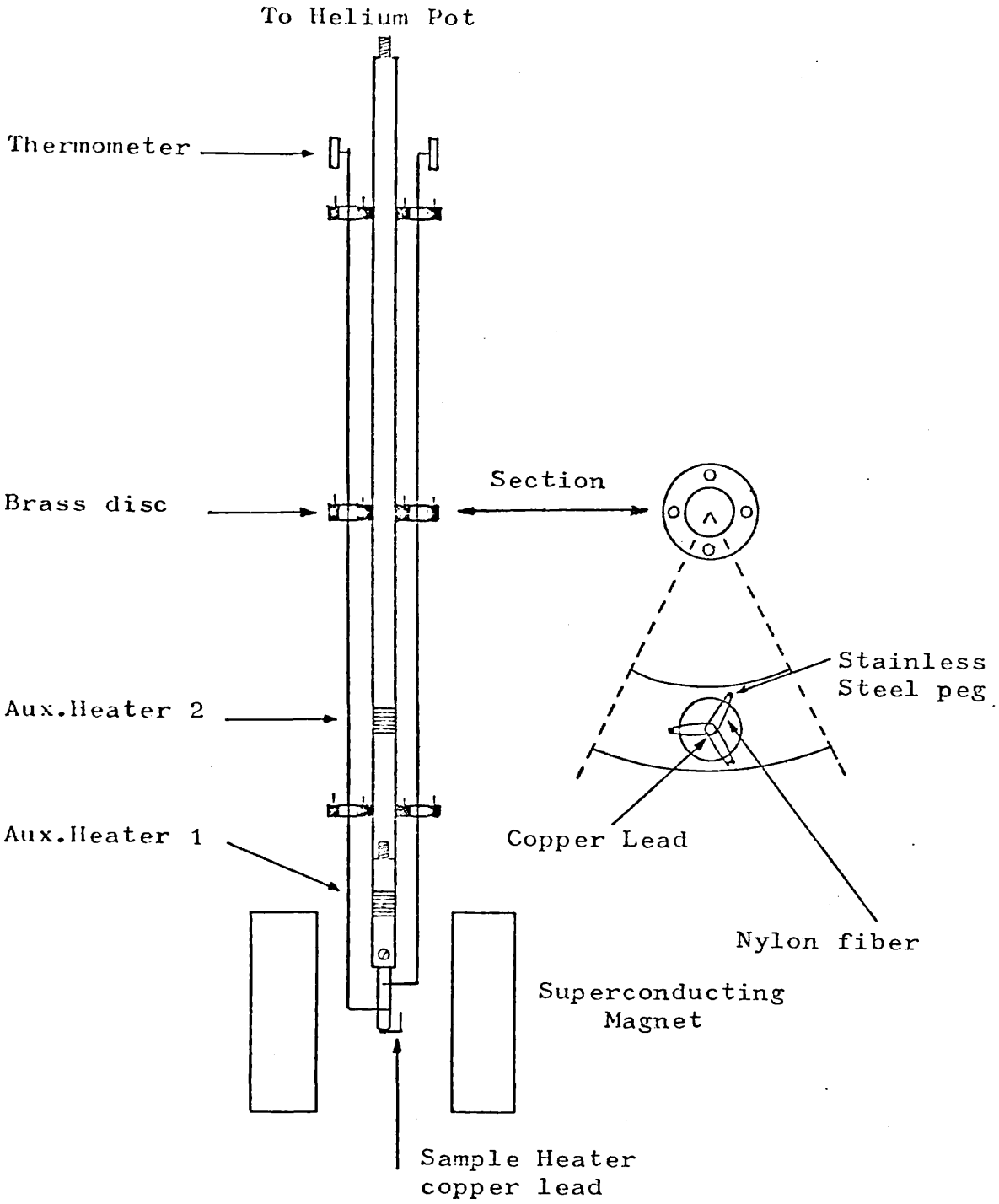

Figure 9.Sample holder and the mounting rig.

Two Allen-Bradby carbon resistors were used for the measurements of temperature difference along the sample. These two thermometers were calibrated for each run against a calibrated carbon-glass thermometer and the calibration was checked at some temperatures using the vapour pressure of the liquid helium in the helium pot. Thermometers of this type usually have characteristics which differ slightly from each other. Each curve changes very little and usually settles down to a good reproducible curve with variation of less than 0.2%. Below $4^{o}K$ two 100 ohm Allen-Bradby carbon resistors were used. These had a value about 1000 ohms at $4.2^{o}K$ and never exceeded $32K\Omega$ at $1.2^{o}K$. The following function with 9 coefficients was found, by the method of a least square fit, to provide a satisfactory fit:-

$$\ln T = \sum_{n=0}^{8} . A_n (\ln R)^n \qquad (1)$$

The following values were obtained for coefficients A_n,

For R_1:

A_0 =	0.666447102E-09	A_5 =	0.172426990E-01
A_1 =	0.267339213E+01	A_6 =	-0.226398666E-02
A_2 =	-0.257156912E+00	A_7 =	0.136558185E-03
A_3 =	0.432210316E-03	A_8 =	-0.316885985E-05
A_4 =	-0.510109185E-01		

And for R_2:

A_0 =	0.237516136E-10	A_5 =	0.180617012E-02
A_1 =	-0.201702624E+02	A_6 =	-0.357484999E-02
A_2 =	0.144081482E+02	A_7 =	0.279232813E-03
A_3 =	-0.367897957E+01	A_8 =	-0.703505158E-05
A_4 =	0.374559714E+00		

Fig. (10) shows the experimental points of R_1 and R_2 vs T and illustrates the good fit with the solid line obtained from equation (1) and the above coefficients.

As will be shown in the next section, the computation of ΔT the temperature drop across the sample which leads to calculation of thermal conductivity, depends directly on the values of the thermometers' slope $(\frac{dR}{dT})$ and not on the resistance of them. So according to equation (1) the slope of the characteristic curve R = R(T) and also second derivative $(\frac{d^2R}{dT^2})$ of each thermometer was calculated and are shown below:

$$\frac{dR}{dT} = \frac{R}{T} \cdot \frac{1}{\sum_{n=1}^{8} nA_n (\ln R)^{n-1}}$$

and

$$\frac{d^2R}{dT^2} = \frac{(\frac{dR}{dT})^2}{R} \cdot \left[1 - \sum_{n=1}^{8} nA_n (\ln R)^{n-1} - \frac{\sum_{n=2}^{8} n(n-1)A_n (\ln R)^{n-2}}{\sum_{n=1}^{8} nA_n (\ln R)^{n-1}} \right]$$

The second derivative of the resistance with respect to temperature was used only in correcting terms. In the temperature range of the experiment the good matching of the two thermometers R_1 and R_2 can be judged by the following criterion:

$$\left| \frac{\frac{dR_1}{dT} - \frac{dR_2}{dT}}{\frac{dR_2}{dT}} \right| \leqslant 0.008$$

For the measurement above $4^{\circ}K$ two 220 ohms A - B resistors were used. These two were calibrated simply against the C - G thermometers for each run. The resistance of 220

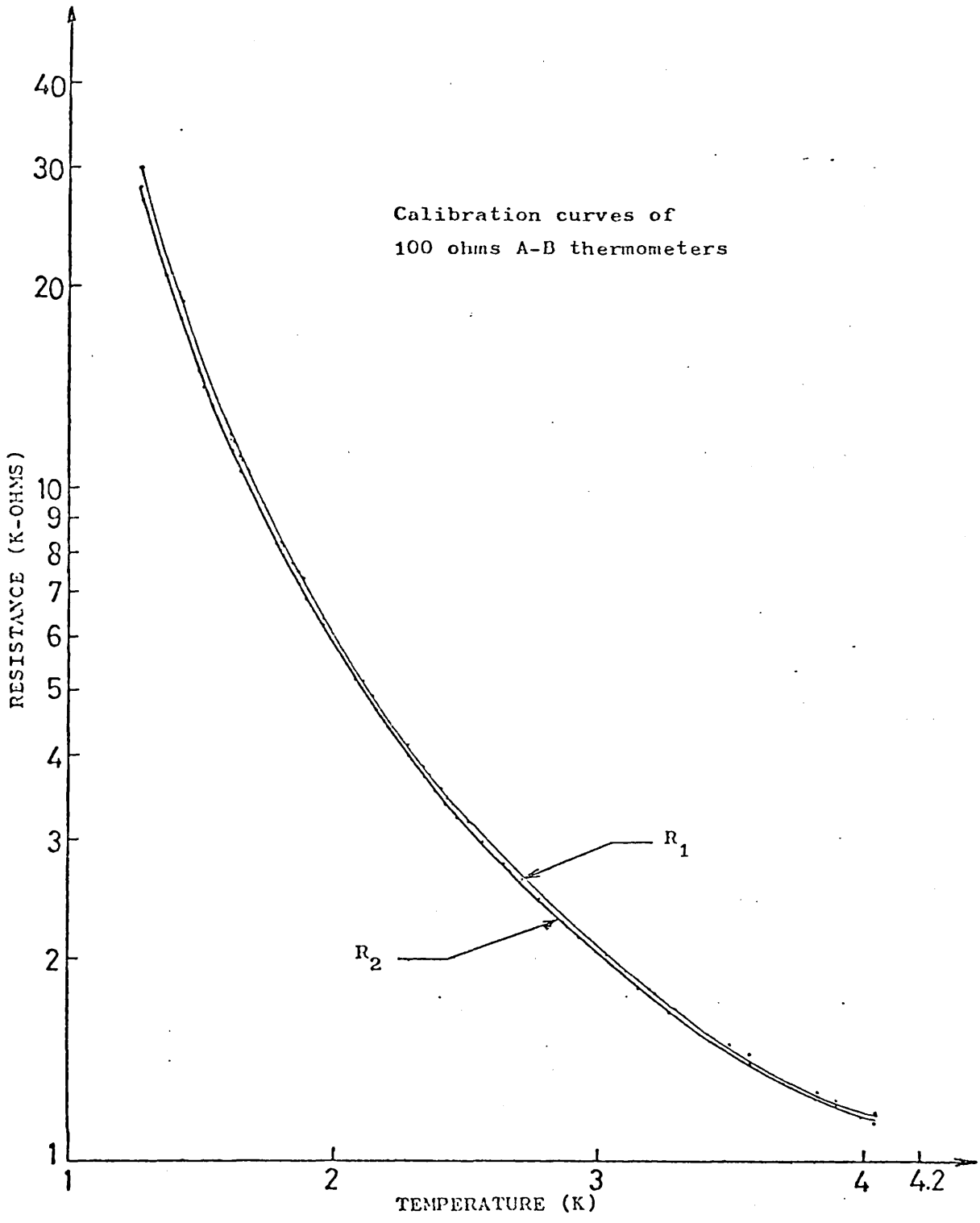

Figure 10. Calibration curves of two 100 ohms Allen-Bradley thermometers.

ohms A - B increases very rapidly below $3^{o}K$ so this type of thermometer is only suitable for measurements above $4^{o}K$. Calibration curves for R_1' and R_2' are given in Fig. (11).

3.4 Computer Controlled System

The measurements of thermal conductivity were made fully automatically by means of a Microprocessor Calculating Unit (MPU) and a Digital Controller.

The system consisted of a Keithley System One and a digital control system. The latter was designed and built in the college electronics workshop[34]. Binary codes from the MPU were decoded into specific commands which were sent to the various control devices.

The Keithley System One consisted of the following:

(a) Programmable Calculating Unit (787-21)

(b) Control Unit (780)

(c) Ten channel scanner (702/7029)

(d) Digital voltmeter 174

(e) Digital output (1722) for DVM 174

(f) Interface (7801-1722) in slot # 1 of CU (780)

The programme which was loaded into the calculating unit was executed and proper commands through the control unit were transmitted to different parts of the system. The scanner was capable of scanning ten different channels. The sensitivity of the DVM 174 was 100nV.

The Digital Controller was a combination of the following devices:

(a) two different digital temperature controllers

(b) two constant current units

(c) four external circuit controllers

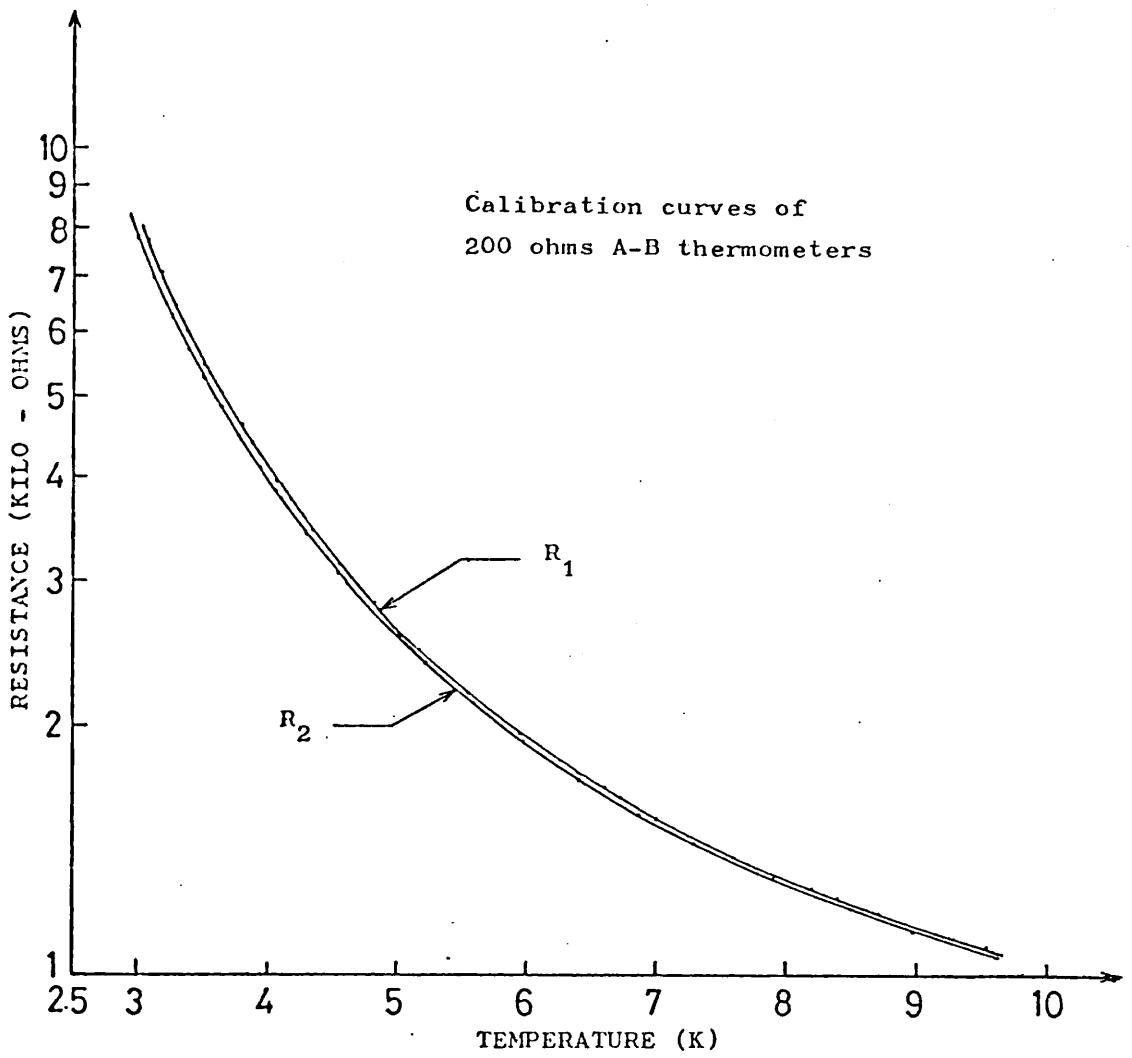

Figure 11. Calibration curves of two 200 ohms Allen-Bradley thermometers.

(d) interface and decoder

(e) function selector.

This system was designed to be fully automatic, but any function could be over iden by the manual control keyboard. The two digital temperature controllers were different in design and use. The output of the first one was connected to an auxillary heater (a) and the second one was used only to create a heat gradient through the sample for thermal conductivity measurements. A block diagram of this system is shown in Fig. (12). Each part will be discussed in details in the following:

3.4.1 Main Digital Temperature Controller

The temperature of the cryostat was monitored by the MPU and could be changed or kept constant according to the programme loaded into it, by means of a digital temperature controller, see Fig. (13). The logic circuit consisted of two 4-bit up/down counters (SN74193) in cascade, and 8-bit data storage latch (SN74116) and two 4-bit data selectors (SN74157).

The functioning of all these elements was controlled entirely by the MPU via an Interface Module which decodes the various commands (i.e. load up/down counter, select latch, etc.) and sends specific control signal to the appropriate device. To reach a desired temperature quickly an 8-bit latch was used to set the initial heating or cooling rate in larger steps compared to that of the counters. When this temperature was reached the output control was shifted from the latch to the counters. This could be done by sending two Control and Data Bytes by the MPU to the temperature

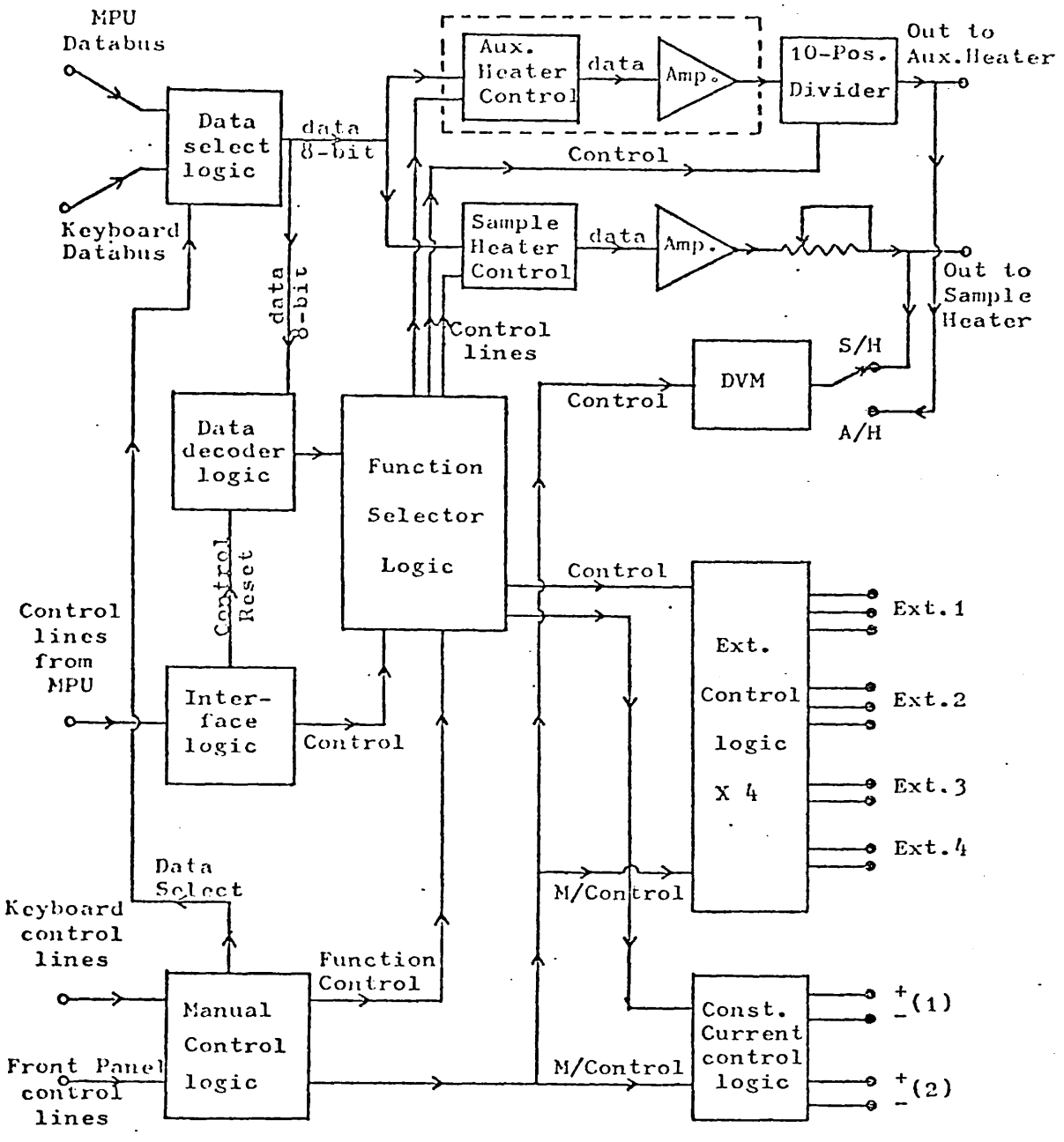

Figure 12. A block diagram of the computer controlled system.

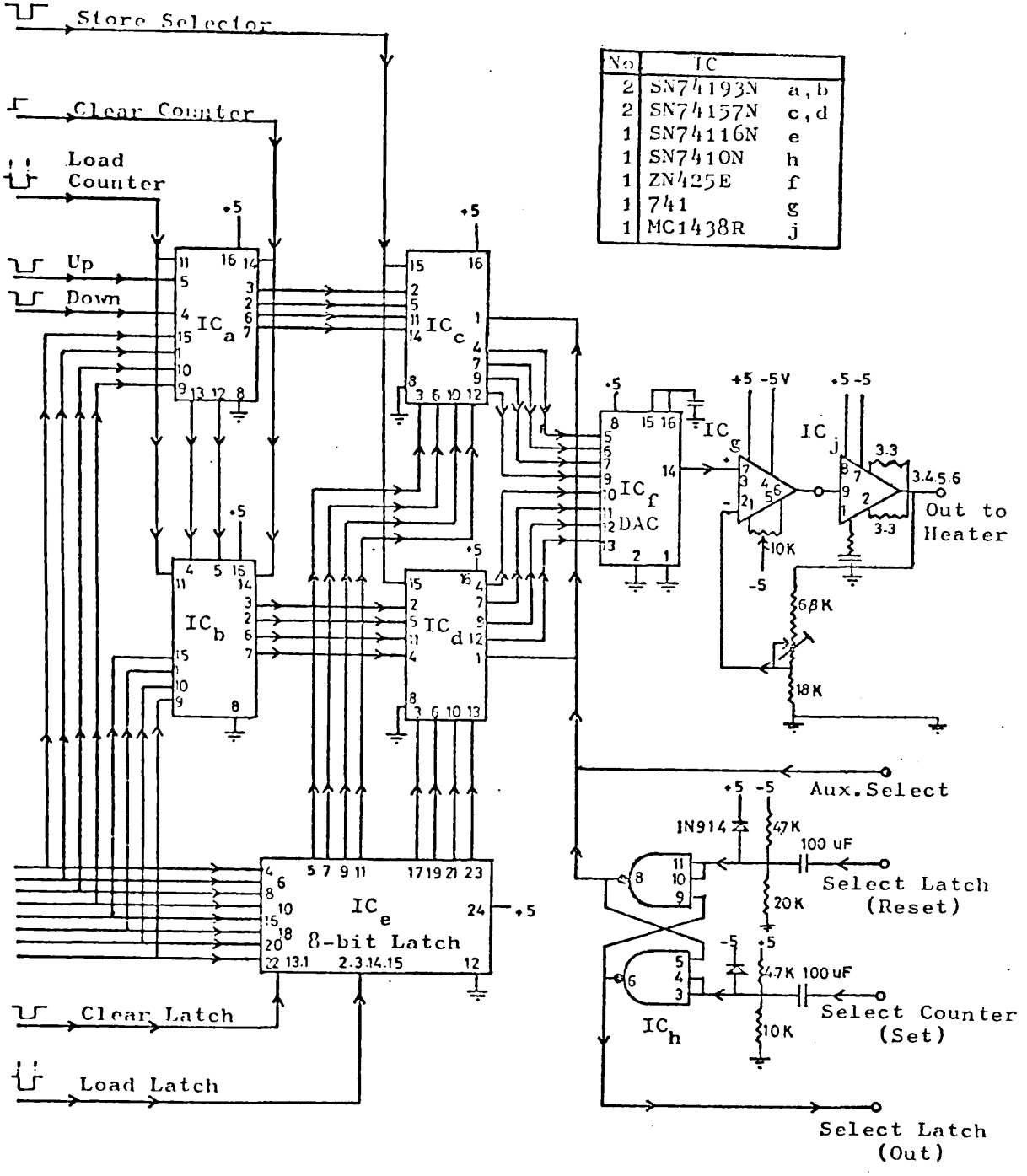

Figure 13. Circuit diagram of the digital temperature controller.

controller unit. The Control Byte (CB) selects the device which controls the output current, the Data Byte (DB) carries the desired value of the heater current. The last DB for the latch would be considered as first DB for the counters after the output control is taken over by the counter which from now on will receive only one step up/down (ten times smaller from the latch) commands for better stability. Using 8-bit logic gives only a resolution of 1/256 in the output current and to improve on this a ten position divider was used in the output circuit (not shown) which was again controlled by the MPU. This gave a resolution of 1/2560 which is like using a 12-bit logic system. The output section which was controlled by the logic section consisted of a DAC(ZN415E), an operational amplifier and a current divider IC. The operational amplifier was used to buffer the DAC output and at the final stage could provide up to 300mA at 3.5 volts. The command codes to control the temperature controller are as the following:

Function	BCD code	Octal code	Output on control unit
Temp. controller OFF	11	821	00010001
" ON	12	822	00010010
load latch	13	823	00010011
clear latch	14	824	00010100
select latch	15	825	00010101
load counter	16	826	00010110
clear counter	17	827	00010111
select counter	18	830	00011000
count up	21	841	00100001
count down	22	842	00100010
advance divider	23	843	00100011
reset divider	24	844	00100100

3.4.2 Sample Heater Controller

In thermal conductivity measurements a very stable power supply is required to create a constant temperature gradient through the sample. Since in a large temperature range different heat gradients are needed, the output of the power supply must be controlled. This was done by a digital circuit similar to the temperature controller explained in the previous section. Since up/down counters were not used the circuit is simpler, see Fig. (14). Using this arrangement helped for optimizing thermal conductivity data by receiving proper CB and DB from MPU changing the heat current through the sample creating different temperature drop across the specimen while the temperature of the cryostat was kept constant.

Another facility available in this section of the system was, the current through the sample heater could be reversed. Since at very low temperature the applied heat to the sample was small the thermal emf could result in a large error in heat measurements, and the only way to eliminate thermal emf was to reverse the current and then use the mean value. The current reversal command was sent to the sample heater controller by the MPU after registering the current and voltage across the sample heater in normal positions. The chosen value for the heater current was determined by the programme according to temperature to optimize the thermal conductivity. The command codes are as follows:

Function	BCD code	Octal code	Output on control unit
sample heater OFF	31	861	00110001
" " ON	32	862	00110010
load latch	33	863	00110011
clear latch	34	864	00110100
reverse current	35	865	00110101

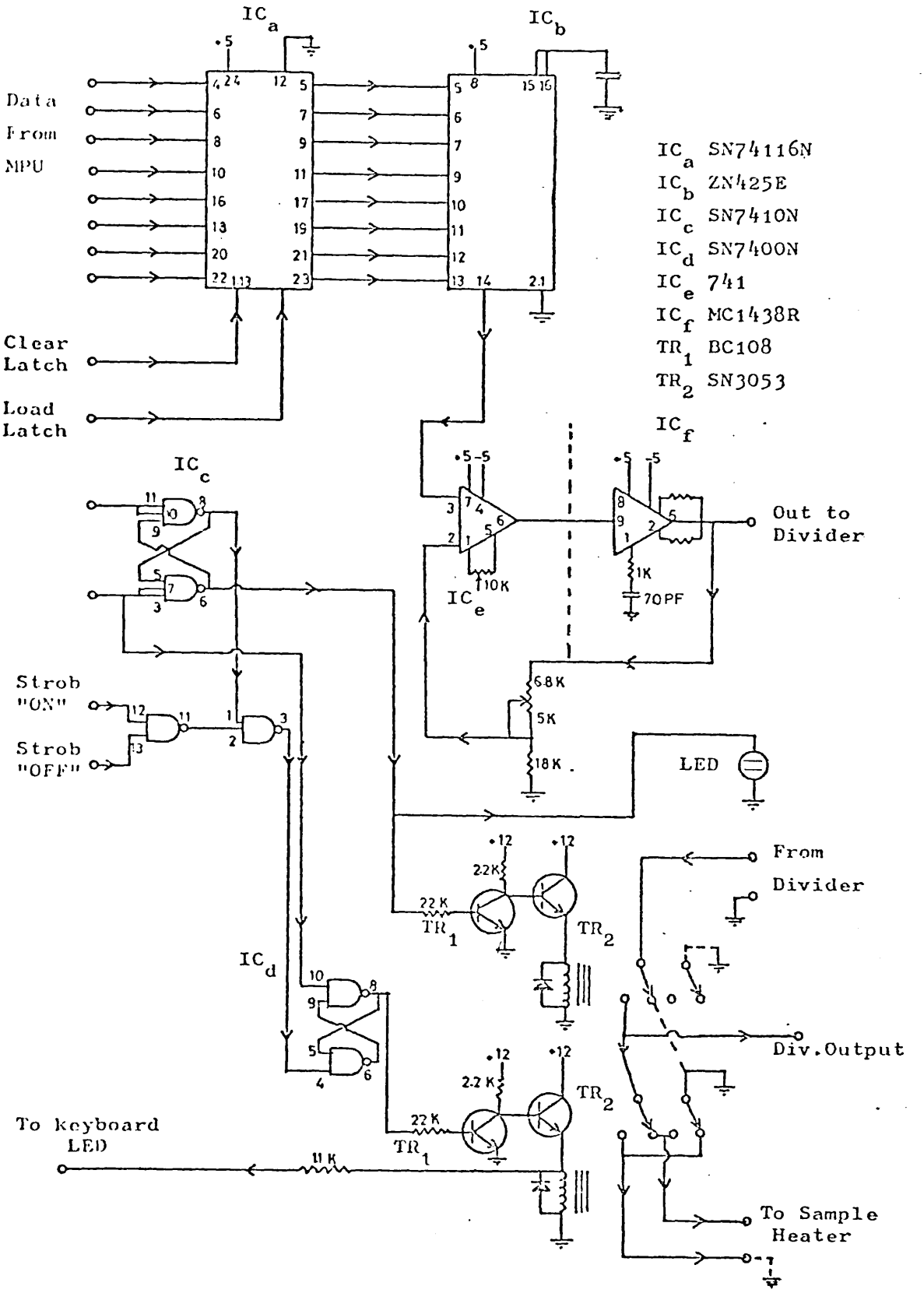

Figure 14. Circuit diagram of the sample heater controller.

3.4.3 Constant Current Unit

The thermometers were supplied by two constant current units, see Fig. (15). The circuit consisted of two digital and analogue parts. The logic circuit which controlled the analogue power supply contained just four IC's for both units. Two adjustable ranges had to be preselected manually. However the reverse switches on each these two units were controlled both manually and by the MPU. The main reason for use of the reversing switches was that in some cases the thermal emf introduced a large error in the measured voltage across the thermometers. As explained in section 3.4.2 by reversing the current and averaging the voltage the steady thermal emf could be eliminated. In the analogue section the transistor (2N5457) was used to supply a constant current in the output independent of the change of impedance of the circuit. The command codes for these units are as:

	Function	BCD code	Octal code	Output on control unit
c.c. unit # 1	Normal	51	121	01010001
" " 1	Reverse	52	122	01010010
" " 2	Normal	55	125	01010101
" " 2	Reverse	56	126	01010110

3.4.4 External Circuit Controllers

Four additional circuit controllers were built for various circuits such as (a) controlling the magnetic field (b) operating the superconducting switch to put the magnet into the persistant-mode (c) to control a magnetic valve on the pressure regulator to fix the vapour pressure. Availability of external circuit controllers increased the versatility of the whole system so much that in fact it was used for some

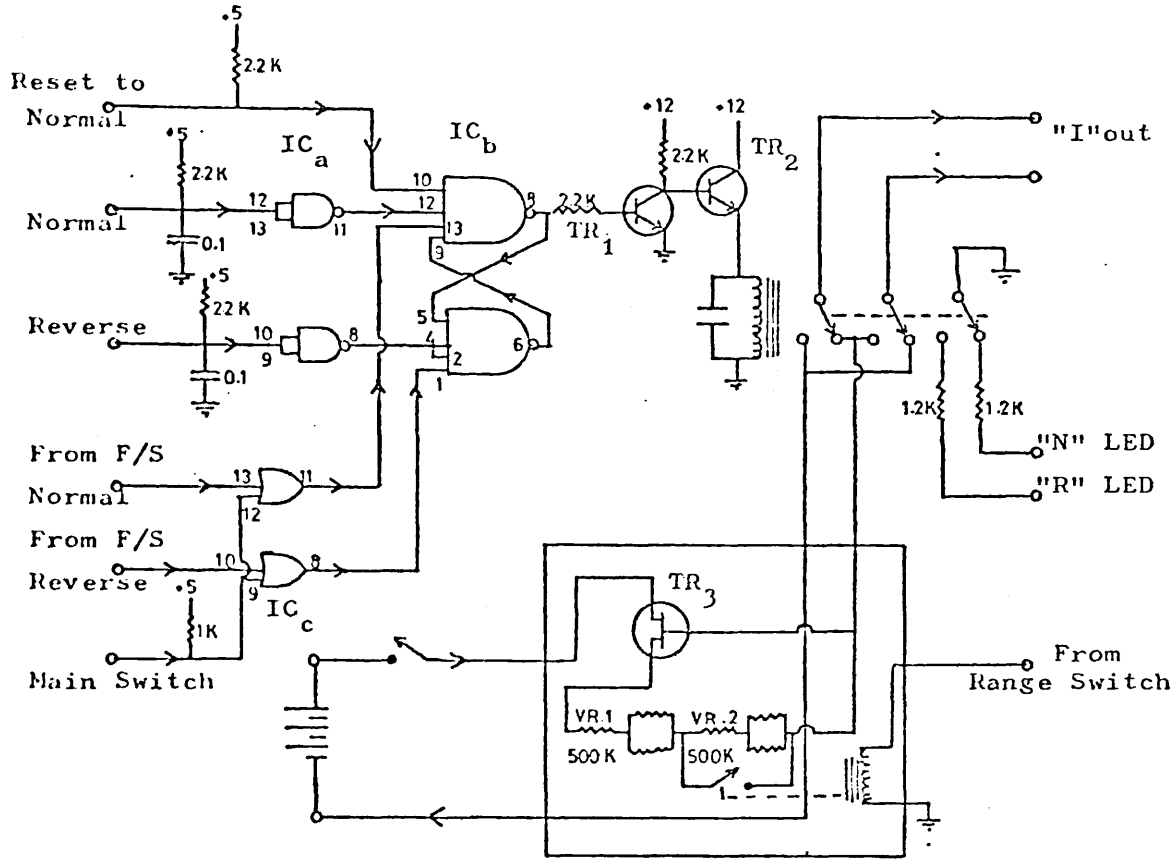

IC_a SN74132N
IC_b SN7420N
IC_c SN7432N
TR_1 BC108
TR_2 2N3053
TR_3 2N5457

Figure 15. Circuit diagram for one of the constant current units.

other low temperature experiment as programme controlled and fully automatic measurement. The logic circuit analysed the command received from MPU, and sent a signal which was amplified by TR#1,2 see Fig. (16) and finally activated the relay. The command code are as following:

	Function	BCD code	Octal code	Output on control unit
External	1 OFF	41	101	01000001
"	1 ON	42	102	01000010
"	2 OFF	43	103	01000011
"	2 ON	44	104	01000100
"	3 OFF	45	105	01000101
"	3 ON	46	106	01000110
"	4 OFF	47	107	01000111
"	4 ON	48	110	01001000

3.4.3 Interface and Decoder

There are three slots available in the Keithly Control Unit (780), slot # 1 was used for digital voltmeter 174 and slot # 2 was used to send the commands from MPU to the Digital Controller Unit (DCU). In the Auto mode the MPU was connected via an interface board which decoded the control signals: Enable Pulse, Control Pulse (CP), Data Pulse (DP), Byte 1 and Byte 2 see Fig. (17) . The systems would only receive commands after receiving an enable pulse. On receiving a CP the decoder logic would be reset ready for the first DP. When this DP was received together with a Byte 1 pulse, the Functions Address register would be loaded with an 8-bit code corresponding to whatever command the MPU wished to make (I.E. Load Aux. Heater Latch, Sweep up the field, etc.). This DP was then delayed by approximately 1 S and used as a "Data Valid" signal to the Function Selection logic. If a single function only was required then

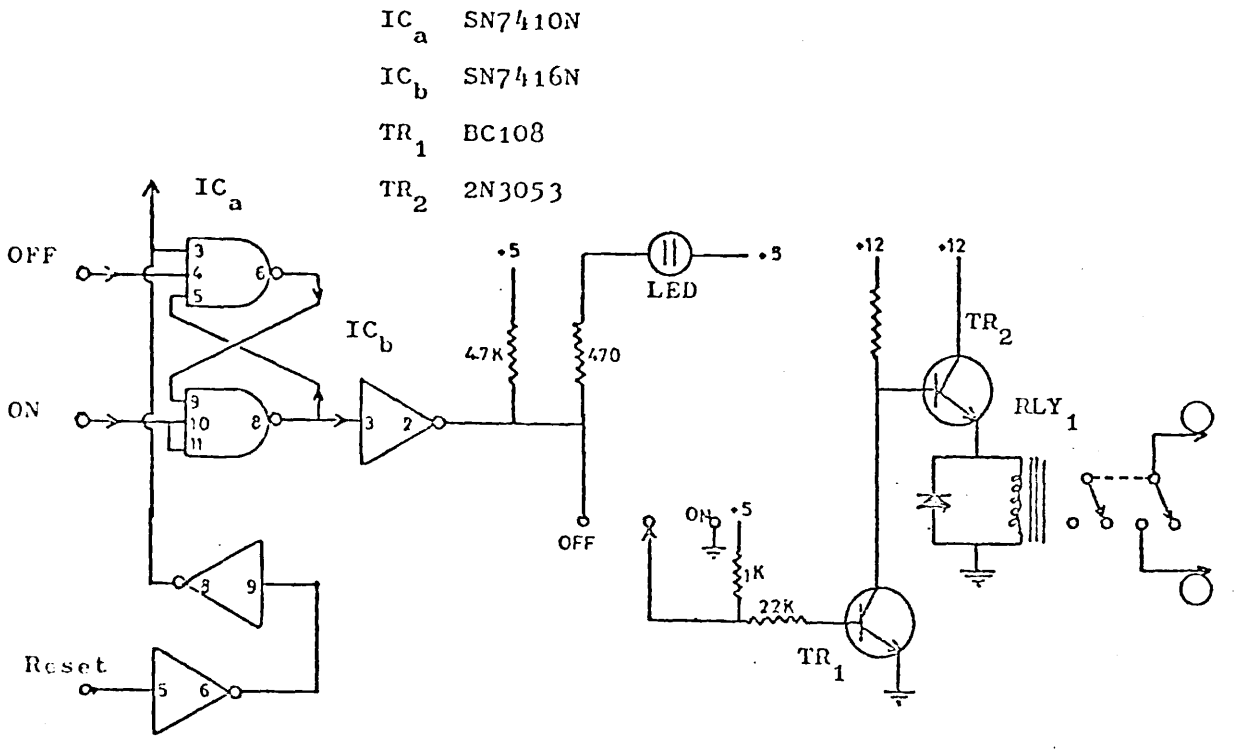

Figure 16. Circuit diagram for one of the external ciruit controller.

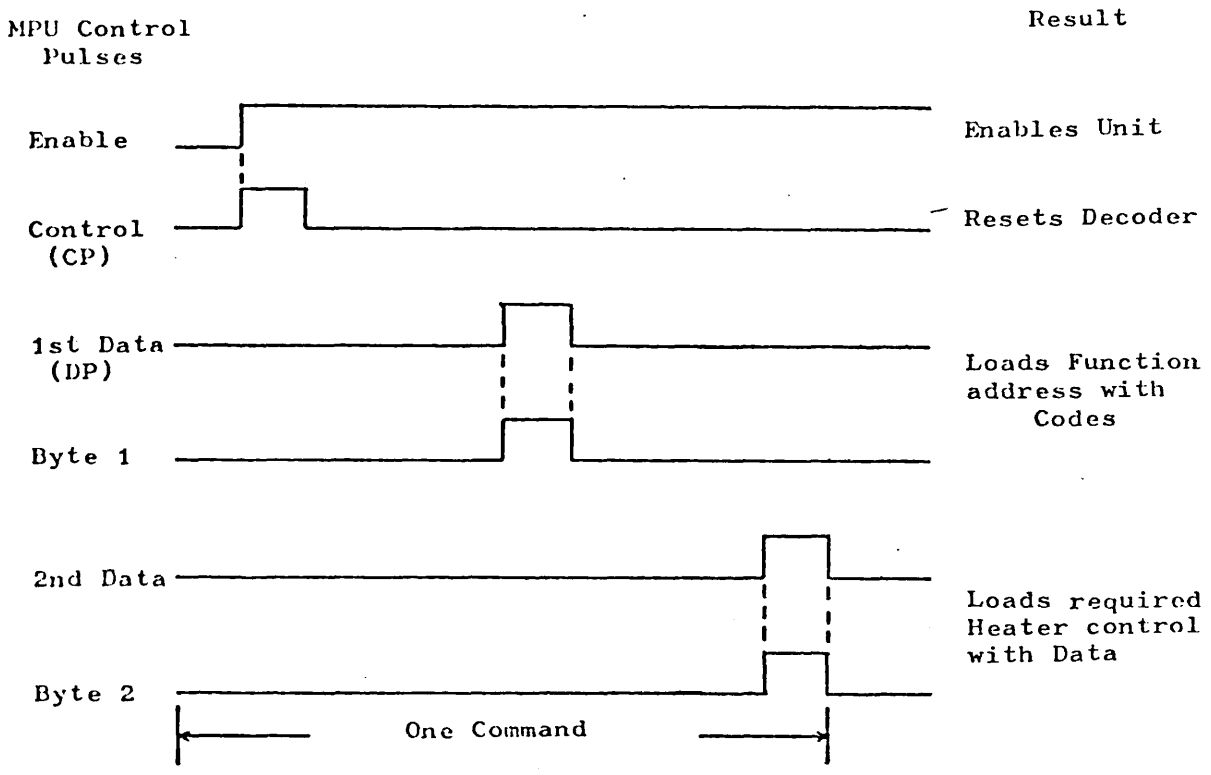

Figure 17. Pulse chart for interface and decoder.

the commands would be executed the moment this "Data Valid" pulse was received. However, if data was to be loaded into one of the heater control registers, then the appropriate register was set up by this first byte (Byte 1) and then on receiving the second DP together with a Byte 2 pulse the data was loaded and would change the heater current accordingly. Codes from Control Unit were inverted by two (SN7486) IC's Fig. (18) and the output of these were transferred to the latch on DTC board and also stored in the 8-bit latch (SN74116) and the output of the latch went into two, four to ten BCD (SN7442) IC's, from which the new codes directly transmitted to function selector board. There were also some other signals from control unit which were carrying enable slot on reset signal.

3.4.6 Function Selector Board

The output from the decoder board was directed to the function selector which was the actual element of the system that completed the analysis of the code sent from MPU through the control unit and transmitted the proper command to each part of the system for execution. From the hardware point of view it was a large board containing 20 IC's. Another facility on this board was the manual control logic which provided manual commands that could override the MPU's. As it is shown in the circuit diagram Fig. (19) how each pulse is inverted or where it would be transmitted.

3.5 Measurements of Thermal Conductivity in Zero Field

A steady-state heat flow method was used for measurement of thermal conductivity. Two Allen-Bradley thermometers R_1

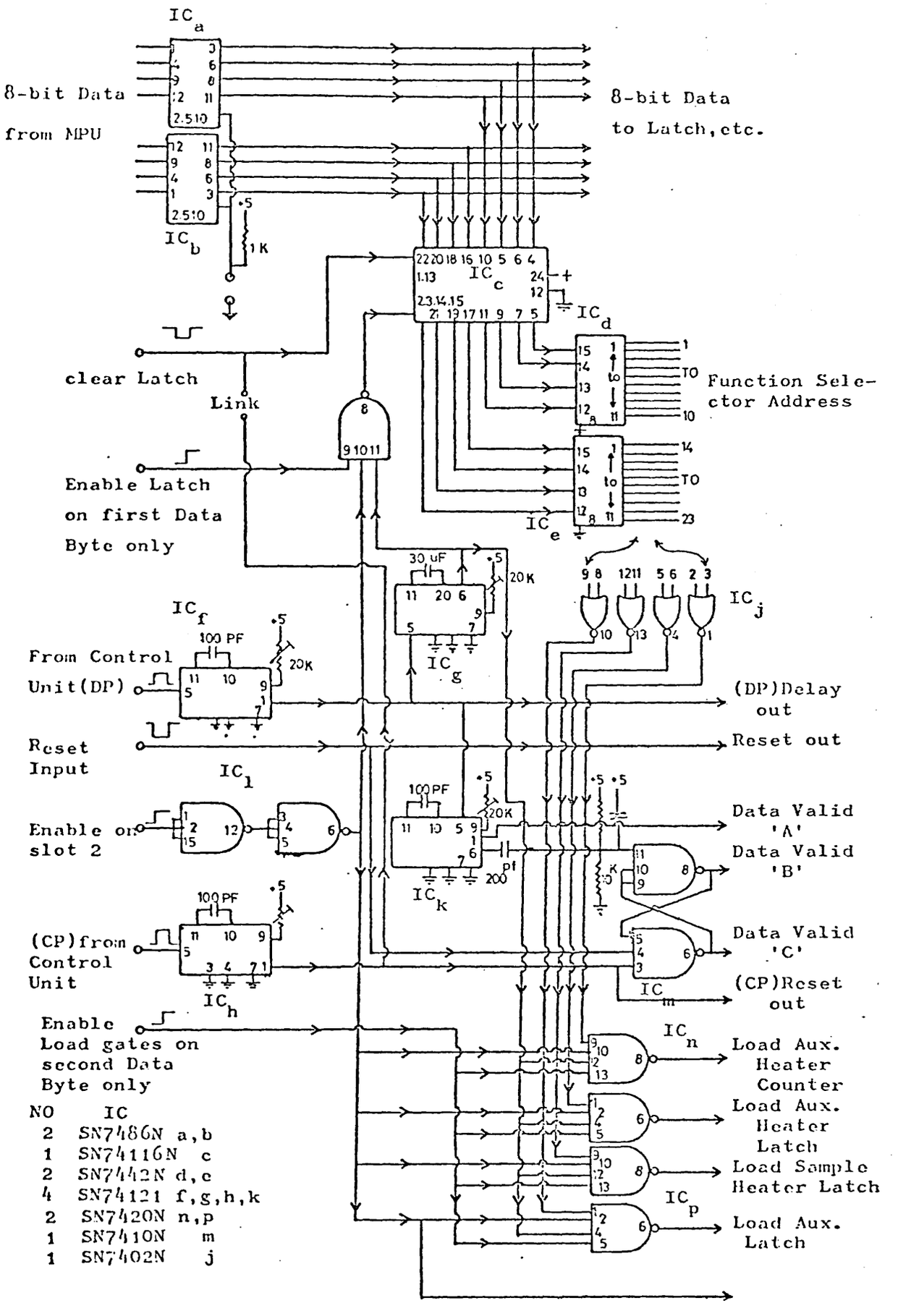

Figure 18.Circuit diagram for decoder and interface.

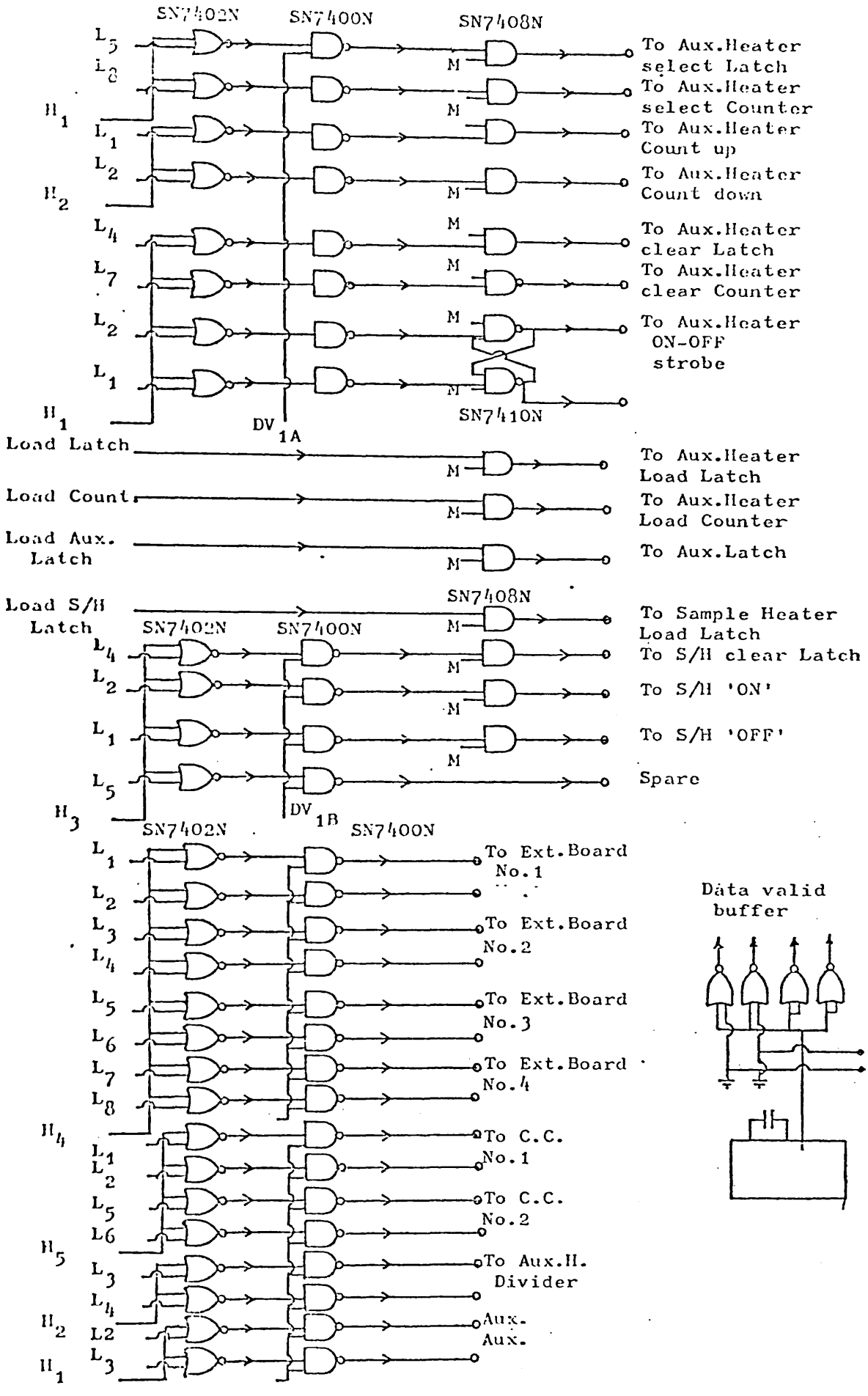

Figure 19.Circuit diagram of the function selector board.

and R_2 were used to measure the temperature gradient across the sample. The thermometers were constructed by wrapping the resistors with a winding of 36-gauge enamel-coated copper wire, the ends of which were brought together, twisted and soldered with indium to two copper rings which were soldered over the ends of the sample for better thermal contact between the specimen and the thermometers. A calibrated carbon-glass thermometer R_3 was used to calibrate thermometers R_1 and R_2 Fig. (20) shows the position of each thermometer on the crystal. The sample heater consisted of 46-gauge constantan wire wound in bifilar manner (to avoid creating a magnetic field) on an L-shaped piece of 14-gauge copper wire which was soldered with indium to one end of the crystal and covered with General Electric No. 7031 varnish. The other end of the sample was firmly clamped and indium soldered to the sample holder. The sample holder itself was screwed in a copper rod in contact with the helium pot. For further measurements of thermal conductivity in a magnetic field one sample holder was prepared for each sample to avoid any damage to the sample during replacement and once the sample was fixed on a sample holder it was very easy and practical to mount it in the cryostat. Two auxiliary bifilar heater was constructed by winding the constantan resistance wire around a section of the sample holder specially machined for this purpose on the main copper rod which was thermally sinked to the helium pot.

The resistance of the sample heater and auxiliary heater at room temperature were respectively 700 and 900 ohms.

The thermometric circuit - The two thermometers number 1 and 2 which were soldered to copper brackets on both ends of the

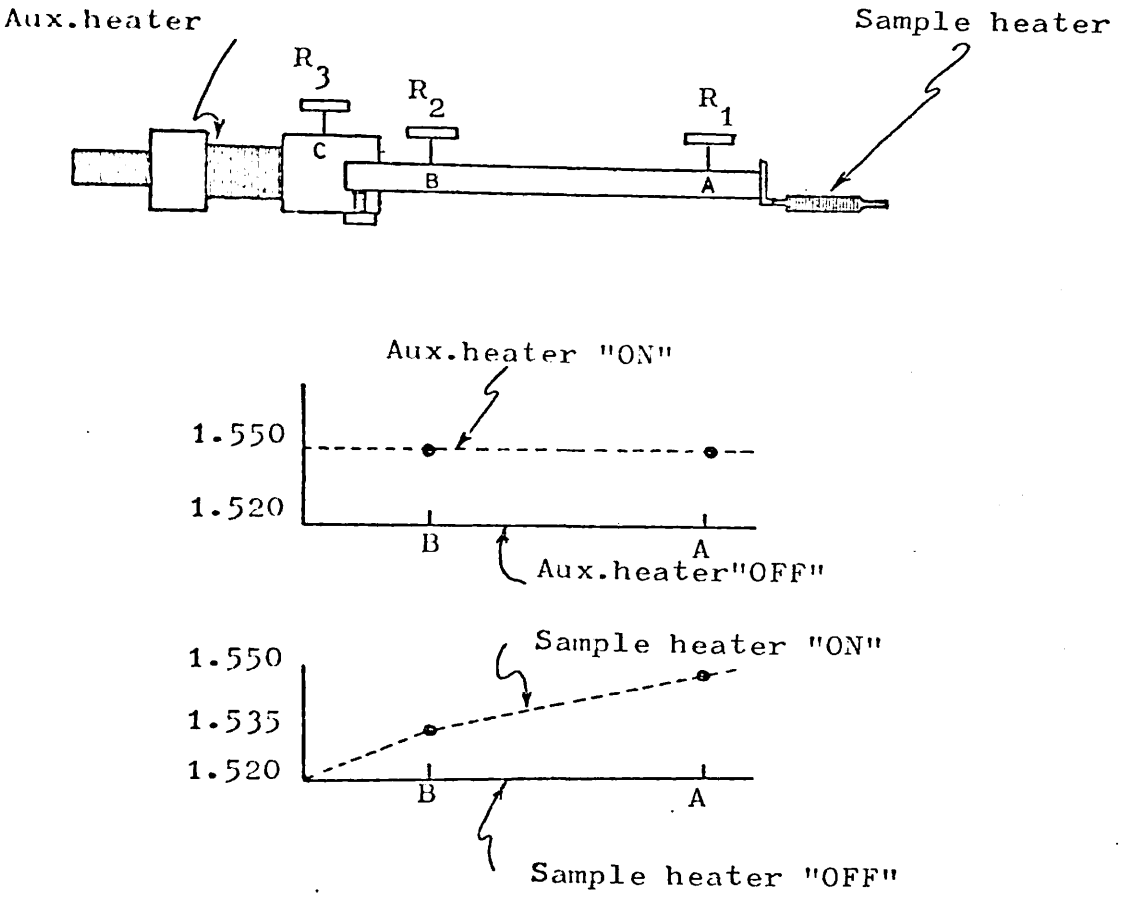

Figure 20. Schematic diagram of the thermometers position on the crystal and temperature gradiant across the crystal of InSb during different stages of measurements.

sample were in a bridge, shown below, where R_0 was a constant 100 KΩ resistance.

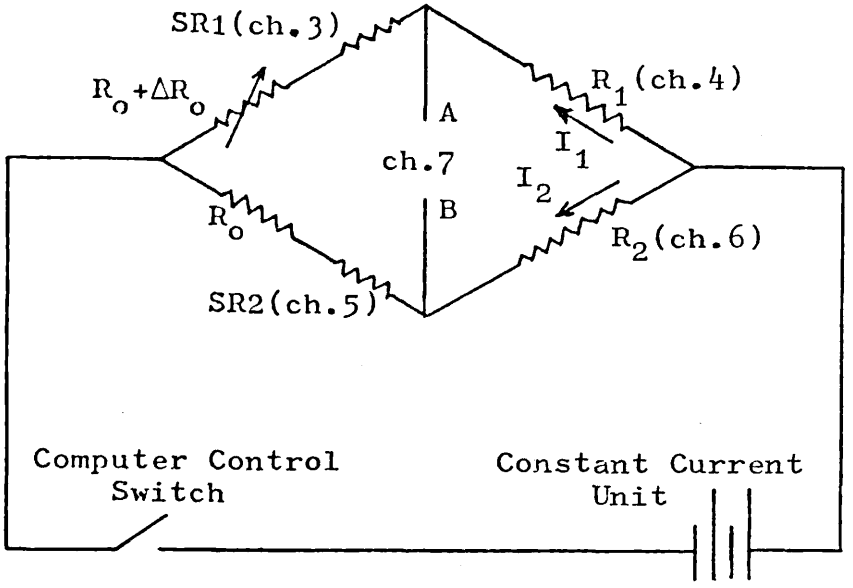

Fig.(21)

The carbon-glass thermometer was in a separate circuit by itself.

The procedure of thermal conductivity measurement - To measure the thermal conductivity first we turned the sample heater on, then measured the potential difference between A and B. At the same time resistance of thermometer number 2 was determined by measuring the voltage V_2 across R_2 and 1 K standard resistance number 2 which give the current I_2. After this measurement, the sample heater was turned off, but the auxiliary heater was turned on to bring back the whole sample to the same temperature that it had reached during the measurement, that is the same temperature which was read by R_2; then under these conditions, we again measured the potential difference between A and B. According to the following calcualtions where the quantities are those shown in the diagram above, the temperature drop could

be obtained from the measurements described above:

$$E = \left[R_b + R_o + \Delta R_o + R_1\right] I_1 + R_b I_2$$

$$E = +R_b I_1 + \left[R_b + R_o + R_2\right] I_2$$

Consider:

$$A = R_b \left[2R_o + \Delta R_o + R_1 + R_2\right] + \left[R_o + \Delta R_o + R_1\right]\left[R_o + R_2\right]$$

then we get:

$$I_1 = \frac{E(R_o + R_2)}{A}, \qquad I_2 = \frac{E(R_o + \Delta R_o + R_1)}{A}$$

$$V = V_B - V_A = \frac{E}{A}\left[R_2(R_o + \Delta R_o + R_1) - R_1(R_o + R_2)\right]$$

$$V = \frac{E}{A}\left[R_2(R_o + \Delta R_o) - R_o R_1\right] \qquad (1)$$

If the bridge is balanced $V = 0$ and we get $\frac{R_2}{R_1} = \frac{R_o}{R_o + \Delta R_o}$ (2)

$$V = \frac{E}{A}\left[(R_o + \Delta R_o + R_1)\frac{R_2(R_o + \Delta R_o)}{(R_o + \Delta R_o + R_1)} - \frac{R_o R_1(R_o + R_2)}{R_o + R_2}\right]$$

Assume

$$\alpha_1 = \frac{R_o}{R_o + R_2}, \qquad \alpha_2 = \frac{R_o + \Delta R_o}{R_o + \Delta R_o + R_1}$$

then

$$V = \frac{E}{A}\left[\alpha_2 R_2(R_o + \Delta R_o + R_1) - \alpha_1(R_o + R_2)R_1\right.$$

Substituting I_2, I_1 then

$$V = \alpha_2 R_2 I_2 - \alpha_1 R_1 I_1$$

When we turn the sample heater on there is a change in V:

$$\delta V = \frac{E}{A}\left[(R_o + \Delta R_o)\delta R_2 - R_o \delta R_1\right. + \frac{E}{A^2}\left[R_2(R_o + \Delta R_o) - R_o R_1\right]\delta A \qquad (3)$$

Substituting (2) in (3)

$$\delta V = \alpha_2 I_2 \delta R_2 - \alpha_1 I_1 \delta R_1 \qquad (4)$$

Using second order approximation for the change of each are resistance with respect to temperature we have:

$$\delta R = \frac{\partial R}{\partial T} \cdot \delta T + \frac{1}{2}\frac{\partial^2 R}{\partial T^2} (\delta T)^2 \qquad (5)$$

If $T_1 - T_2 = t$ and $\frac{T_1 + T_2}{2} = \overline{T}$, so that t is the temperature drop and $\overline{T}$ the mean temperature during measurements, then

$$T_1 = \overline{T} + \frac{t}{2} \qquad \text{and} \qquad T_2 = \overline{T} - \frac{t}{2}$$

Substituting (5) in (4) we get the following:

$$\cdot(\delta V) = \tfrac{1}{2}\left[I_2\alpha_2(\frac{\partial R_2}{\partial T}) + I_1\alpha_1(\frac{\partial R_1}{\partial T})\right]\delta t + \left[I_2\alpha_2(\frac{\partial R_2}{\partial T}) - I_1\alpha_1(\frac{\partial R_1}{\partial T})\right]\delta\overline{T}$$

$$+ \tfrac{1}{2}\left[I_2\alpha_2(\frac{\partial^2 R_2}{\partial T^2}) - I_1\alpha_1(\frac{\partial^2 R_1}{\partial T^2})\right]\left[(\delta\overline{T})^2 + (\frac{\delta t}{2})^2\right]$$

$$+ \tfrac{1}{2}\left[I_2\alpha_2(\frac{\partial^2 R_2}{\partial T^2}) + I_1\alpha_1(\frac{\partial^2 R_1}{\partial T^2})\right]\delta t\delta\overline{T}$$

or where $\delta V = A^*\delta t + B^*\delta\overline{T} + C^*\left[(\delta T)^2 + (\frac{\delta t}{2})^2\right] + D^*\delta\overline{T}\delta t$

$$A^* = \tfrac{1}{2}\left[I_2\alpha_2(\frac{\partial R_2}{\partial T}) + I_1\alpha_1(\frac{\partial R_1}{\partial T})\right]$$

$$B^* = \left[I_2\alpha_2(\frac{\partial R_2}{\partial T}) - I_1\alpha_1(\frac{\partial R_1}{\partial T})\right]$$

$$C^* = \tfrac{1}{2}\left[I_2\alpha_2(\frac{\partial^2 R_2}{\partial T^2}) - I_1\alpha_1(\frac{\partial^2 R_1}{\partial T^2})\right]$$

$$D^* = \tfrac{1}{2}\left[I_2\alpha_2(\frac{\partial^2 R_2}{\partial T^2}) + I_1\alpha_1(\frac{\partial^2 R_1}{\partial T^2})\right]$$

According to our calibration curves in thermometry sections B^* and C^* terms are negligible because of the good matching of R_1 and R_2. When we adjust I_1 and I_2 to satisfy the conditions:

$$\frac{I_2\alpha_2}{I_1\alpha_1} = \frac{\partial R_1}{\partial R_2} = \alpha' \qquad (6)$$

then

$$\delta V = A^*\delta t + D^*\delta\overline{T}\delta t \qquad (7)$$

But in order to have a linear approximation or just the A^*

term, the term $D^* \delta \bar{T}$ must be negligible. This term is proportional to the rise in mean temperature of the whole sample after turning the sample heater on. A good heat contact between the crystal and the heat sink is essential to minimize this term because it reduces $\delta \bar{T}$. The Fig. (20) shows the temperature rise across the sample and between each thermometer. So by measuring δV, and calculating δt from the formula (7) and also measuring the current (I_H) and voltage (V_H) of the sample heater, and the distance between the points of attachment of the thermometers, we measured the heat gradient, and by using the following standard expression we calculated thermal conductivity:

$$K = \frac{\dot{Q}}{A} \cdot \frac{L}{\delta t}$$

where $\dot{Q} = I_H \cdot V_H$ and L is the distance between thermometers # 1 and #2 and A is the cross-section of the crystal. The points which must be mentioned is that the quantities α_2 and α_1 appearing in A^* were calculated for each temperature point to avoid further approximation and the crucial adjustment of I_1 and I_2 by changing ΔR_o to bring α' to the correct value (e.g. (6) above).

As mentioned before the above procedure normally is done manually and the calculation is performed by the use of a computor. But by using a Kiethly system one and the Digital Controller explained in previous section the thermal conductivity measurement was made through an appropriate programme loaded into system one.

Control Programme - The main features of the programme consist of the following :

1. At each point the temperature was fixed and controlled and two thermometer numbers 1 and 2 were calibrated against the precalibrated carbon-glass thermometer.

2. The sample heater was turned on to create heat gradient through the sample.

3. The current and voltage across the thermometers and sample heater was measured, and then each value was stored in the memory bank for later use.

4. The voltage difference δV across the bridge is measured.

5. To eliminate the thermal emf noise the current in all thermometers and the heater is reversed and step 3 and 4 was repeated.

6. The sample heater is turned off and the auxiliary heater turned on and returned the temperature of the whole sample to the point where R_2 was.

7. Using expression (7) the temperature difference and finally the thermal conductivity is calculated, and if $\frac{\delta t}{\overline{T}} < 0.01$ the sample heater current is changed and step 1 to 7 is repeated again.

The flow chart for the above procedure is shown in the following and the programme loaded on Keithly® System One for zero field thermal conductivity is given in appendix.

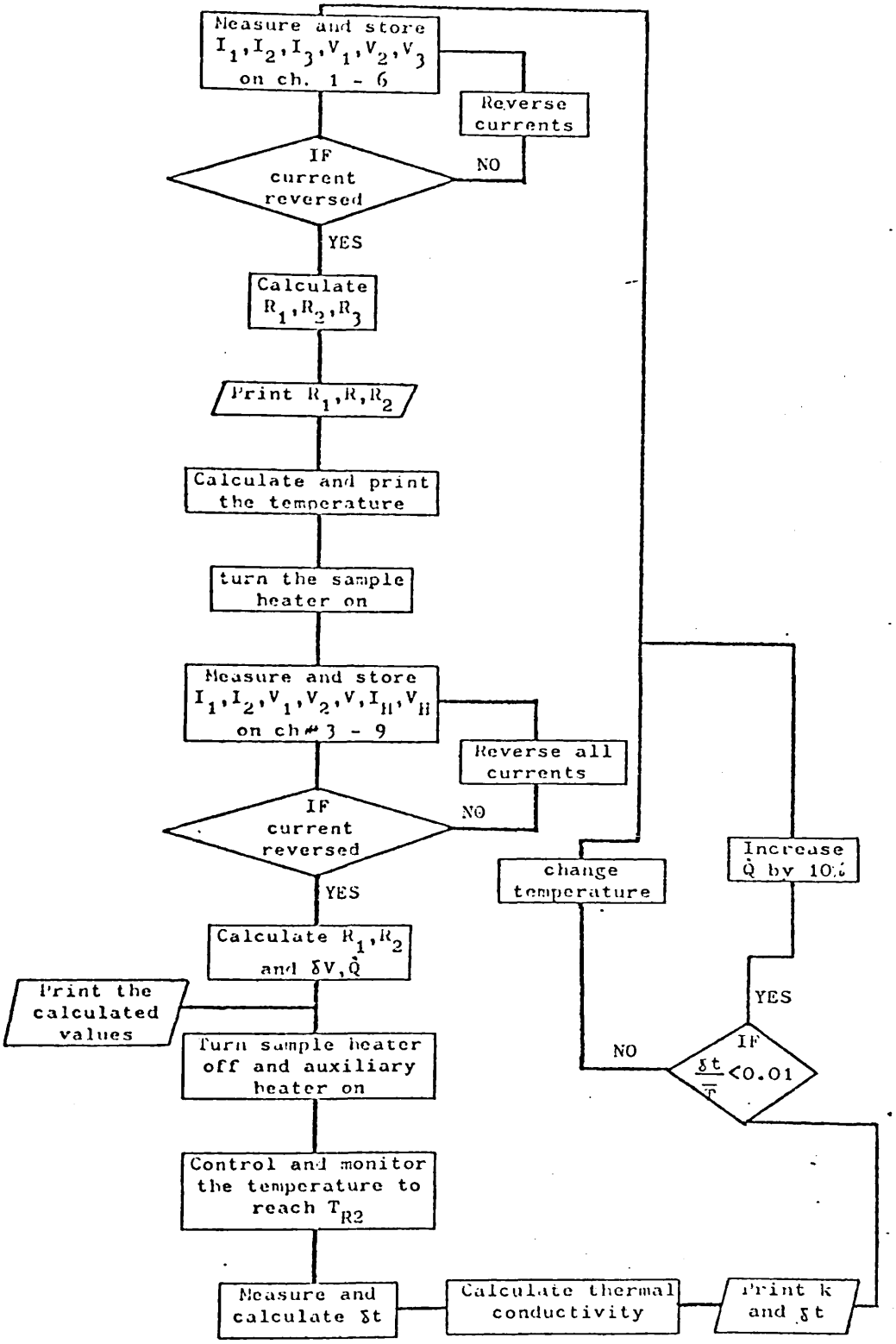
Measure and store $I_1, I_2, I_3, V_1, V_2, V_3$ on ch. 1 - 6
Reverse currents
IF current reversed
NO
YES
Calculate R_1, R_2, R_3
Print R_1, R, R_2
Calculate and print the temperature
turn the sample heater on
Measure and store $I_1, I_2, V_1, V_2, V, I_H, V_H$ on ch# 3 - 9
Reverse all currents
IF current reversed
NO
YES
Calculate R_1, R_2 and $\delta V, \dot{Q}$
Print the calculated values
Turn sample heater off and auxiliary heater on
Control and monitor the temperature to reach T_{R2}
Measure and calculate δt
Calculate thermal conductivity
Print k and δt
change temperature
Increase $\dot{Q}$ by 10%
YES
NO
IF $\frac{\delta t}{\bar{T}} < 0.01$

3.6 Thermal Conductivity Measurements in Magnetic Field

The effect of a magnetic field on the thermal conductivity of InSb is very small, but since only the relative change with field is needed a different method of measurement was used to that used for the zero field method. In these measurements an AC Signal Generator was used to supply the thermometers instead of the DC power supply, and the voltage difference across the bridge was measured by means of a Brookdeal lock-in-amplifier.

The output of the lock-in-amplifier was connected to the y-axis of an x-y recorder and the magnetic field to the x-axis.

Procedure of the measurements - The same bridge was used as before Fig. (21) for these measurements. First with the sample heater on, the out of balance voltage was measured as explained in section 5. The the change in this voltage was recorded as the magnetic field was swept up. The temperature had to be controlled to a very high stability because the output of the bridge was very sensitive to any temperature drift.

In order to avoid both interference of 50 Hz from the mains and a very long time constant the most suitable frequency was found, by an initial experiment, to be 180 Hz. The magnetic field was swept up/down to 40 KG at a rate of 20 - 50 minutes. To make sure that the output signal was not lagging behind the field due to the time constant of the device, the field was swept up and down for each measurement at a fixed temperature, to ensure the retrace of the recorded output.

The thermometers and the sample heater were placed 20 cm from the centre of the superconducting coil where the magnetic

field dropped to less than 250 gauss. This field was then shielded out by wrapping the thermometers with Niobium foils (critical field = 1980 gauss) to avoid magnetoresistance effects. A careful test to check the above was performed as follows: the sample heater was turned off and the temperature at the lowest point was kept constant. Then the output of the bridge was monitored while the field swept up to 40 KG, there was no change in the output signal, hence there was no effect due to the interactions between residual field and the thermometers.

CHAPTER 4

The Zero-Field Thermal Conductivity

4.1 n-InSb

Measurements of the thermal conductivity have been made between 1 and 10K of four samples of indium antimonide tellurium doped. Their specifications (e.g. dimensions, crystallographic orientation and impurity concentration, etc.) are given in section 3.1.

The results of the thermal conductivity measurements in zero-field are represented in a traditional logarithmic plot in figures (22 -25). The experimental data are in good agreement with the measurements of Challis et al[3] and Kosarev[5]. The following observations are considered:

1. There is a departure from the T^3 temperature dependency of the thermal conductivity, which is expected from an ideal dielectric at low temperature. In figure (26) by plotting K/T^3 vs T for sample (B) the divergence of the conductivity from T^3 is shown.

2. These measurements are not significantly dependent on the technique used for sample growth (sample E, C were boat grown and D, B were pulled).

3. When the impurities were added the thermal conductivity decreased and the maximum was shifted to higher temperatures.

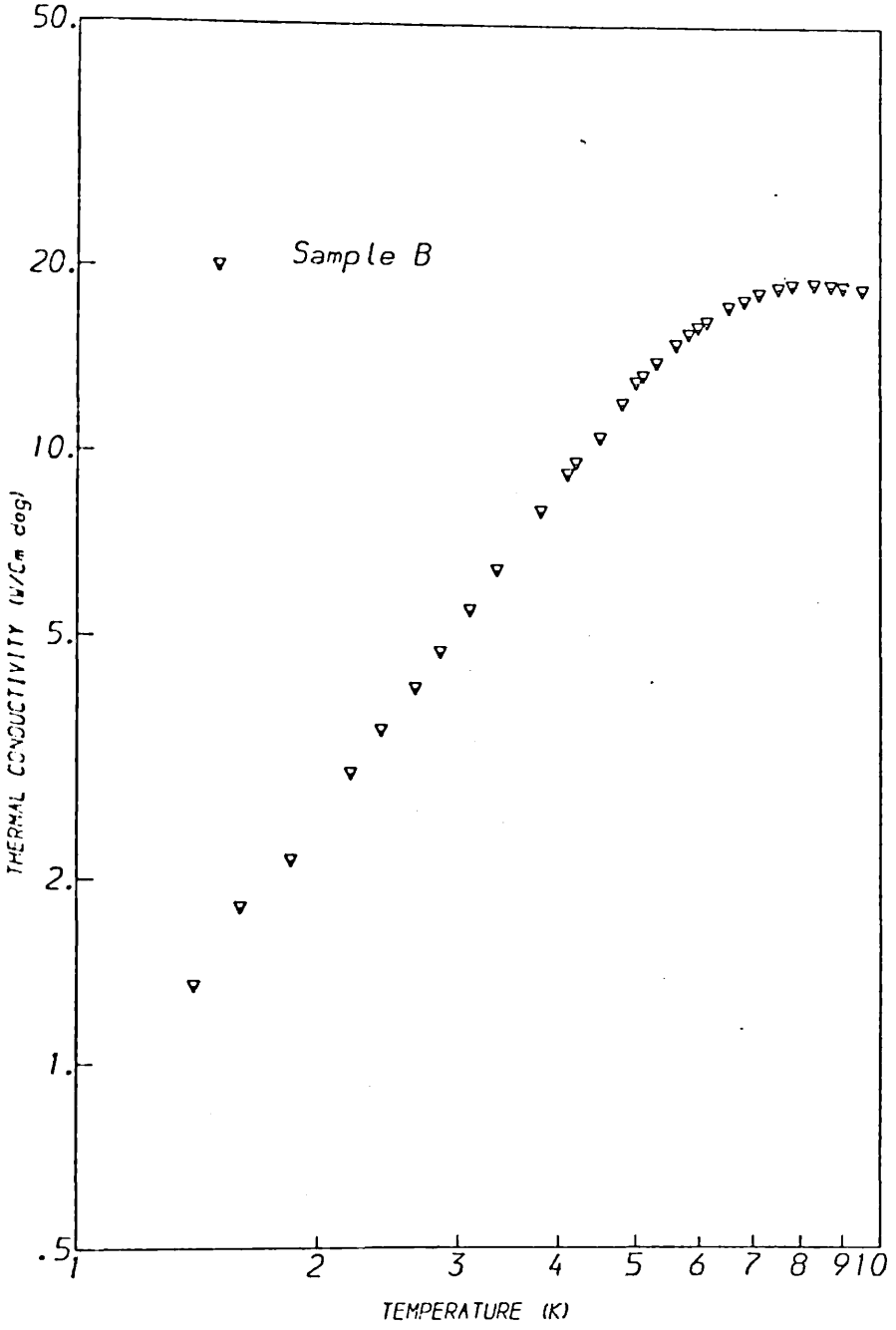

Figure 20. The lattice thermal conductivity of sample B with donor concetration $n=3\times10^{14}$ cm^{-3}.

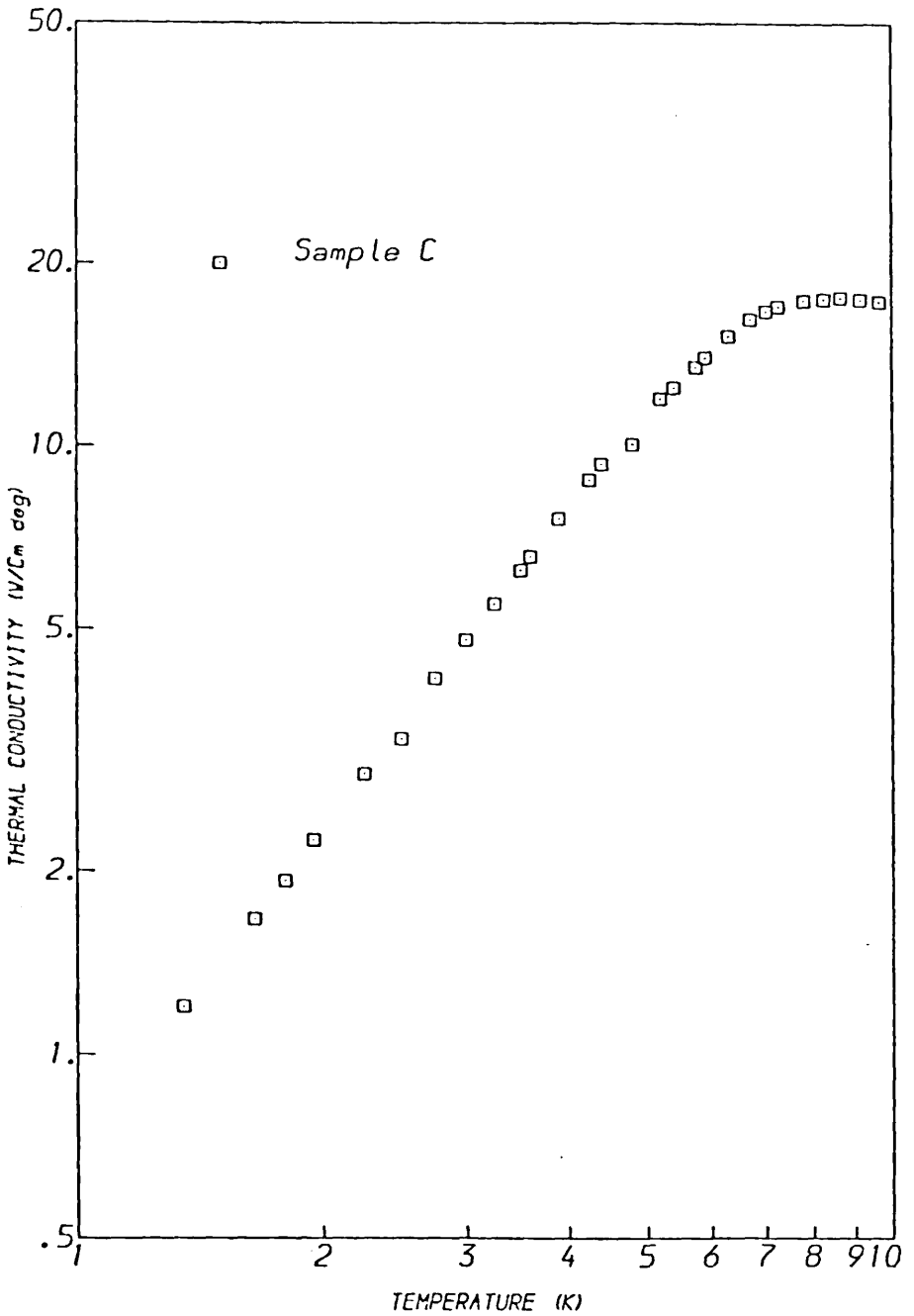

Figure 23. The lattice thermal conductivity of sample C with donor concentration $n=1.4\times10^{15}cm^{-3}$.

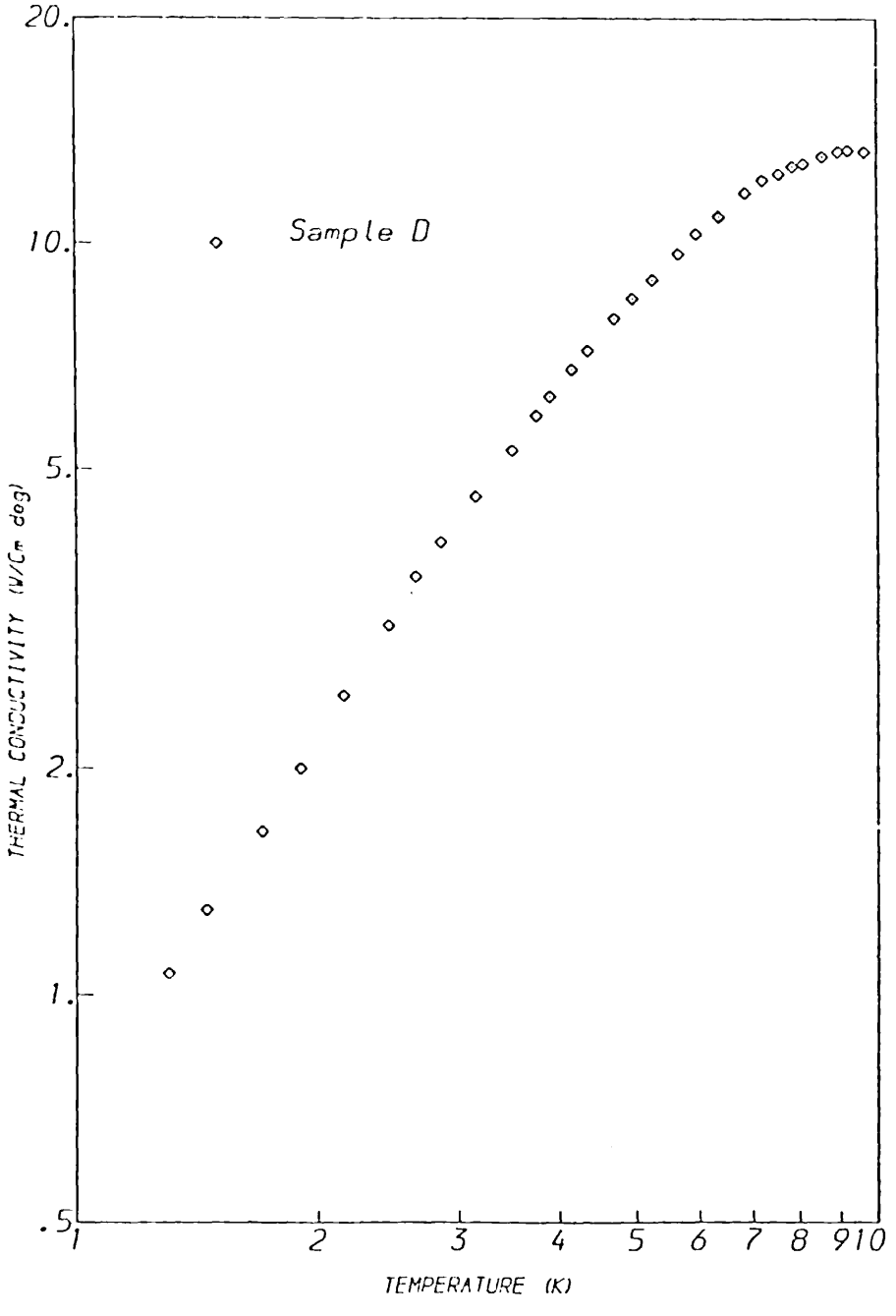

Figure 24. The lattice thermal conductivity of sample D with donor concentration $n=3.5\times10^{16}cm^{-3}$.

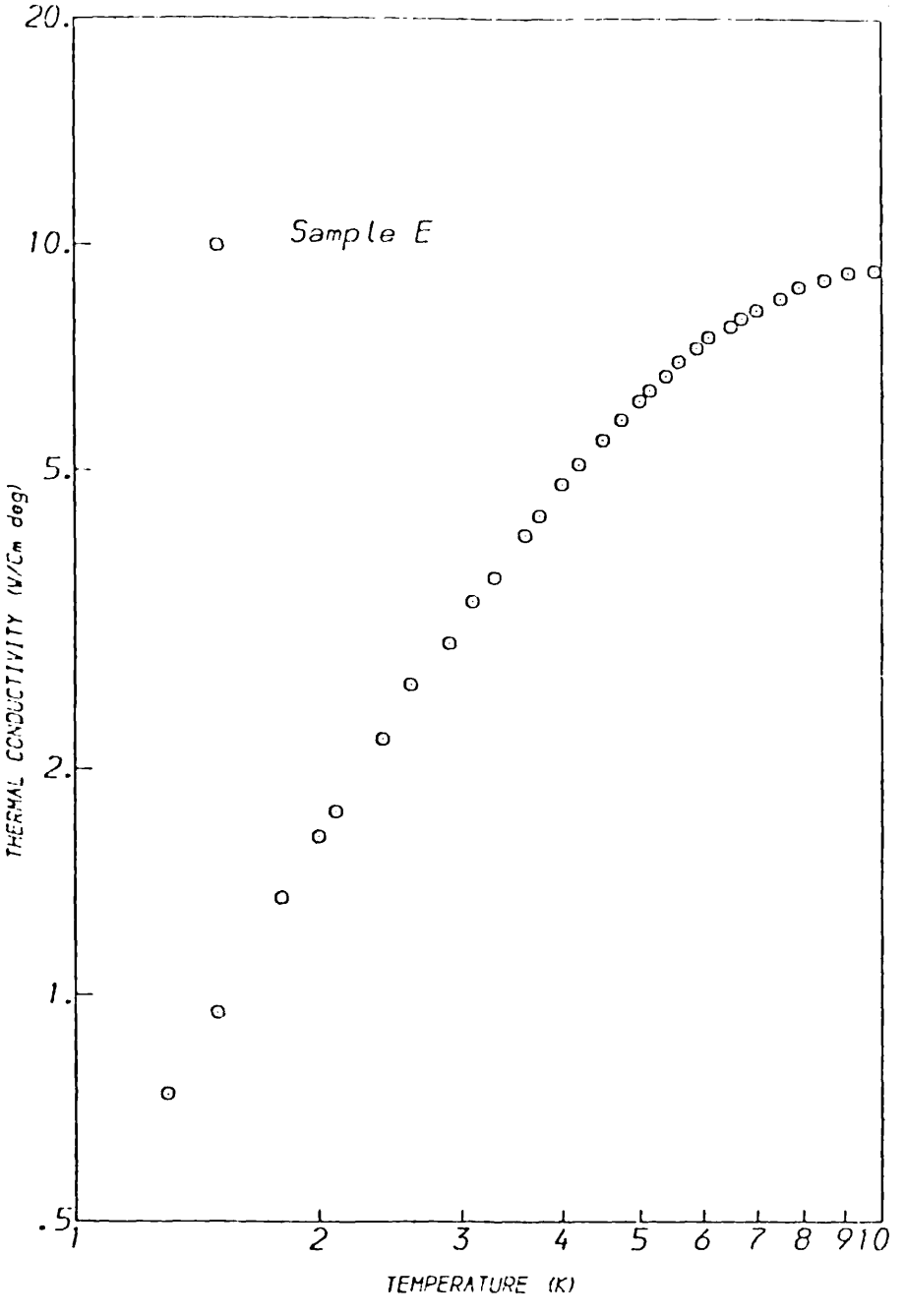

Figure 25. The lattice thermal conductivity of sample E with donor concentration $n=1.2\times10^{17}\,cm^{-3}$.

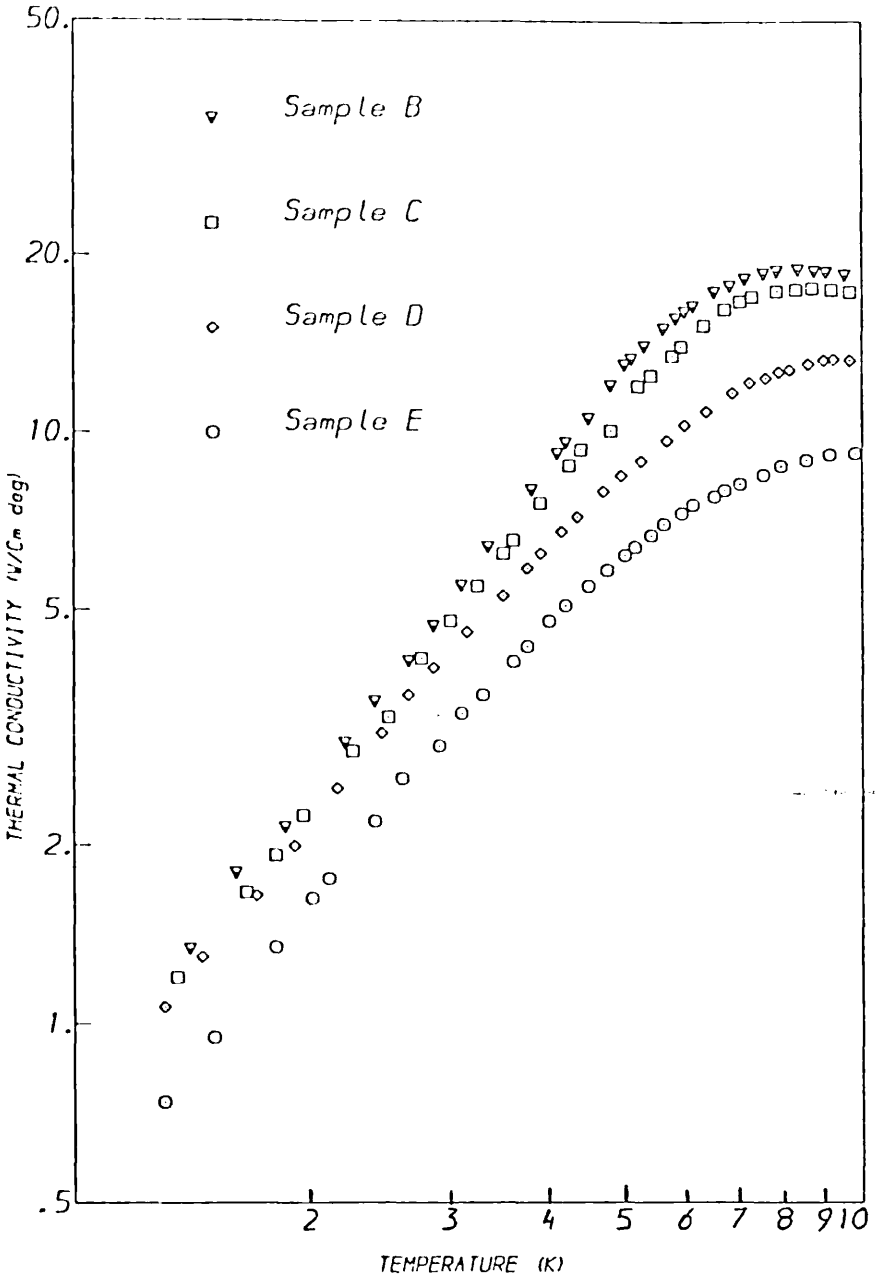

Figure 25a. The lattice thermal conductivity of four n-type samples.

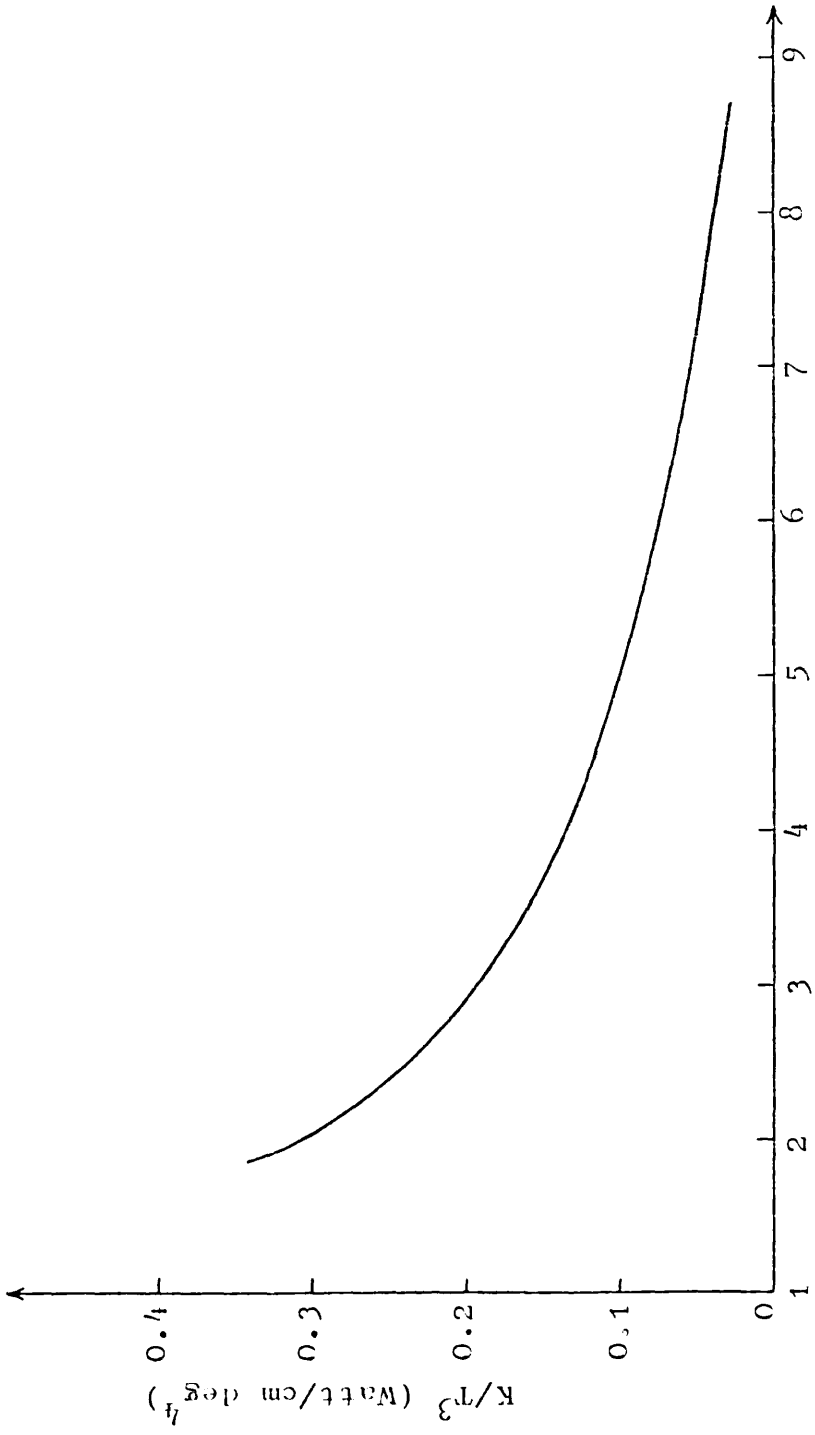

Figure 26. Lattice thermal conductivity devided by T^3 versus T for sample B.

4.1.1 Thermal Conductivity of the Least Doped Sample

The donor concentration of sample B with $N_D - N_A \simeq 3 \times 10^{14} cm^{-3}$ is low which can be considered almost pure. Its thermal conductivity results have been fitted to Callaway's thermal conductivity integral:

$$K(T) = \frac{k}{6\pi^2} \left(\frac{kT}{\hbar}\right)^3 \sum_{t=1}^{3} \frac{1}{v_t} \int_0^{\frac{\theta_D}{T}} t \frac{e^x x^4}{(e^x - 1)^2} dx \qquad (4.1)$$

where $x = \frac{\hbar\omega}{kT}$.

The total relaxation time t is considered to be a combination of three terms as in the following:

$$t^{-1} = t_b^{-1} + t_i^{-1} + t_p^{-1} \qquad (4.2)$$

where t_i , t_b and t_p are the relaxation times for phonon scattering by the isotopes , the crystal boundaries and the phonons. In t_i the effect of the defects and dislocations have been neglected because the ambient temperature is lower than that where these scattering mechanisms are effective. t_p become noticeable just at the higher temperature end (above 6K) .

4.1.2 Isotope scattering frequency t_i^{-1}

As mentioned in 2.4 the isotope scattering frequency is shown to be $t_i^{-1} = A\omega^4$ where A was defined before as:

$$A = V\Gamma / 4\pi v_s^3$$

Holland[4] initially considered $A = 0.923 \times 10^{-44} sec^3$. This differs appreciably from the value $A = 2.8 \times 10^{-44} sec^3$ obtained from the experimental data on an InSb sample with $n = 7 \times 10^{13} cm^{-3}$. As A depends on the velocity of sound , which is different for each crystalographic direction, the difference is not unexpected.

4.1.3 Boundary Scattering Frequency τ_b^{-1}

The rate of phonon scattering by the crystal boundaries has been calculated according to 2.3. Frankl et al[37] have given an analytical expression for the correction required to Λ for the finite length effect. Berman et al[23] graphically showed the correction as a function of R/L (where $R = \Lambda/2$ and L is the sample length) for different values of f the roughness parameter. Frankl's expression is:

$$\frac{1}{\Lambda'} = \frac{1}{\Lambda}\frac{1 - P}{1 + P} + \frac{1}{L}$$

where P, the specularity factor, measures the sample polish which is related to f by:

$$1 - P = f(\eta, q) = 1 - \exp(-2q^2\eta^2)$$

where η is the root-mean-square deviation of the surface from the level and is called asperity parameter.

4.1.4 Fitting Results

To fit the experimental data of sample B into the thermal conductivity integral, boundary scattering rate τ_b^{-1}, A and B were considered as adjustable parameters. A non-linear least square fitting routine was developed to calculate the above parameter according to the experimental points. The results are shown in the following table.

(Table II)

	τ_b^{-1}	A	B
Calculated	1.4×10^{6}	0.923×10^{-44}	1.92×10^{-22}
Best fit	1.25×10^{6}	2.42×10^{-44}	3.1×10^{-22}

Differences between calculated values and the best fit was expected because firstly there are some phonons specularly reflected from the boundaries and secondly in calculation of Λ the effect of dislocation and defects was not taken into account and in practice the experimental value of Λ is larger than the calculated value. From the value obtained for boundary scattering the specularity factor P can be calculated from Frankl and Campisi expression:

$$\tau_B^{-1} = v_s \left[\frac{1}{\Lambda}\left(\frac{1 - P}{1 + P}\right) + \frac{1}{L}\right]$$

substituting numerical value for each parameter P = 0.12.

An order of magnitude value for the asperity parameter can be deduced. Since at 1.5K the dominant phonon wave-vector is $(q = \frac{3.8kT}{\hbar v})$ 3.19×10^6 cm^{-1}, so the asperity $n = 35A^o$ is obtained. According to Campisi's data when $n \gtrsim 100A^o$ the sample may be considered rough. The calculated value for the phonon-phonon interaction parameter B from fitting is in a good agreement with the value given by Holland[4]. However, this scattering mechanism is only effective in the temperatures above liquid helium.

4.1.5 Thermal Conductivity of the More Heavily Doped Samples

The analysis of the zero field thermal conductivity for n-type samples with concentration larger than 10^{15} cm^{-3} is similar to that of pure sample with the difference of additional term in relaxation time which takes into account the effect of the electron-phonon interaction τ_{e-Ph}^{-1}.

4.1.6 Electron-Phonon Scattering

The lifetime of an acoustic phonon interacting with a quasi-free electron gas is calculated from standard first order perturbation theory[30]. If one assumes isotropy but not necessarily parabolicity, of the conduction band the relaxation rate is given by:

$$\tau_{e\text{-}ph}^{-1} = \frac{v_s m^2}{\pi \hbar^4} \left| V(q, u) \right|^2 \qquad \text{for } q < 2k_F$$

where $\left| V(q, u) \right|^2$ is the squared matrix element of the phonon potential, and the deformation potential induced by a sinusoidal strain give additive contribution to $\left| V(q, u) \right|^2$, since there is no interference term between them[38]. The above expression is valid only for wavevectors in the Fermi sphere of energy E_F (condition of strong degeneracy). An important aspect of the above equation is the absence of an explicit dependence on the total number of electrons. To deal with the electron-phonon interaction a free-electron dielectric permittivity was introduced[39] which would screen out the phonon potentials according to:

$$\frac{V_s(q, u)}{V(q, u)} = \frac{1}{1 + (q_{TF}/q)^2} F\left(\frac{q}{2k_F}\right)$$

with $$F(x) = \frac{1}{2} + \frac{1 - x^2}{4x} \ln \left| \frac{1 + x}{1 - x} \right|$$

The Thomas-Fermi wavevector, q_{TF} is given by:

$$q_{FT} = \frac{(4\pi e^2 / \varepsilon)^{1/2}}{v_F} = \left(\frac{4m^* e^2 k_F}{3\pi \hbar^2 \varepsilon}\right)^{1/2} \qquad (4.4)$$

The factor $F\left(\frac{q}{2k_F}\right)$ is nearly equal to 1 for $q < 2k_F$ and

decreases rapidly to 1/2 when $q = 2k_F$. Then the screening-enhanced relaxation time of a phonon interacting with an electron is given by Ihet et al[22]

$$\tau^{-1}_{\substack{e-ph \\ screen}} = (\frac{A}{q} + Bq) \frac{v}{(1 + 3(\frac{q_{TF}}{q})^2)^2 F^2(\frac{q}{2k_F})} \qquad (4.5)$$

where

$$A = \frac{32\pi e^2 m^{*2} (e_{14})^2}{\hbar^3 \varepsilon^2 \rho v_s} (\bar{q}_x \bar{q}_y \bar{u}_z + \bar{q}_y \bar{q}_z \bar{u}_x + \bar{q}_z \bar{q}_x \bar{u}_y)^2$$

$$B = \frac{m^{*2} c^2}{2\pi\hbar^3 \rho v_s} \cos^2(\bar{q}, \bar{u})$$

When we consider that the thermal phonons are propagating in the direction of [110] and only the longitudinal mode is interacting with electrons we get:

$$A = 0$$

$$B = \frac{m^{*2} c^2}{2\pi\hbar^3 \rho v_s}$$

where c = 13 eV for the deformation potential constant[38,41]

ε = 17 for the lattice dielectric permittivity,

$\rho = 5.80\ g/cm^3$.

In order to consider the relaxation rate due to the above scattering (Eqn. 4.5) the thermal conductivity integral (Eqn. 4.1) must be split in two parts as following:

$$K = A' \int_0^{\Theta^*/T} \frac{x^4 e^x dx}{\left[\tau_b^{-1} + ax^4 T^4 + \frac{bxT}{\left[1 + 3(\frac{\hbar v_s}{kT})(\frac{q_{TF}}{x})^2\right]^2}\right] (e^x - 1)^2}$$

$$+A' \int_{\Theta^*/T}^{\Theta/T} \frac{x^4 e^x dx}{\left[\tau_b^{-1} + ax^4 T^4\right](e^x - 1)^2} \qquad (4.6)$$

where

$a = A(\frac{k}{\hbar})^4$ the isotope scattering parameter

$$A' = \frac{k^4 T^3}{2\pi^2 \hbar^3} \sum_{t=1}^{3} \frac{1}{v_t} \qquad (4.7)$$

and

$$b = \frac{km^{*2}c^2}{2\pi\rho v_s \hbar^4} \qquad (4.8)$$

the electron-phonon interaction parameter. Θ^* is called effective Debye temperature and defined by:

$$\Theta^* = 2k_F \left(\frac{\hbar v_s}{k}\right) \qquad (4.9)$$

which limits the phonon wavevectors which can be scattered by electrons and an electron system is transparent for phonons with $\overline{q} > \overline{2k_F}$.

Fitting results for sample C did not show any electron-phonon scattering, but for the samples D and E the results revealed a small contribution of this scattering in the thermal conductivity at the lower temperature range. At 1.2K the dominant phonon wavevector $q = 1.6 \times 10^6$ cm^{-1} which is well in the allow range for above interaction (i.e. $4.1 \times 10^5 < q < 3.1 \times 10^6$ cm^{-1}).

4.2 p-InSb

Here experimental data of thermal conductivity of two Ge doped p-type indium antimonide single crystals are presented, see figures (27-28). Measurements have been performed on two specimen with specifications given

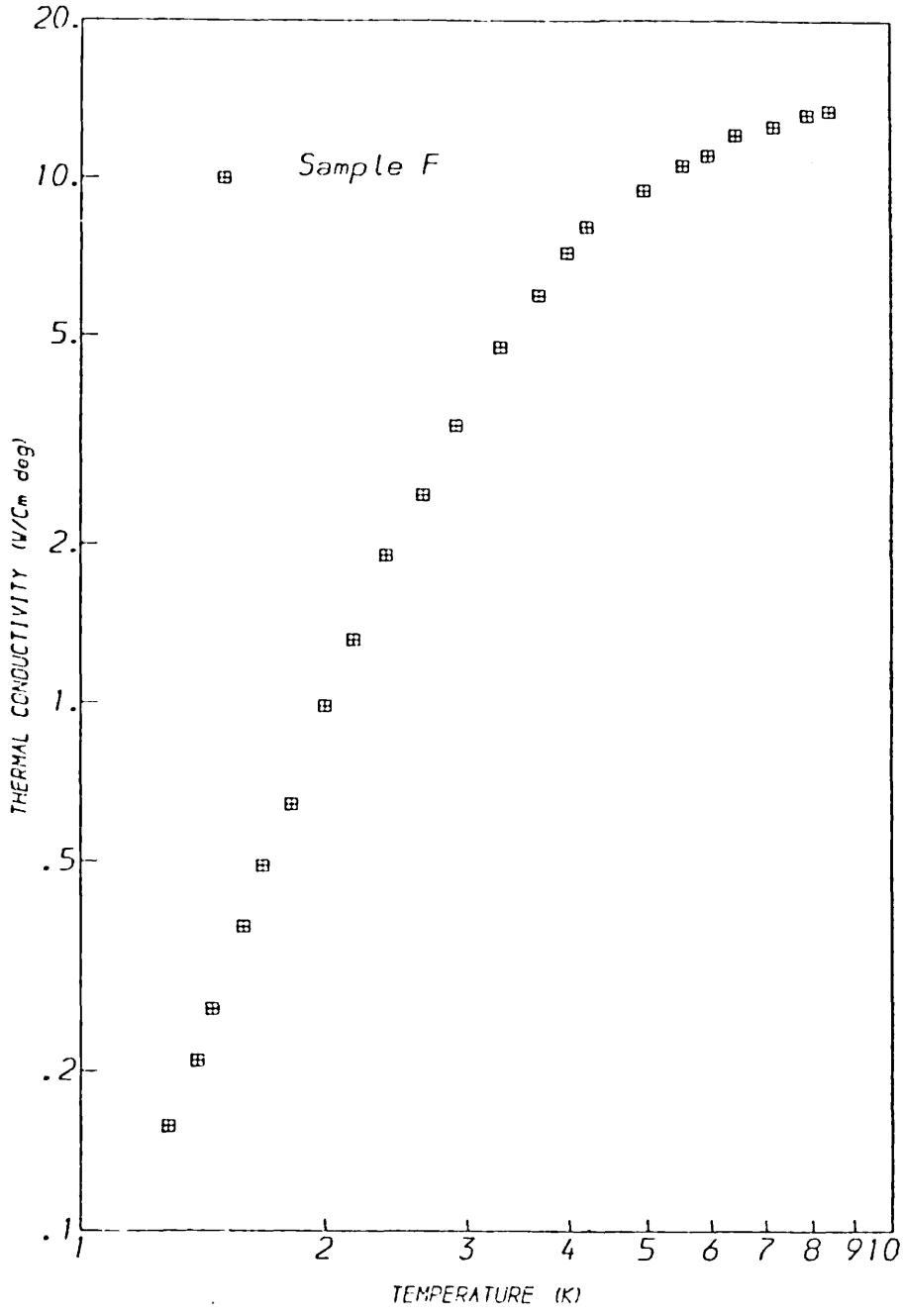

Figure 27. The lattice thermal conductivity of sample F with acceptor concentration $p=2.8\times10^{15}cm^{-3}$.

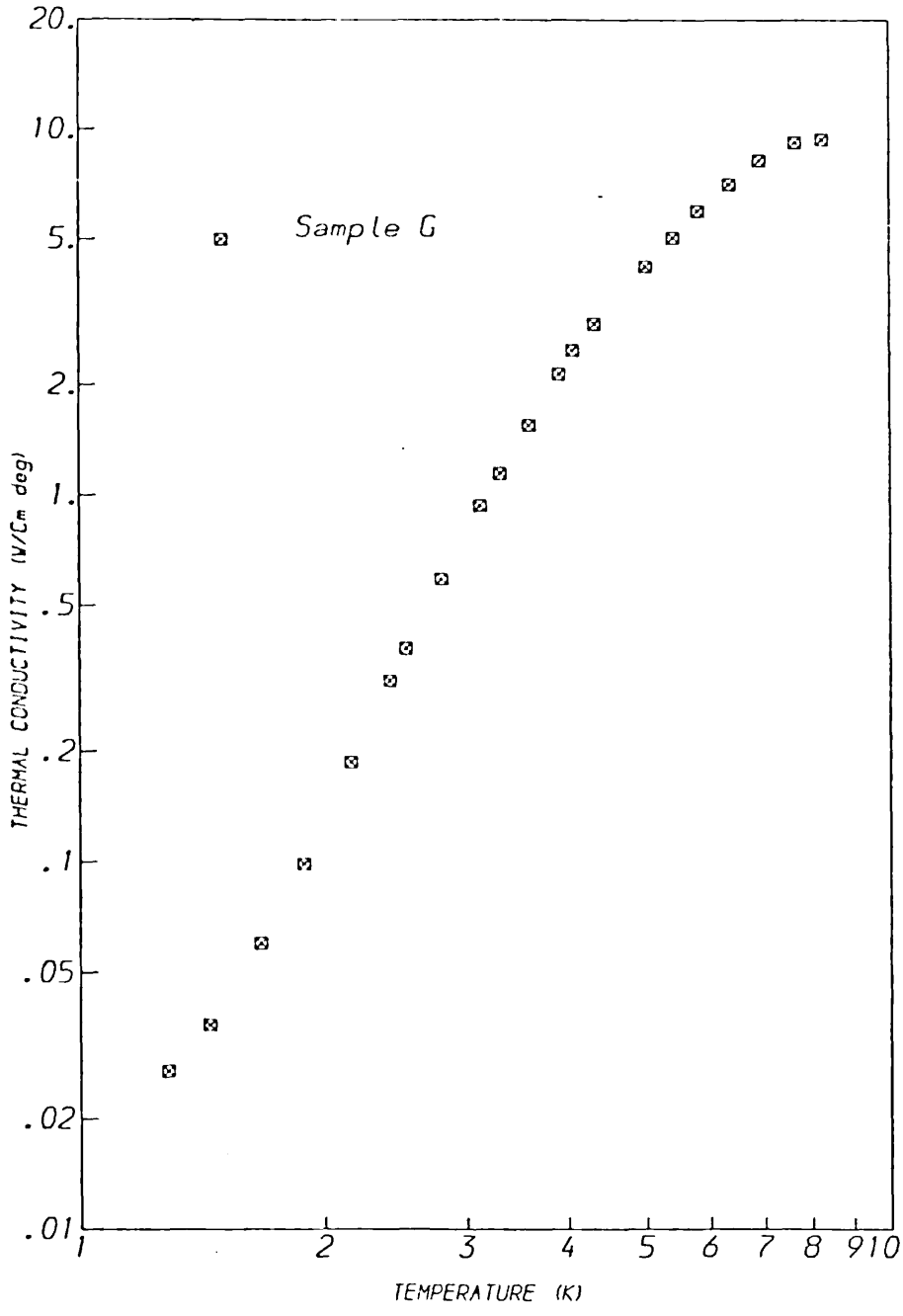

Figure 26. The lattice thermal conductivity of sample G with acceptor concentration $p=2.4\times10^{17}\,cm^{-3}$.

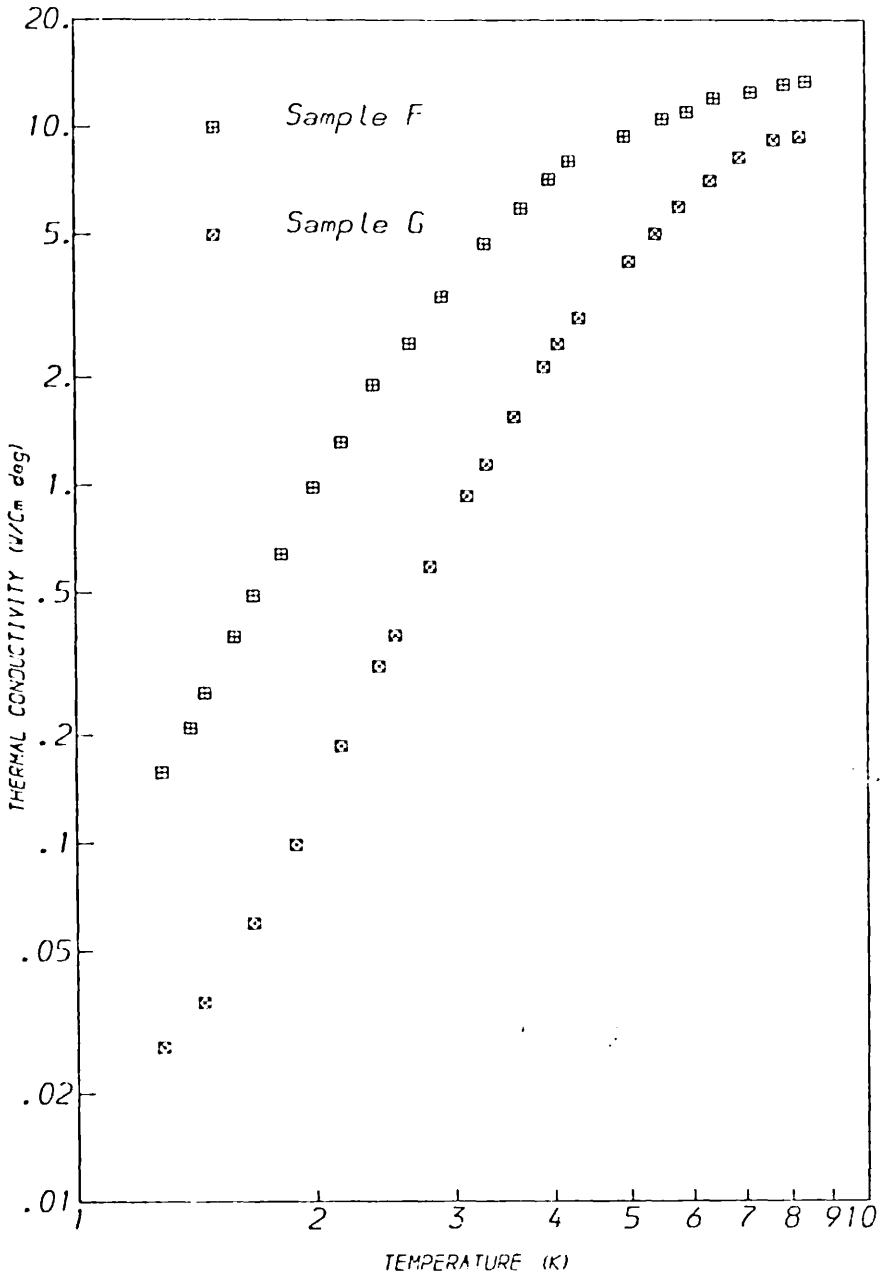

Figure 23a. The lattice thermal conductivity of two p-type samples.

in section 3.1. The effect due to the scattering of phonons by boundaries and isotopes is the same as the case of n-InSb. The strong phonon scattering in this type of crystals is not however caused by isotopes or imperfection of the lattice but is rather due to different scattering processes. In the sample with $N_A \simeq 2 \times 10^{17}$ cm^{-3} the phonon scattering is due to Ziman type charge carrier scattering and for the sample with $N_A \simeq 2.8 \times 10^{15}$ cm^{-3} the acceptors are neutral and their energy levels are split so that phonon scattering arises due to transition between these split states.

The effective mass of charge carriers (holes) is relatively large and phonon-charge carrier scattering mechanism which plays a decisive role accounting for great differences between the phonon thermal conductivity of n-type and p-InSb revealed by the experiments.

4.2.1 Charge Carrier -Phonon Scattering

The theoretical treatment of hole-phonon scattering in the degenerate case ($P \gtrsim 10^{17}$ cm^{-3}) when impurity levels form a band which overlaps with the valence band is already discussed in sections 2.5 and 4.1.5. The interaction of charge carriers and phonons becomes interesting when the acceptor levels are still isolated ($P \lesssim 10^{16}$ cm^{-3}) and they do not merge with the valence band.

The shallow acceptor ground state and the valence band edge of III-V semiconductor compounds are similar to that of Ge and Si[42]. They also have four-fold degeneracy and Γ_8 symmetry. Accordingly, the acceptor hole-phonon

interaction Hamiltonian is of the same form as that for free holes near the valence band edge[43,44]. From symmetry consideration Hasegawa[45] constructed this Hamiltonian in terms of the angular momentum operator $\overline{J}$ as

$$H = \tfrac{2}{3}D_u^a\left[(J_x^2 - \tfrac{1}{3}J^2)e_{xx} + CP\right] + \tfrac{1}{3}D_{u'}^a\left[(J_xJ_y + J_yJ_x)e_{xy} + CP\right] \quad (4.10)$$

where J_α is the αth component of the angular momentum operator for $J = \frac{3}{2}$ (α = x, y and z referring to the four-fold axes), $e_{\alpha\beta}$ is the conventional strain component, D_u^a and $D_{u'}^a$ are the deformation potential constants of the acceptor states and CP denotes the cyclic permutation of the indices x, y and z. The state $\psi(r)$ of the shallow acceptor can be represented by the Bloch functions $\phi_j(r)$ of the valence band edge and the hydrogenic envelope functions $F_j(r)$ as

$$\psi(r) = \sum_{j=1}^{6} F_j(r)\phi_j(r) \quad (4.11)$$

If we assume that the ground states are identified by the quantum number $M_J(\frac{3}{2}, \frac{1}{2}, -\frac{1}{2}, -\frac{3}{2})$, the corresponding envelope functions are given by:

$$\psi_{M_J} = \phi_{M_J}\left[(\pi a^{*3})^{-\frac{1}{2}}\, e^{-r/a^*}\right] \quad (4.12)$$

where ϕ_{M_J} is the eigen function of M_J and a^* is the effective Bohr radius. By expanding $e_{\alpha\beta}$ in phonon operators, the matrix elements of the hole-phonon interaction between two acceptor states $|n\rangle$ and $|m\rangle$ can be calculated. This calculation will be shown in Appendix 2 for quantization axis in $[110]$ direction, but in this section we are mostly concerned about the phonon relaxation rate due to this interaction. The single-mode relaxation time $\tau_{h\text{-}ph}$ is defined by[46]

$$\frac{1}{\tau_{h\text{-}ph}} = \sum_{q'} W(q \rightarrow q')$$

where $W(q \rightarrow q')$ for the elastic phonon scattering in the second Born approximation is calculated by Suzuki and Nikoshiba[18] and the final relaxation rate caused by acceptor hole-phonon interaction is

$$\tau^{-1}_{h\text{-}ph} = \frac{n_a \omega^2 W}{100 \rho^2 \pi \hbar^2 v_t^2} \left(\frac{2}{3} D^a_{u'}\right)^4 f^2\left(\frac{\omega}{v_t}\right) \left[\frac{f^2\left(\frac{\omega}{v_1}\right)}{v_1^5} + \frac{3}{2} \frac{f^2\left(\frac{\omega}{v_2}\right)}{v_2^5}\right] \qquad (4.13)$$

where n_a is the acceptor concentration, v_1 and v_2 are the average velocities of sound for the longitudinal and transverse modes of the phonon, respectively,

$$W = \tfrac{1}{3}(W_1 + W_2 + W_3)$$

where $W_1 = 24 + 48D^2 + 8D^4$

$W_2 = 16 + 37D^2 + 7D^4$

$W_3 = 20 + 35D^2 + 5D^4$

in which $D = \frac{D^a_u}{D^a_{u'}}$ and $f(q) = (1 + \frac{1}{4}a^{*2}q^2)^{-2}$. By adding $\tau^{-1}_{h\text{-}ph}$ to the total relaxation rate τ^{-1} a good fit for thermal conductivity measurements of p-type sample F ($P = 2.84 \times 10^{15}$ cm^{-3}) was obtained. Fig (29) represents the relaxation rate for each scattering mechanism of this sample. Values of the parameters used in the phonon thermal conductivity calculations are $\rho = 5.8$ gm/cm^3, $a^* = 40A^o$, $D^a_u = 2.6$ eV, $D^a_{u'} = 6.5$ eV, and the velocity of sound is given in sec. 2.3.

Consider now sample G which has a much higher concentration of acceptors. The thermal conductivity data of sample G Fig. (28) obeys the Ziman type T^2 behaviour at the lowest temperature range. To compare the calculated

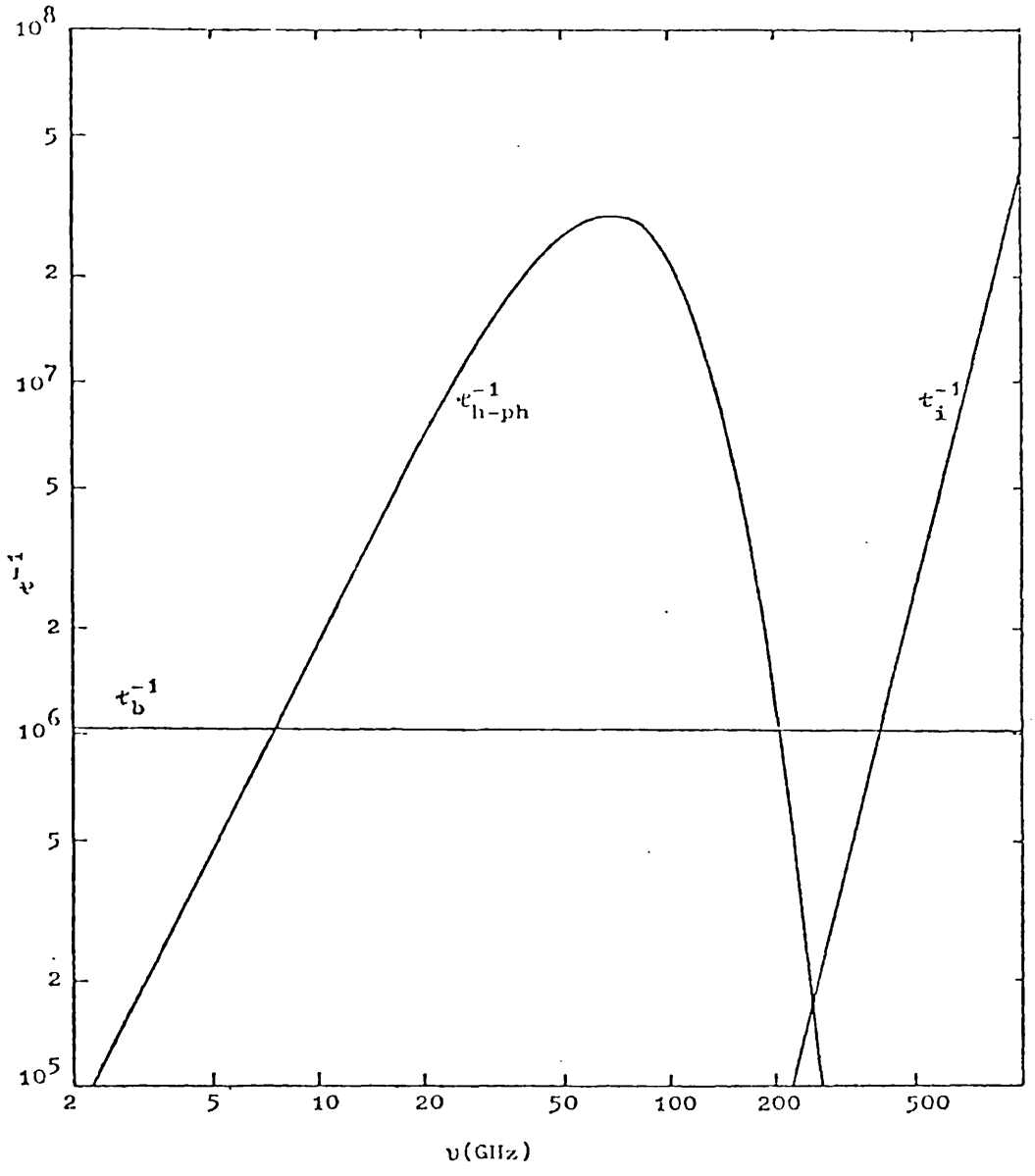

Figure 29. The relaxation rate for boundary, isotope, and hole scattering of phonons.

value for electron-phonon interaction parameters with those found from the best fit, the following approximation is made. We take the region where K varies as T^2, then we neglect the other scattering mechanisms. Hence expression 4.6 becomes:

$$K_{h\text{-}ph} = \frac{k}{2\pi^2 v_s} \left(\frac{kT}{\hbar}\right)^3 \int_0^{\Theta^*/T} \frac{1}{axT} \frac{x^4 e^x dx}{(e^x - 1)^2}$$

or:

$$K_{h\text{-}ph} = \frac{k^4}{2\pi^2 v_s \hbar^3} \frac{T^2}{a} \int_0^{\Theta^*/T} \frac{x^3 e^x}{(e^x - 1)^2} dx \qquad (4.14)$$

The above integral is of the form of Debye integrals J_n.

$$K_{h\text{-}ph} = \frac{k^4}{2\pi^2 v_s \hbar^3} \frac{T^2}{a} J_3\left(\frac{\Theta^*}{T}\right) \qquad (4.15)$$

but for the temperature region where this holds $\Theta^* \gg T$ and $J_3\left(\frac{\Theta^*}{T}\right) \simeq J_3(\infty) = 7.212$. Substituting the above value in (4.15), we get

$$a = \frac{k^4}{2\pi^2 v_s \hbar^3} \cdot \frac{J_3(\infty)}{\left(\frac{K}{T^2}\right)} \qquad (4.16)$$

The measured value for K/T^2 for sample G ($K/T^2 = 0.016 \times 10^7$ erg cm^{-1} deg^{-3} sec^{-1}) is substituted in (4.16), then $a = 1.85 \times 10^6$ $(K\text{-}sec)^{-1}$. The variation of this parameter was very effective on the T^2 region. The isotope scattering term d can alternatively be deduced graphically.

This matches better with experiment and also gives the approximate value of Θ^* as follows:

$$K = \frac{k}{2\pi^2 v_s} \left(\frac{kT}{\hbar}\right)^3 \int_0^{\Theta^*/T} (t'^{-1} + axT)^{-1} \frac{x^4 e^x}{(e^x - 1)^2} dx + \int_{\Theta^*/T}^{\Theta/T} t' \frac{x^4 e^x}{(e^x - 1)^2} dx$$

where τ' represents all scattering other than charge carrier scattering. If the boundary scattering is assumed to be negligible above the Ziman cut-off and τ' is reduced to the isotope scattering ($\tau'^{-1} = dx^4T^4$) then

$$K = \alpha \frac{T^2}{a} J_3\left(\frac{\Theta^*}{T}\right) + \frac{\alpha}{Td} \int_{\Theta^*/T}^{\infty} \frac{e^x dx}{(e^x - 1)^2}$$

where $\frac{\Theta_D}{T} \simeq \infty$

and

$$\alpha = \frac{k^4}{2\pi^2 v_s \hbar^3} = 4.1 \times 10^{10} \ (\text{erg/cm.sec}^2.\text{deg}^{-4})$$

then

$$K = \alpha \frac{T^2}{a} J_3\left(\frac{\Theta^*}{T}\right) + \frac{\alpha}{2Td} e^{-\Theta^*/T}$$

If again we approximate $J_3\left(\frac{\Theta^*}{T}\right) = J_3(\infty) = 7.212$

$$\frac{\alpha}{2Td} e^{-\Theta^*/T} = K - T^2 \times 1.6 \times 10^5$$

then

$$\frac{1}{d} e^{-\Theta^*/T} = \frac{2T}{\alpha} (K - 1.6 \times 10^5 T^2)$$

or

$$\ln d + \frac{\Theta^*}{T} = -\ln \left[\frac{2T}{\alpha} (K - 1.6 \times 10^5 T^2)\right]$$

by plotting $\ln d + \frac{\Theta^*}{T}$ vs $\frac{1}{T}$ we get a straight line, Fig (30) whose slope is equal to Θ^* and its intercept represents $\ln d$. Variation of d and Θ^* in (4.6) was effective in the temperature range above the T^2 region, which is expected. At this stage by using the above numerical values of each parameter, the expression 4.6 can be evaluated numerically. The calculated value of q_{TF} for this sample is 1.9×10^6 cm^{-1} and the effective Debye temperature Θ^* derived from the graph 12.5 deg is in good agreement with

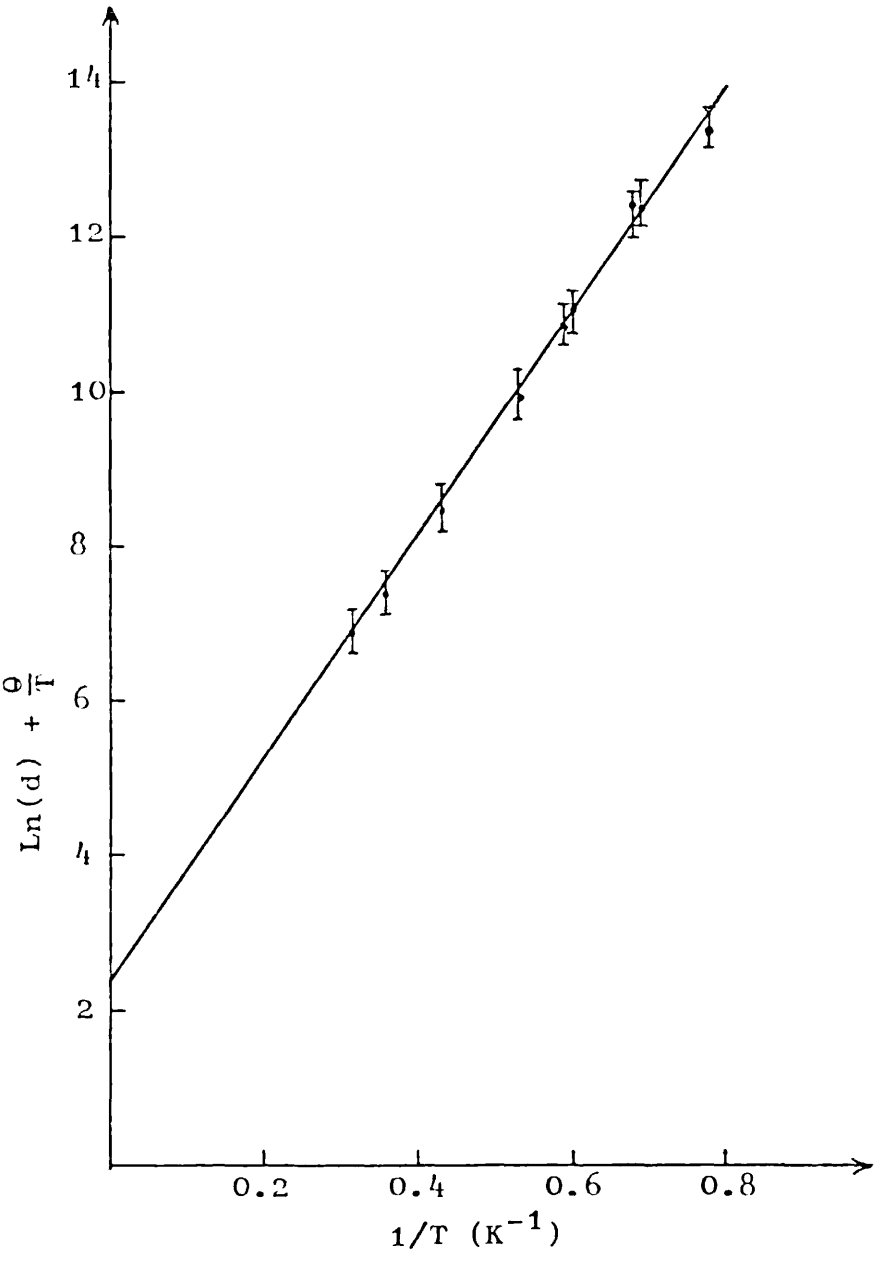

Figure 30. Logarithm of the isotope scattering parameter d plus the ratio of effective Debye temperature Θ^* to temperature T versus reciprocal temperature for sample G.

the calculate value of 11.2 deg which confirms Ziman's theory in a brief range of temperature.

CHAPTER 5

Thermal Conductivity of n-InSb in Magnetic Field

5.1 Introduction

The work described here examines the electron-phonon interaction in n-type indium antimonide at liquid helium temperature using magneto - thermal conductivity measurements. Thermal phonons with large momentum comparable with that of electrons are absorbed and it is convenient to use a magnetic field to isolate the effect of the electron-phonon interaction from other scattering mechanism. In particular, the electronic states in n-InSb are markedly affected by applied field.

Since the effective mass of the electrons in InSb is very small, the contribution of electrons in scattering phonons is also small in thermal conductivity at low temperatures. In a degenerate specimen of InSb when donor states overlap the conduction band (donor concentration $> 5 \times 10^{15}$ cm^{-3}), thermal conductivity show quantum oscillations (see Fig. (31) for raw data of sample D) which are associated with the crossing of the Landau levels through the Fermi level of the electrons, similar to that of de Haas-van Alphen oscillation.

Absorption of phonons occurs only when the change in component of electron wave vector perpendicular to the magnetic field which accompanies the absorption is smaller than the inverse of the cyclotron radius. This allows electron transition within a Landau level to occur only when the bottom of the Landau level is close to the Fermi level.

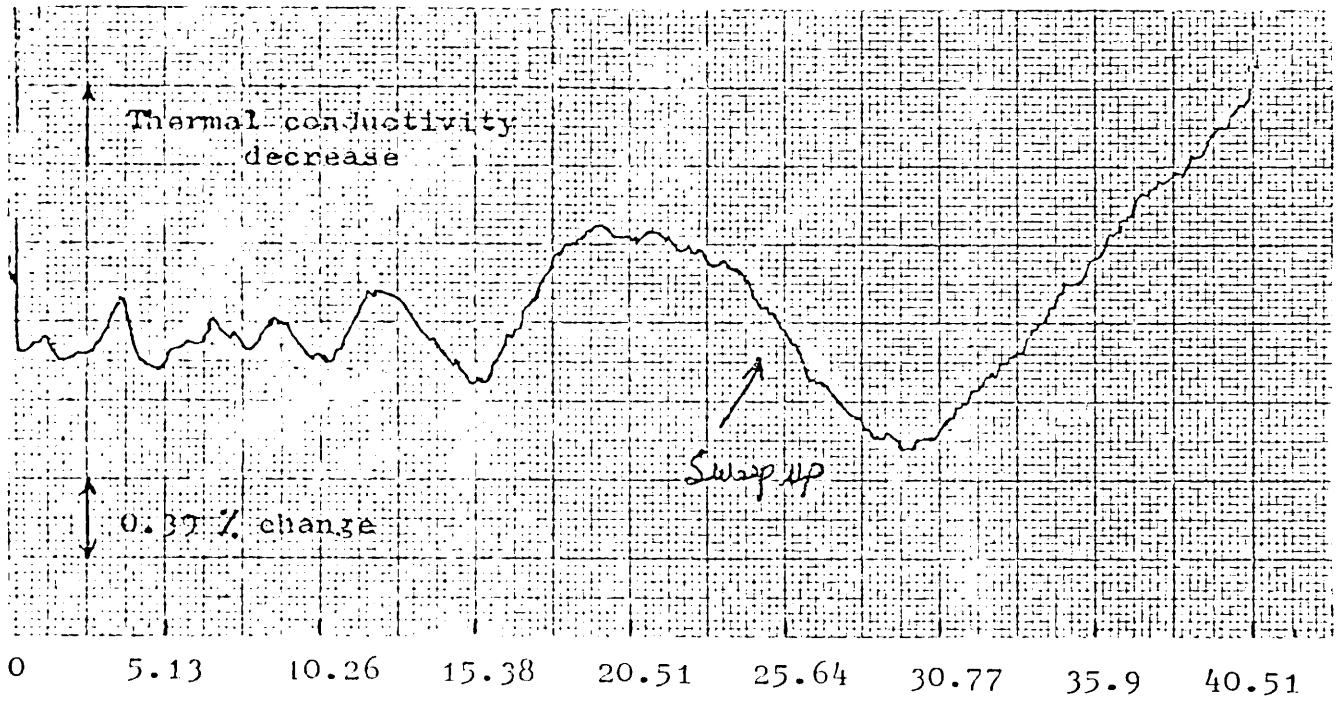

Figure 31. Raw data for magnetic field dependence of thermal conductivity of sample D at 1.3 K.

5.2 Landau Levels

In the presence of an external magnetic field, we form the hamiltonian operator $H = H\left[(\bar{P} + e\bar{A})/\hbar\right]$ and solve the effective Schrodinger equation

$$H\left[(\bar{P} + \frac{e\bar{A}}{c})/\hbar\right]\psi(r) = E\psi(r) \qquad (5.1)$$

Suppose a spherical energy surface with hamiltonian

$$H = \frac{1}{2m^*}(\bar{P} + \frac{e\bar{A}}{c})^2 \qquad (5.2)$$

$$H = \frac{1}{2m^*}(P_x^2 + P_y^2 + P_z^2)$$

It is convenient to take the magnetic field B to be along the z direction and we choose the vector potential $\bar{A}$ as:

$$A_y = -Bx \qquad A_x = A_z = 0$$

then

$$P_x = \frac{\hbar}{i}\frac{\partial}{\partial x} \qquad P_y = \frac{\hbar}{i}\frac{\partial}{\partial y} - eBx \qquad P_z = \frac{\hbar}{i}\frac{\partial}{\partial z} \qquad (5.3)$$

with these simplification equations (5.1) takes the form

$$-\frac{\hbar^2}{2m^*}\left[\frac{\partial^2}{\partial x^2} + (\frac{\partial}{\partial y} - ieBx/\hbar)^2 + \frac{\partial^2}{\partial z^2}\right]\psi(r) = E\psi(r) \qquad (5.4)$$

This equation is separable in rectangular coordinates.

Let us put

$$\psi(r) = \exp\left[i(k_y y + k_z z)\right] g(x) \qquad (5.5)$$

This leads to

$$(d^2g/d^2x) + (2m^*/\hbar^2)\left[E - (\hbar^2 k_z^2/2m^*) - (\frac{1}{2m^*})(\hbar k_y - eBx)^2\right]g(x) = 0 \qquad (5.6)$$

It is convenient to define the classical cyclotron radius λ as:

$$\lambda^2 = \frac{c\hbar}{eB}$$

and

$$\omega_c = \frac{eB}{m^*c}$$

then the above equation may be written as

$$\left(\frac{d^2g}{dx^2}\right) + \left(\frac{2m^*}{\hbar^2}\right)\left[\varepsilon - \tfrac{1}{2}m^*\omega_c^2\,(x - \lambda^2 k_y)^2\right] g(x) = 0 \qquad (5.7)$$

where $\varepsilon = E - \dfrac{\hbar^2 k_z^2}{2m^*}$. This is an equation for a simple harmonic oscillator of frequency ω_c, with the eigen value E_n given by

$$E_1 = (n + \tfrac{1}{2})\hbar\omega_c$$

where n is a positive integer including zero (n = 0, 1, 2..), and the quantity ω_c is called the cyclotron frequency. The total energy of an electron in a magnetic field (when the spin is neglected) is given by

$$E = \frac{\hbar^2 k_z^2}{2m^*} + (n + \tfrac{1}{2})\hbar\omega_c \qquad (5.8)$$

and it is apparent the result is quite remarkable because a three-dimensional, parabolic band structure from which we started has been split up into a series of the oscillator levels which can be associated with the classical circular motion of the electron in a plane perpendicular to the magnetic field, plus a one-dimensional parabolic term coming from the free electron motion in a direction parallel to the field. These discrete levels are called Landau levels, and the energy of the lowest state is no longer zero, but has been raised to $\frac{1}{2}\hbar\omega_c$. These levels are separated by an energy

$$\hbar\omega_c = \frac{\hbar eB}{m^*c} = 1.1577 \times 10^{-8}\,\frac{B}{(m^*/m)}\ \text{eV}$$

where B is in gauss and m_o is the free electron mass. This energy is large for materials with small effective mass ratio of the order of 10^{-2} (InSb, Bi, etc.) in strong fields and the formation of the Landau levels becomes quite significant. For low fields and for materials with effective mass ratios of the order of unity, this energy is small compared to thermal energies except at the very lowest temperatures. If we add the effect of the spin to the picture, another term representing the interaction of the electron spin with the magnetic field will be added to the hamiltonian of equation (5.2) which is given by

$$(\frac{e\hbar}{m_o})\ \overline{s}\ .\ \overline{B}$$

and consequently the energies are

$$E = (\frac{\hbar^2 k_z^2}{2m^*}) + (n + \tfrac{1}{2})\hbar\omega_c + (\frac{e\hbar}{m_o})\ Bs \qquad (5.9)$$

where s is the spin quantum number ($s = \pm \frac{1}{2}$). Here we note that the free electron mass m_o enters into the spin term, whereas the effective mass m^* enters into the cyclotron frequency. We may also note that as a result of the spin term, we find that if $m^* \simeq m_o$, the energy of the lowest state is $E = 0$, that is, the lowering of energy caused by alignment of the spin cancels the increase produced by confinement of an electron to an orbit. However, in indium antimonide $m^* \ll m_o$, and one effect or the other may predominate. The preceding representation is a somewhat over-simplified picture of the spectrum particularly in indium antimonide where spin-orbit coupling is significant, and the g factor of the electron departs significantly from 2. The calculations of g factor has

been reviewed by Yafat[17], and simplified recently by de Graaf and Overhauser[47].

5.3 Magnetic Field Effect on Electron-Phonon Interaction

Here we consider the electron-phonon interaction Hamiltonian through the deformation potential C as:

$$H' = C\left(\frac{\hbar}{2A^3\rho}\right)^{\frac{1}{2}} \sum_q \frac{q}{\omega_q^{\frac{1}{2}}} (\bar{a}_q + \bar{a}_q^*) e^{i\bar{q}\cdot\bar{r}} \qquad (5.10)$$

where $\bar{a}$ and $\bar{a}^*$ are the creation and annihilation operators of the phonon with wave vector $\bar{q}$, and as explained in section 5.2 since P_y, P_z commute with H the corresponding eigen function for Hamiltonian (5.2) can be easily written as:

$$\psi_{nk_yk_z} = A^{-1} \exp\left[i(k_y y + k_z z)\right] \phi_n (x - \lambda^2 k_y) \qquad (5.11)$$

where A is the normalization constant. The rate of phonon absorption by an electron (n, k_y, k_z, s) being scattered to the state (n', k_y', k_z', s) can be calculated using the standard time-dependent perturbation theory in the lowest order.

$$\langle \psi^*_{nk_yk_zs} \left| H' \right| \psi_{mk_y'k_z's'} \rangle = \delta(k_y + q_y - k_y') \cdot$$

$$\delta(k_z + q_z - k_z') \delta_{ss'} \int_{-\infty}^{+\infty} dx e^{iq_x x} \phi_n^*(x - \lambda^2 k_y) \phi_m(x - \lambda^2 k_y') \qquad (5.12)$$

Here we assume $\bar{q} = q\ (0, 0, 1)$. The integration over x gives

$$\int_{-\infty}^{+\infty} e^{iq_x x} \phi_n^*(x) \phi_m(x) dx = \exp\left(-\frac{\lambda^2 q_x^2}{4}\right) \left(\frac{i\lambda q_x}{\sqrt{2}}\right)^{n-m} (m!/n!)^{\frac{1}{2}} L_m^{n-m}\left(\frac{\lambda^2}{2}\right) \qquad (5.13)$$

where L_m^n is the Laguerre bi-polynomial and the right hand

side is valid for $n \gg m$. The equation (5.12) takes the following form

$$\langle \psi_{nk_y k_z s} | H' | \psi_{mk_y k_z s'} \rangle = \delta_{ss'} \delta(k_y - k_y') \delta(k_z + q - k_z') \cdot \exp(-\frac{\lambda^2}{4} q_x^2) \cdot$$

$$(\frac{\lambda I_x}{\sqrt{2}})^{n-m} (m!/n!)^{\frac{1}{2}} L_m^{n-m} (\frac{\lambda^2 q_x^2}{2}) \qquad (5.14)$$

with $L_m^{n-m}(x) = \sum_{p=0}^{m} (-1)^p \frac{n!}{(m-p)!(p+n-m)!} \frac{1}{p!} x^p$

The rate of absorption is obtained by

$$W(q,n,k_z,s \longrightarrow 0,m,k_z + q,s) = (2\pi/\hbar)(C^2 \hbar q^2 / 2A^3 \rho \omega_q) \cdot$$

$$F_{nm}(\frac{\lambda^2 q_x^2}{2}) \delta(\hbar\omega_q + E(n,k_z,s) - E(m,k_z+q,s)) \qquad (5.15)$$

where

$$F_{nm}(x) = e^{-x} x^{n-m} (m!/n!) \left[L_m^{n-m}(x) \right]^2$$

This function is = 1 for $n = m$ and = 0 for $n \neq m$, now if we sum the absorption rate over the initial and final electron states:

$$W_{n=m}^{s}(q) = (A^3/4\pi^2\lambda^2) \int W(q,n,k_z,s \longrightarrow 0,n,k_z+q,s) f_{n,k_z,s} \cdot$$

$$(1 - f_{n,k_z,+q,s}) dk_z$$

where $f_{n,k_z,s}$ is the Fermi distribution function for the electron state of (n, k_z, s). And finally the relaxation rate of electron-phonon interaction is given by

$$\tau^{-1} = \sum_{n=m,s} W_n^s(q)$$

Now, the absorption rate (5.15) can be calculated in detail in the following:

$$W(1,n,k_z,s \longrightarrow 0,n,k_z+q,s) = (2\pi/\hbar)(C^2\hbar q^2/2A^3\rho qv)\cdot$$
$$\delta(\hbar qv+E(n,k_z,s)-E(n,k_z+q,s)) \qquad (5.16)$$

If we substitute for energies from equation (5.9) section 5.2 in the deltafunctions we get:

$$W = \frac{\pi C^2 q}{A^3 \rho v_s}\ \delta\left(\hbar qv - \frac{\hbar^2 q^2}{2m^*} - \frac{\hbar^2 q k_z}{m^*}\right) \qquad (5.17)$$

Since the delta function is an even function the above result can be simplified as

$$W = \frac{\pi C^2 q}{A^3 \rho v_s}\ \delta\left[\frac{\hbar^2 q}{m^*}\left(k_z - \frac{v_s m^*}{\hbar} + \frac{q}{2}\right)\right] \qquad (5.18)$$

or

$$W = \frac{\pi C^2 m^*}{A^3 \rho v_s \hbar^2}\ \delta(k_z - k_o) \qquad (5.19)$$

where

$$k_o = \frac{v_s m^*}{\hbar} - \frac{q}{2}$$

By summing over the initial and final state of the electrons the relaxation rate becomes

$$t^{-1} = \sum_{n,s} \frac{A^3}{4\pi^2\lambda^2} \int \frac{\pi C^2 m^*}{A^3 \rho \hbar v}\ \delta(k_z - k_o) f_{n,k_z,s}\ (1 - f_{1,k_z+q,s})\, dk_z$$

which is

$$t^{-1} = \frac{C^2 m^*}{4\pi\rho\hbar^2\lambda^2 v} \sum_{n,s} f_{n,\frac{m^*v}{\hbar}-\frac{q}{2},s} \left(1 - f_{n,\frac{m^*v}{\hbar}+\frac{q}{2},s}\right) \qquad (5.20)$$

The Fermi distribution function is defined by

$$f_{n,k_z} = 1/\left\{\exp\left[\left(\frac{\hbar^2 k_z^2}{2m^*} - \varepsilon_{n,s}\right)/kT\right] + 1\right\} \qquad (5.21)$$

where

$$\varepsilon_{n,s} = E_F - \left[\left(n + \tfrac{1}{2} + \tfrac{1}{2}\gamma s\right)\hbar\omega_c\right] \qquad (5.22)$$

with

$$\gamma = \frac{\text{spin splitting}}{\text{Landau level splitting}} = \frac{\hbar\omega_s}{\hbar\omega_c} = \frac{g\mu_e B}{\hbar\omega_c} \qquad (5.23)$$

substituting for each parameter we get

$$\gamma = -0.32$$

To calculate the relaxation rate (5.20) each Fermi function in the summation must be determined as

$$f_{n,\frac{m^*v}{\hbar}-\frac{q}{2},s} = 1/\left(\exp\left\{\left[\frac{\hbar^2}{2m^*}\left(\frac{m^*v}{\hbar} - \frac{q}{2}\right)^2 + \left(n+\tfrac{1}{2}+\tfrac{1}{2}\gamma s\right)\hbar\omega_c - E_F\right]/kT\right\} + 1\right) \qquad (5.24)$$

A similar expression can be derived for $(1-f_{n,\frac{m^*v}{\hbar}+\frac{q}{2},s})$ and substitution of these in (5.20) determines the final relaxation rate of electron-phonon scattering in a magnetic field.

$$t_{e\text{-}ph}^{-1} = \frac{C^2 m^*}{4\pi\rho\hbar^2\lambda^2 v} \sum_{n,s} \left[1/\left(\exp\left\{\left[\left(\frac{m^*v_s^2}{2} + \frac{x^2k^2T^2}{8m^*v^2} - \frac{xkT}{2}\right) + \left(n+\tfrac{1}{2}+\tfrac{1}{2}\gamma s\right)\hbar\omega_c - E_F\right]/kT\right\} + 1\right)\right] \cdot \left[\exp\left\{\left[\left(\frac{m^*v_s^2}{2} + \frac{x^2k^2T^2}{8m^*v^2} + \left(n+\tfrac{1}{2}+\tfrac{1}{2}\gamma s\right)\hbar\omega_c - E_F\right]/kT\right\}/\left(\exp\left\{\left[\left(\frac{m^*v_s^2}{2} + \frac{x^2k^2T^2}{8m^*v^2} + \frac{xkT}{2}\right) + \left(n+\tfrac{1}{2}+\tfrac{1}{2}\gamma s\right)\hbar\omega_c - E_F\right]/kT\right\} + 1\right)\right] \qquad (5.25)$$

where $x = \frac{\hbar q v_s}{kT}$, m^* is the electron effective mass and v_s is the velocity of sound for longitudinal mode since only the longitudinal phonon mode is scattered by electrons in each Landau level.

5.4 Measurements and Experimental Results of Thermal Conductivity in Magnetic Field

Magnetothermal conductivity measurements of four n-type indium antimonide samples was made in the temperature range of (1.2 - 2K). The experimental procedure was explained in section 3.6, and the only point which has to be mentioned here is that in order to reduce the noise level in the output signal of the lock-in-amplifier the time constant and sweeping time was increased to an optimum value which permitted a very stable ambient temperature and an output signal which did not lag behind the magnetic field. The variations of the thermal conductivity with magnetic field at various fixed temperature is plotted for the n-type samples in figures (32-34). The data obtained for sample B (see Fig. (32)) with low donor concentration showed no change in thermal conductivity due to magnetic field. This confirms the basic assumption that the effect observed in the doped samples is correlated with the concentration of n-type impurities and is due to the electron-phonon interaction. No oscillations are observed in sample C. This sample has a concentration $N_D - N_A = 4.4 \times 10^{15}$ cm^{-3} such that the extreme quantum limit with the electrons occupying the lowest Landau level, is reached with a field as low as

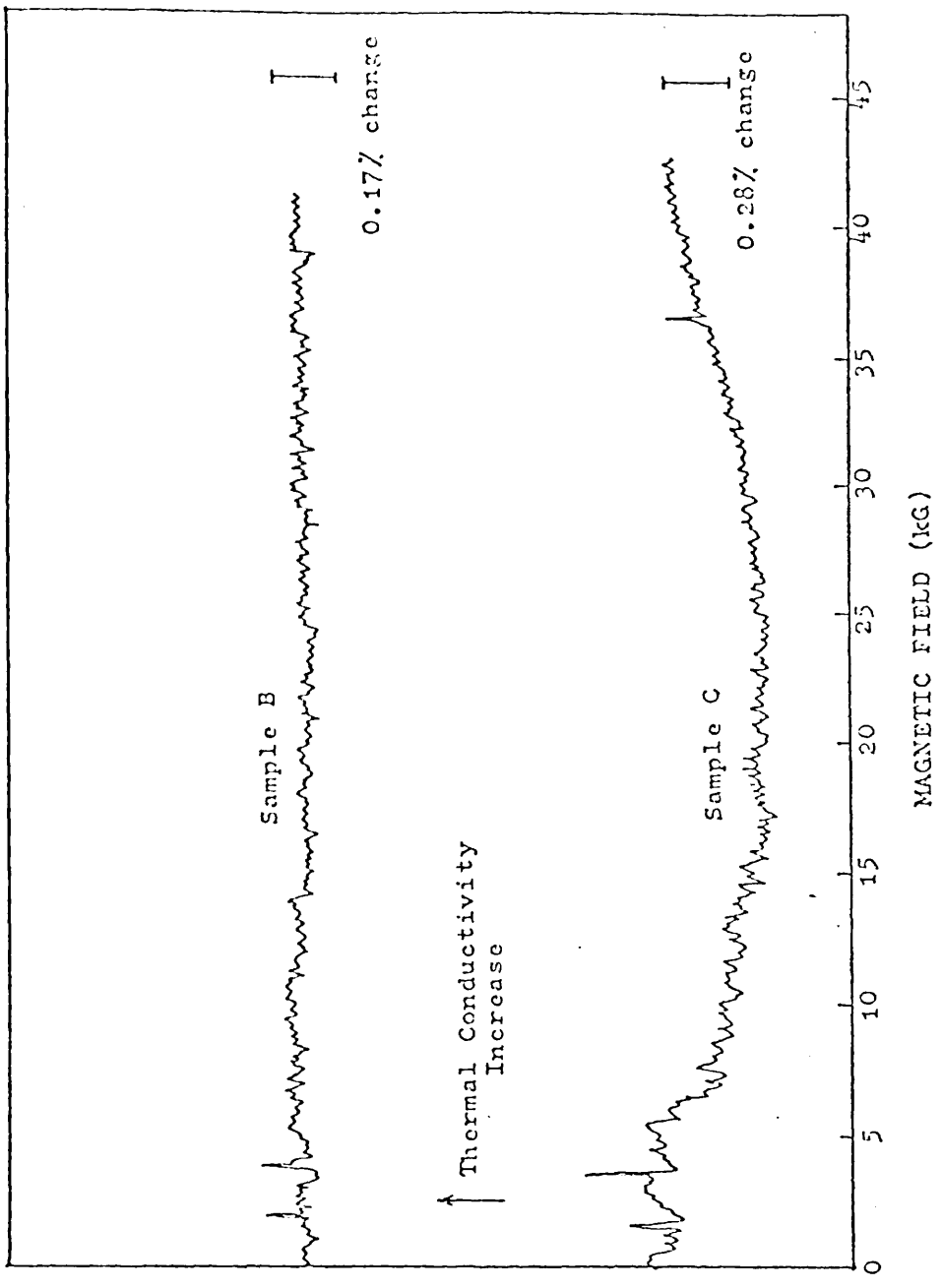

Figure 32. Magnetic field dependence of thermal conductivity of sample B and C with donor concentrations $n=3.05\times10^{14}$ and $n=4.4\times10^{15}$ cm^{-3} respectively at 1.28 K.

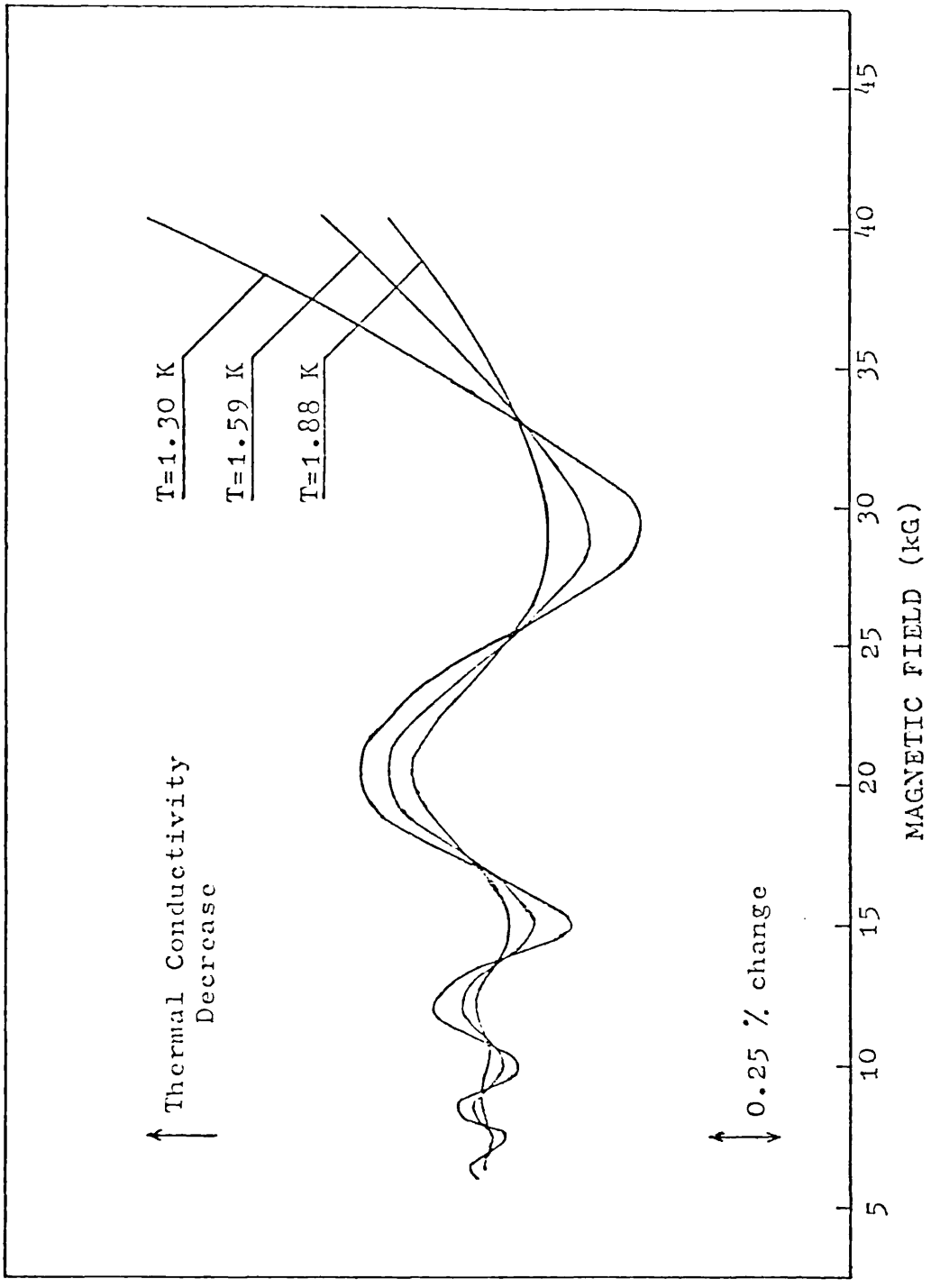

Figure 33. Magnetic field dependence of thermal conductivity of sample D with donor concentration $n=3.5\times10^{16}$ cm^{-3} at several temperatures.

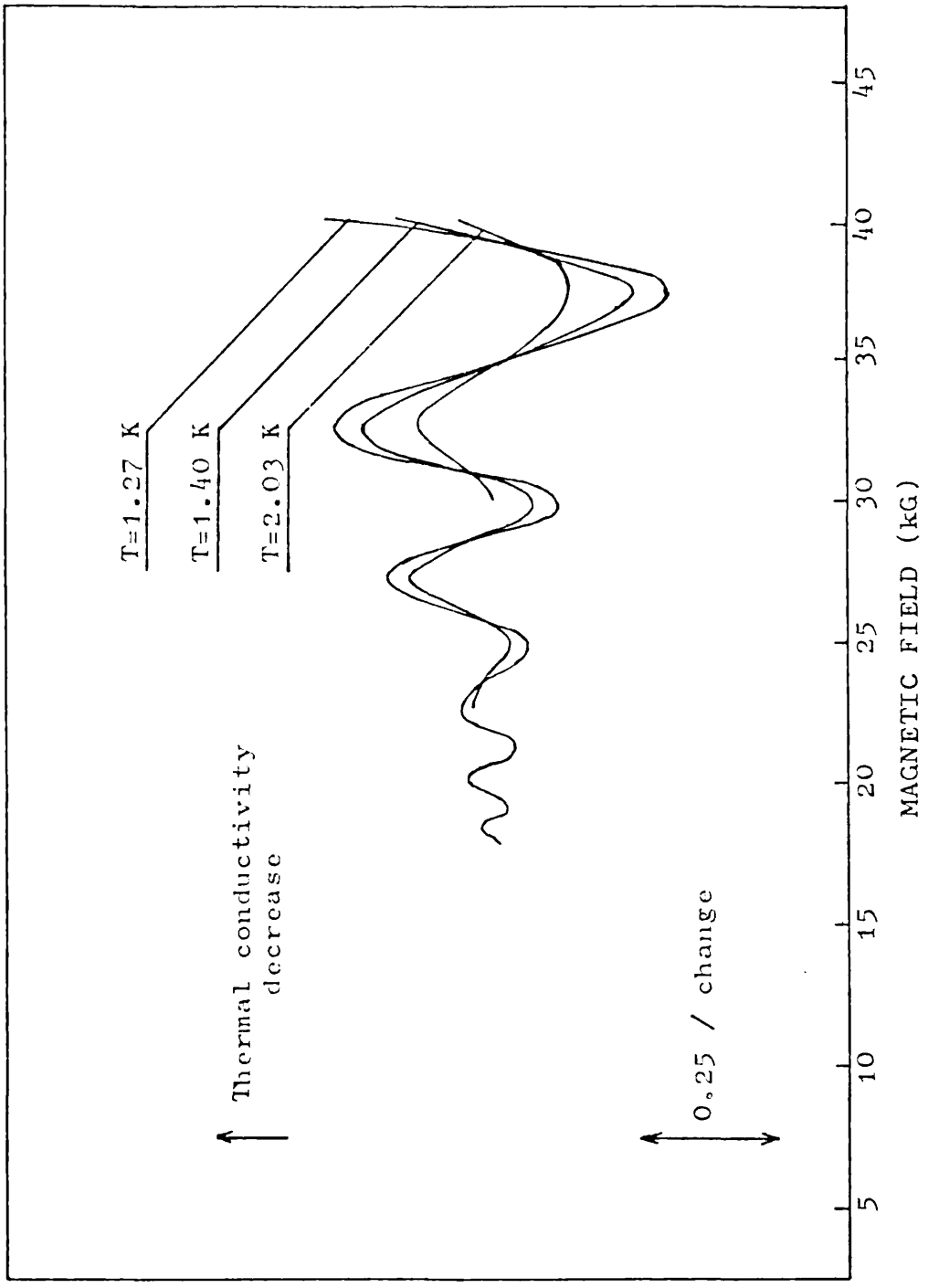

Figure 34. Magnetic field dependence of thermal conductivity of sample E with donor concentration $n=1.2\times10^{17}$ cm^{-3} at several temperatures.

10 kG. There is however a small decrease in thermal conductivity of about 0.3% as the field is increased to 40 kG. But as the impurity concentration is increased the effect of the magnetic field is enhanced, and the thermal conductivity of samples D and E oscillate with the magnetic field. The periods of the oscillation are similar to those of the Shubnikov-de Haas oscillations. However, the amplitude of the oscillations are small and the maximum change of the thermal conductivity at 40 kG for sample D is just 1%.

5.5 Shubnikov-de Haas Oscillation in More Heavily Doped Samples

There is a direct correspondence between magneto-thermal resistivity oscillation and the Shubnikov-de Haas oscillation of magnetoresistance of heavily doped samples. however the cause of these two effects is quite different. The Shubnikov-de Haas effect is one of a series of similar effects which includes the de Haas-van Alphen effect in which the magnetic susceptibility oscillates with field.

The density of states oscillate in the applied magnetic field (Fig. (35))[50] due to the quantization of electron motion. There is an abrupt change of the density of states at each Landau level. For a degenerate semiconductor the electrical resistivity is determined by the scattering of electrons with energy close to the Fermi energy, and when the Landau levels cross the Fermi level there is a sudden change in electron scattering due to the change in the density of states at Fermi level. Consequently there

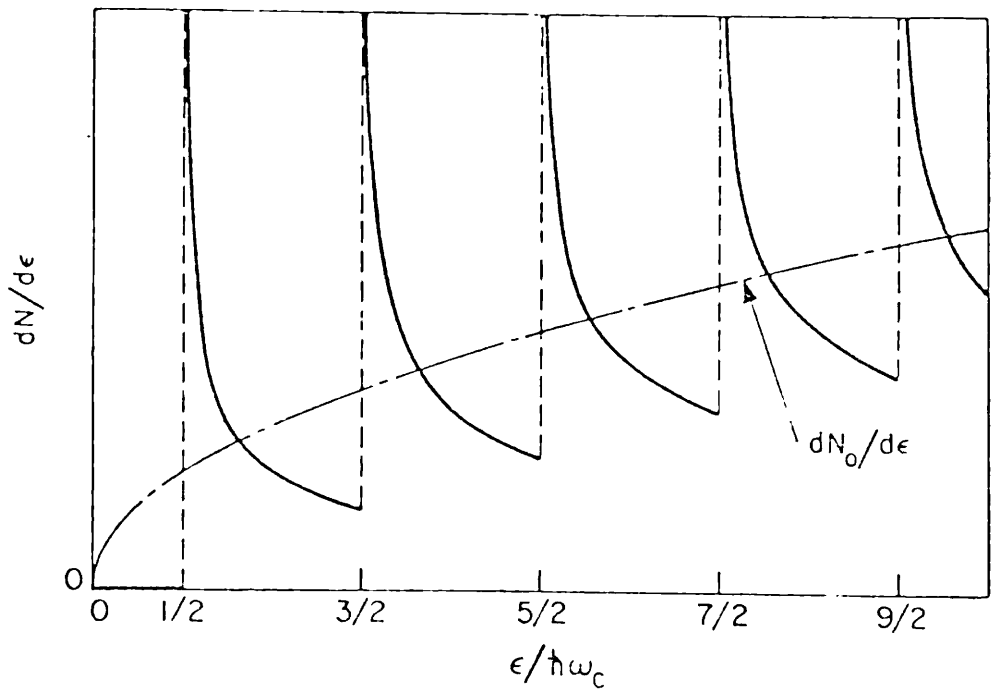

Figure 35. Density of states in the presence of a magnetic field. The zero field case is also shown. (From reference 50)

is an oscillation in the resistivity which is the Shubnikov-de Haas effect. The oscillation occurs according to

$$1/B = (2e\pi/\hbar cA)(n + \tfrac{1}{2}) \qquad (5.27)$$

where A is the area of the cross section of the Fermi sphere in the momentum space and the effect of spin has been neglected. In a longitudinal magnetic field the oscillating part of the resistivity is shown to be[49]

$$\frac{\rho-\rho_o}{\rho_o} = \left(\frac{\hbar\omega_c}{2E_F}\right)^{\frac{1}{2}} \frac{y}{\sinh y} \cos(\gamma\pi)\exp\left(\frac{-2\pi^2 k\, T_D}{\hbar\omega_c}\right) \cdot \sin(F+\phi) \qquad (5.28)$$

$$\text{where } y = \frac{2\pi^2 kT}{\hbar\omega_c},\ T_D = \hbar/\pi kt \text{ and } F = \frac{\hbar c}{2e}k_F^2 \qquad (5.29)$$

is the frequency of the oscillation. T_D is called the Dingle temperature and γ is defined in expression (5.23).

The amplitude of the oscillation depends on thermal broadening through the term y and at low temperature where $y \ll 1$ then $y/\sinh y \simeq 1$ and the amplitude of the oscillation become independent of the temperature.

Measurements of magneto-resitance of a specimen similar to sample D revealed oscillation with period identical to that observed in magneto-thermal resistivity. The amplitude of the oscillation in these two measurements is quite different as expected, and also the oscillation of magnetoresistance showed a monotonic change which was not present for the magneto-thermal resistivity. Figure (36) compares the types of oscillations.

5.6 Analysis of the Result

The oscillatory magneto-thermal resistance effect observed in InSb have been treated according to theory

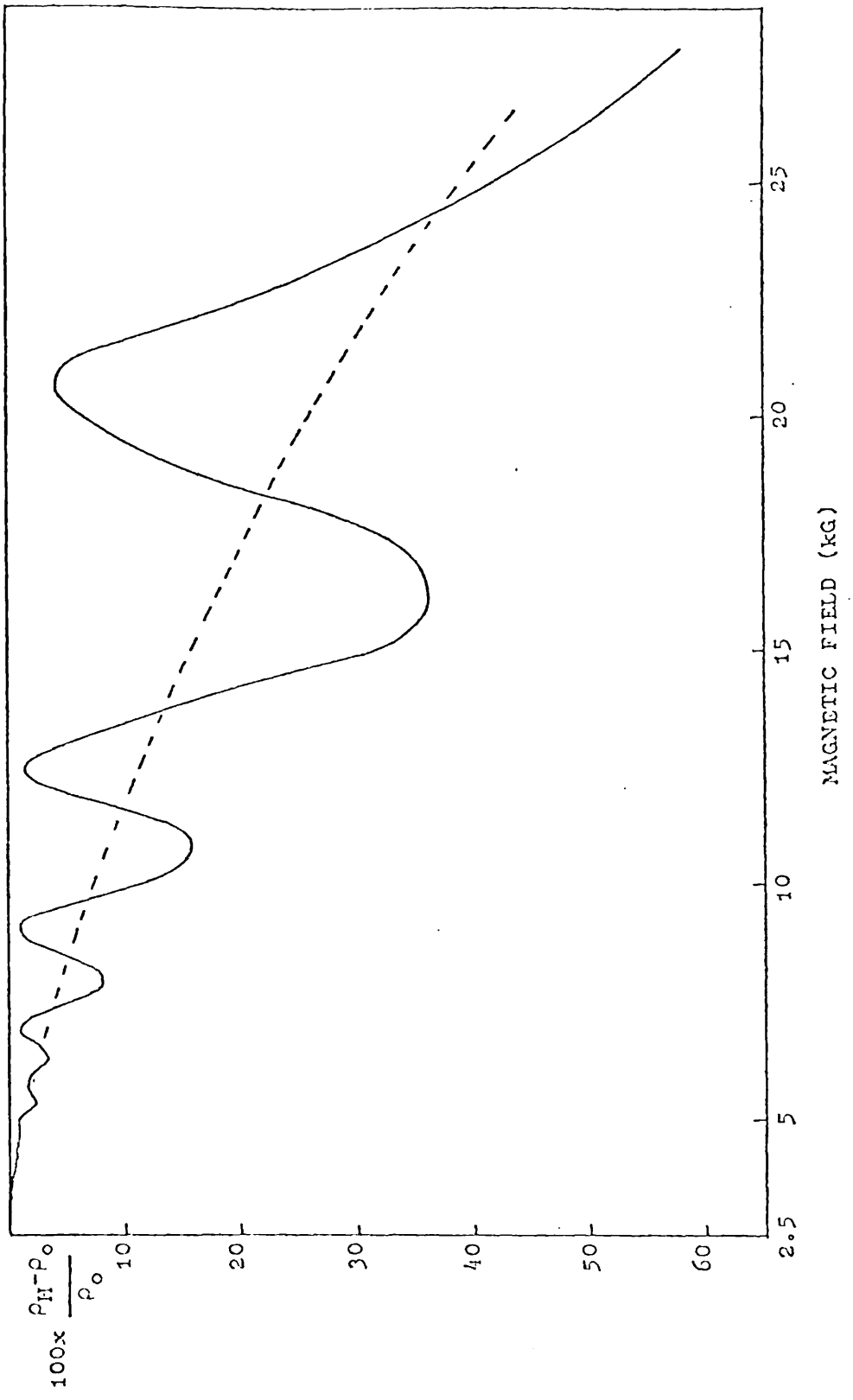

Figure 36. Longitudinal magnetoresistance of sample D with donor concentration $n=3.5\times10^{16}$ cm^{-3} at 2.9 K.

given in section 5.3. Since this oscillation in thermal conductivity is just due to the scattering of phonons by electrons in different Landau levels the amplitude of the oscillation depends directly on the strength of this interaction for each sample. The amplitude of the oscillation also depends on which Landau level is crossing the Fermi level. Figure (37) shows a plot of the 1/B values for maximum and minimum values of thermal resistivity of sample D versus integers which is identical to that of electrical resistivity measured at 2K.

In order to include the relaxation rate (5.25) in the thermal conductivity integral, values of τ_{e-ph}^{-1} were calculated separately to check whether the oscillatory effect was significant or not, and to do so the calculation of the allowed phonon wavevector was required. Electron transitions occur only in the same Landau level by absorption of a phonon with certain wavevector $\bar{q}$ in the vicinity of the Fermi level, and the electron system is transparent for the rest of the phonon spectrum. Figure (38) illustrates the allowed phonon wavevector for electron transition in nth Landau level :

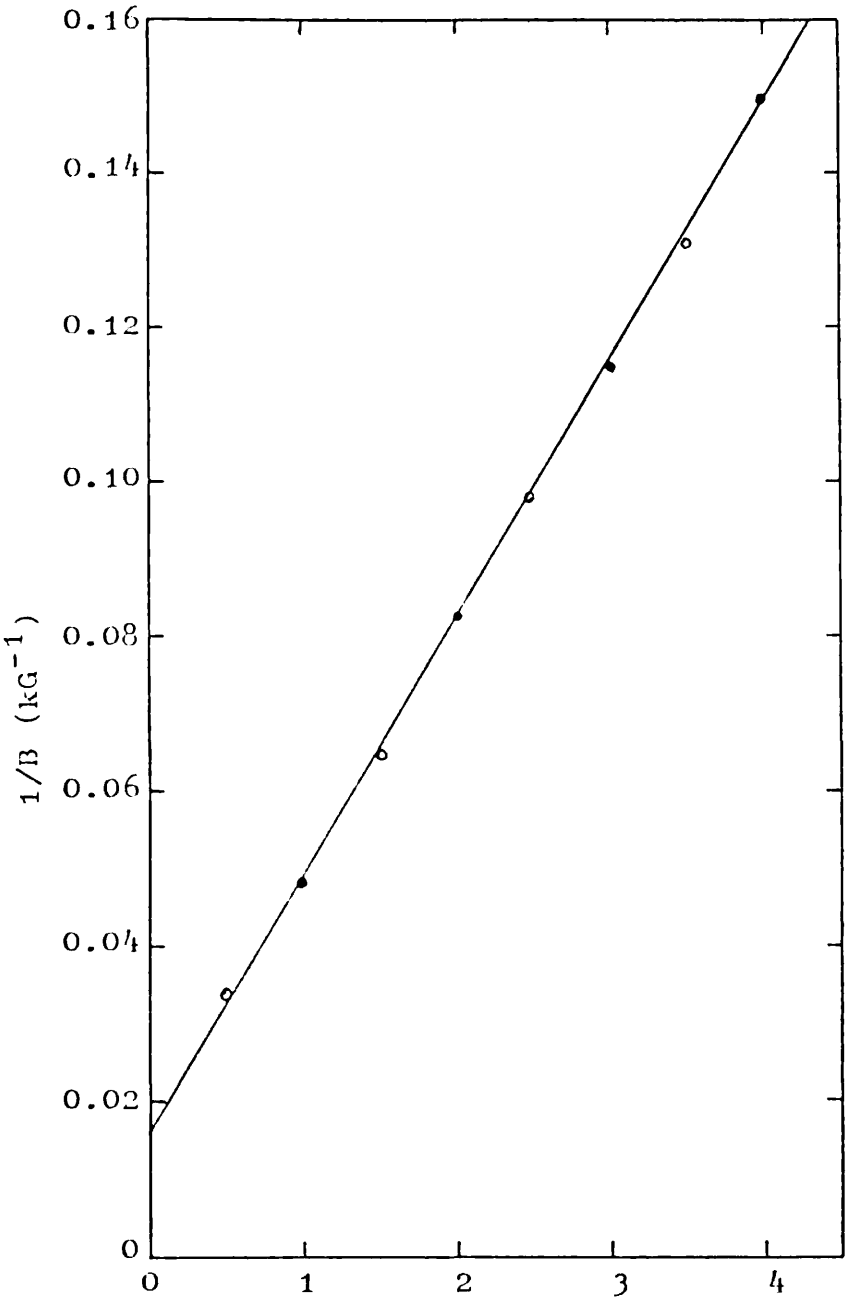

Figure 37. Inverse magnetic field for maxima and minima of magnetothermal conductivity versus integers.

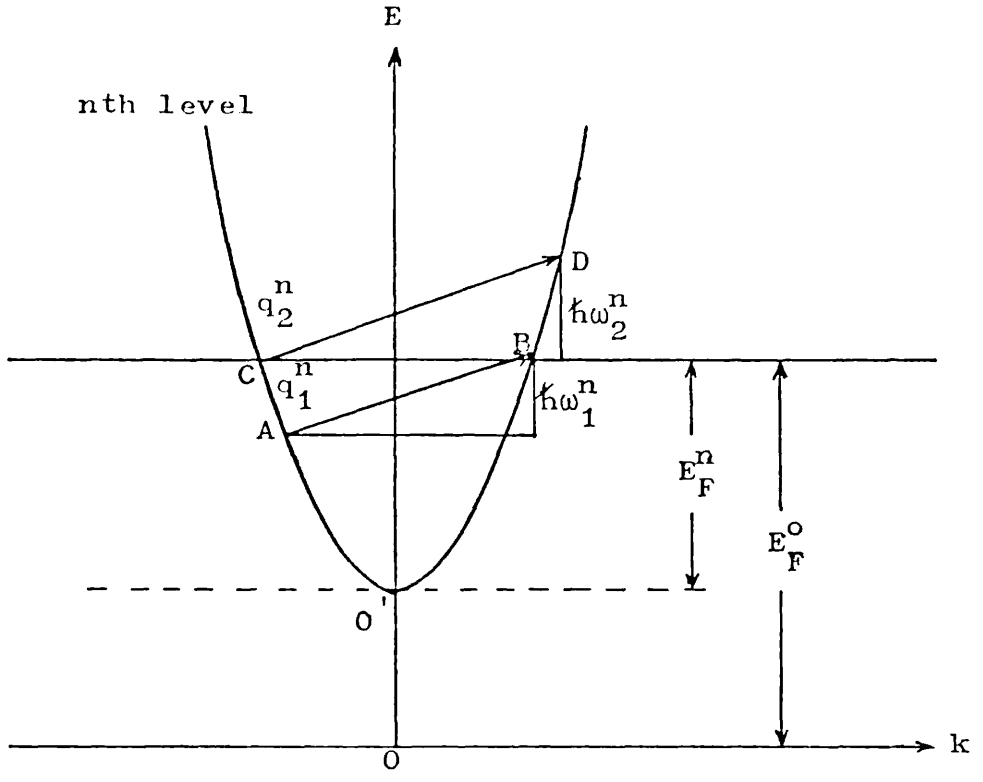

Figure 38. Allowed phonon wavevectors for electron transition in nth Landau-level.

$$q_1^n < q < q_2^n \tag{5.30}$$

where q_1^n represents a phonon absorbed by an electron which is excited from A, below the Fermi level to B close to the Fermi level and q_2^n to excitation from C, at the Fermi level to D.

Then the following assumption is made:

$$E_F^o = \frac{\hbar^2 k_F^{2n}}{2m^*} + (n + \tfrac{1}{2})\hbar\omega_c$$

$$\text{then } \frac{\hbar^2 k_F^{2n}}{2m^*} = E_F^n = E_F^o - (n + \tfrac{1}{2})\hbar\omega_c \tag{5.31}$$

If the origin is transferred to O' the coordinates of point A and B with respect to energy and wavevector axis are:

$$A(E,\ k)=(E_F^n - \hbar\omega_1^n,\ -(\frac{2m^*}{\hbar^2})^{\frac{1}{2}}\ \sqrt{E_F^n - \hbar\omega_1^n}) \tag{5.32}$$

because $E_F^n - \hbar\omega_1^n = \frac{\hbar^2 k^2}{2m^*}$

$$B(E,\ k) = (E_F^n,\ +\ k_F^n) \tag{5.33}$$

q_1^n may be obtained as:

$$q_1^n = q_B - q_A = k_F^n + (\frac{2m^*}{\hbar^2})^{\frac{1}{2}}\ \sqrt{E_F^n - \hbar\omega_1^n} \tag{5.34}$$

using $\hbar\omega_1^n = \hbar q_1^n v_s$

$$(q_1^n - k_F^n)^2 = (\frac{2m^*}{\hbar^2})(E_F^n - \hbar v_s q_1^n) \tag{5.35}$$

and finally q_1^n is determined from second order equation (5.35) as:

$$q_1^n = 2k_F^n - \frac{2m^*}{\hbar}\ v_s$$

substituting for k_F^n from (5.31)

$$q_1^n = 2(\frac{2m^*}{\hbar^2})^{\frac{1}{2}}\ \left[E_F^o - (n + \tfrac{1}{2})\hbar\omega_c\right]^{\frac{1}{2}} - \frac{2m^*}{\hbar}\ v_s \tag{5.36}$$

using the coordinate of points C and D and following the same procedure as above q_2^n can be obtained:

$$C(E_F^n\ ,-k_F^n)$$

$$D(E_F^n + \hbar\omega_2^n,\ +\ (\frac{2m^*}{\hbar^2})^{\frac{1}{2}}\sqrt{E_F^n + \hbar\omega_2^n})$$

then

$$q_2^n = 2(\frac{2m^*}{\hbar^2})^{\frac{1}{2}}\ \left[E_F^o - (n + \tfrac{1}{2})\hbar\omega_c\right]^{\frac{1}{2}} + \frac{2m^*}{\hbar}\ v_s \tag{5.37}$$

In addition to the condition (5.30) the phonon wavevector must satisfy the following requirement:

$$q < q_{cr} \simeq \lambda^{-1} \tag{5.38}$$

q_{cr} is slowly varying with B, but q_1^n and q_2^n decrease rapidly with increasing B as the bottom of the n-th Landau level approaches the Fermi level. As the field strength is changed, the range of phonon wavevector satisfying equation (5.30) also changes, but such phonons can be always found in the broad thermal phonon spectrum. However, satisfying equation (5.38) explains why absorption is strong only for small ranges of the field strength and is nearly zero for other fields despite the fact that a broad phonon spectrum is present. Thus, at fields such that $q_{cr} < q_1^n$, the two requirements (5.30) and (5.38) cannot be satisfied, and so no phonon is absorbed. As the field increases and becomes such that $q_1^n < q_{cr} < q_2^n$, only phonons whose wavevector satisfies $q_1^n < q < q_{cr}$ are absorbed. When the field increases more (q_1^n decreases), the range of q satisfying this inequality increases. At fields which allow $q_2^n < q_{cr}$, all the phonons satisfying (5.30) are absorbed. Finally when the field increased so that the bottom of the Landau level coincides with the Fermi level, the total absorption suddenly decreases, and this process goes on for each Landau level. Using expression (5.25) to calculate τ_{e-ph}^{-1} at T = 1.298K and also neglecting spin figure (39) was obtained for sample D which represents the variation of electron-phonon scattering rate for each Landau level with magnetic field. In order to compare the strength of this interaction with the other scattering mechanisms, all are plotted against the phonon frequency υ in figure (40) which reveals that electron-phonon scattering in only predominant in a very short interval of phonon spectrum and the interaction is stronger when

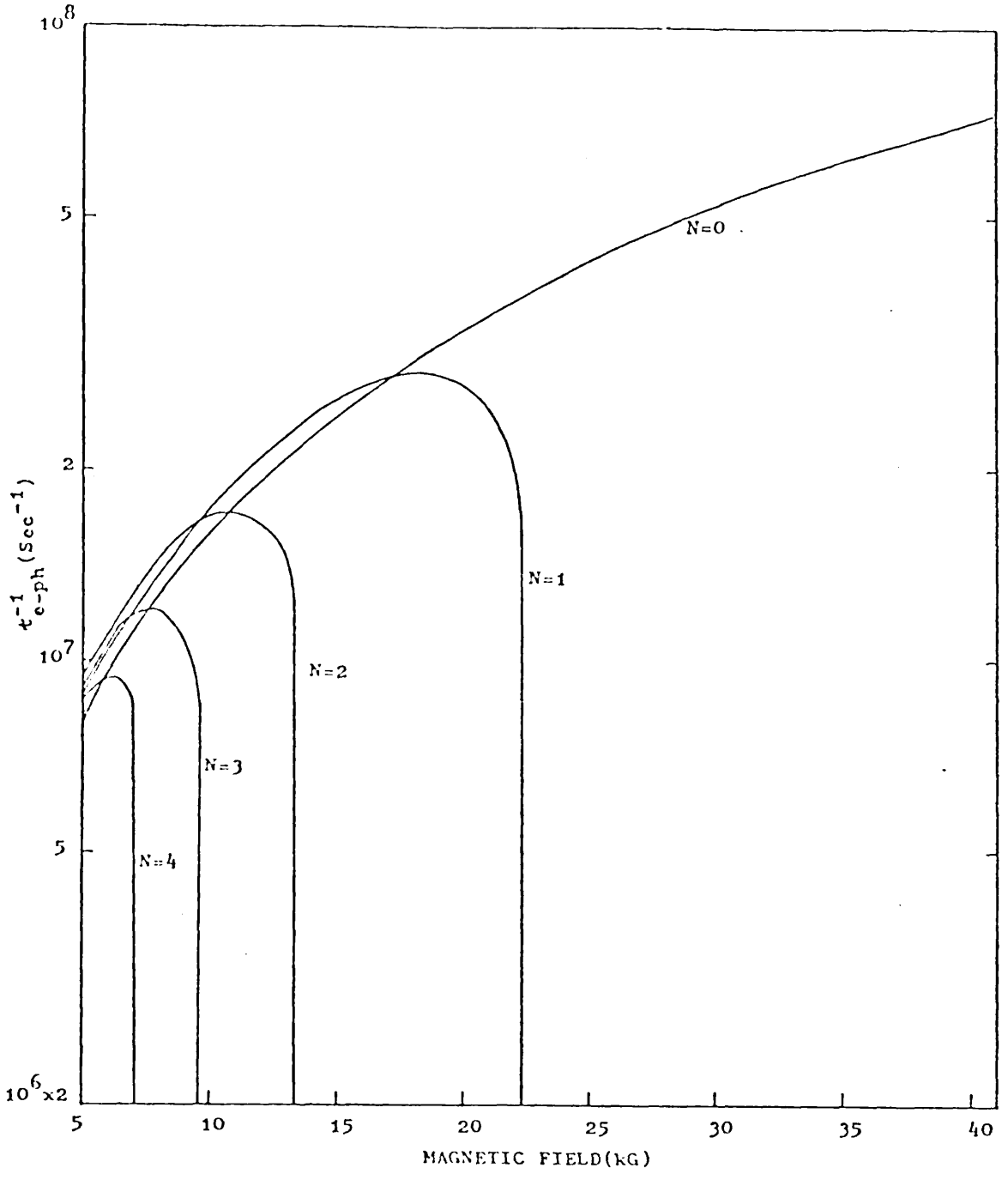

Figure 39. Magnetic field dependence of electron-phonon scattering relaxation rate for each Landau-level of sample D at 1.3 K.

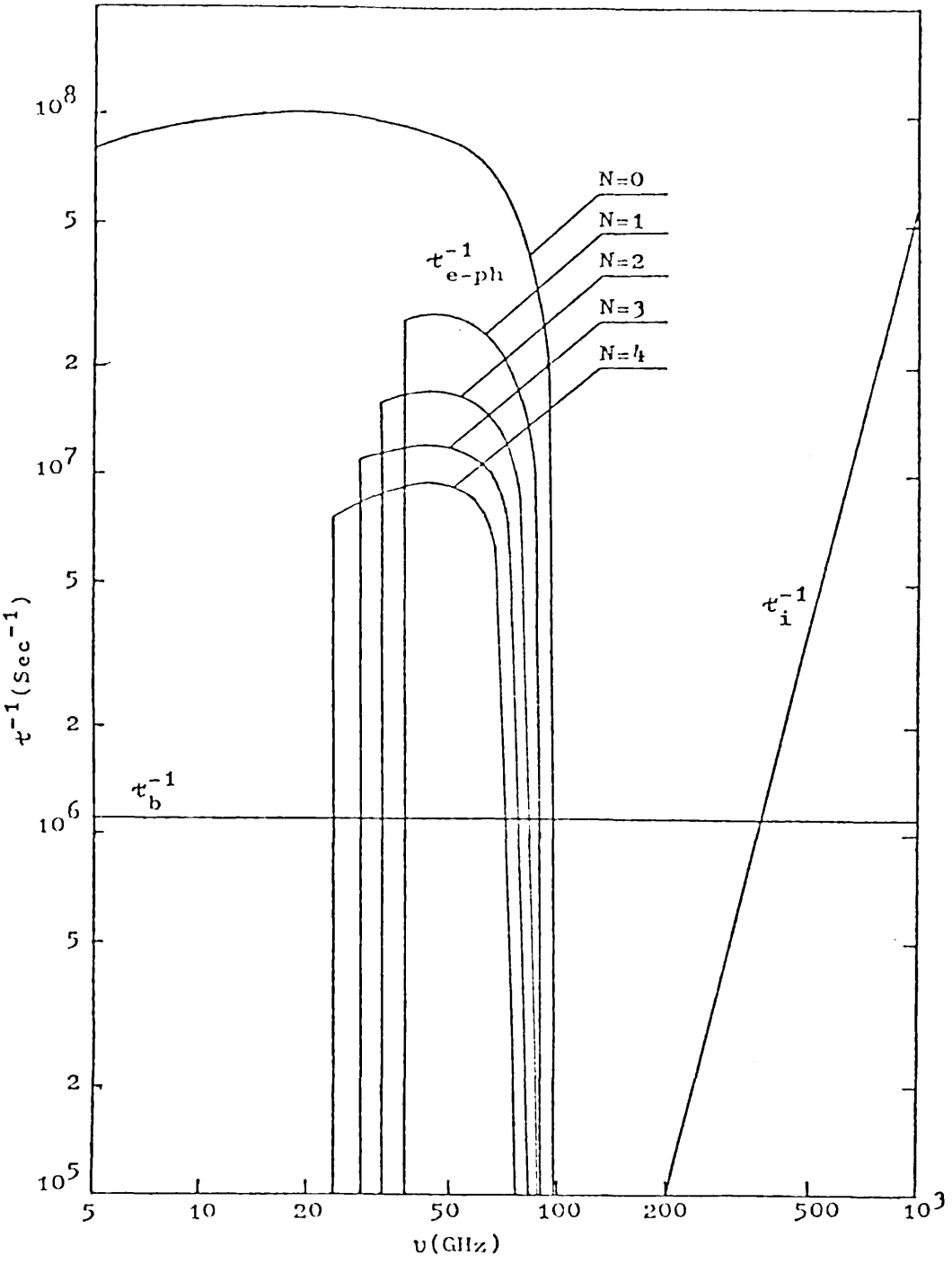

Figure 40. Frequency dependence of relaxation rate for boundary, isotope and electron scattering of phonons for each Landau-level of sample D at 1.3 K.

the Landau level involved with phonon scattering is deeper. Thus the best way to observe the oscillation of thermal conductivity is to maintain the ambient temperature of the sample in a range that the most probable phonons have a frequency where τ_{e-ph}^{-1} is effective. This temperature for sample D was 0.70K which was not attainable by the system used. However the oscillation could be observed up to 2K because of the broad thermal spectrum. But when the temperature increased the amplitude of the oscillation decreased because the most probable phonons moved to higher frequency.

Finally the effect of equation (5.25) was examined by adding it to the total relaxation time of the thermal conductivity integral, which was split into different parts according to q_1^n and q_2^n for each magnetic field as in the following

$$K(T) = \frac{k}{6\pi^2}(kT/\hbar)^3 \sum_{t=1}^{3} \frac{1}{v_t} \int_0^{q_1^1} \frac{e^x x^4 dx}{(\tau_b^{-1} + \tau_I^{-1})(e^x - 1)^2} +$$

$$\int_{q_1^1}^{q_2^1} \frac{x^4 e^x dx}{(\tau_b^{-1} + \tau_I^{-1} + \tau_{e-ph}^{-1})(e^x - 1)^2} + \int_{q_2^1}^{q_1^2} \frac{x^4 e^x dx}{(\tau_b^{-1} + \tau_I^{-1})(e^x - 1)^2} +$$

$$\int_{q_1^2}^{q_2^2} \frac{x^4 e^x dx}{(\tau_b^{-1} + \tau_I^{-1} + \tau_{e-ph}^{-1})(e^x - 1)^2} + \cdots\cdots$$

Figure (41) shows the calculated thermal conductivity for sample D versus magnetic field.

The calculated value has been deduced assuming only one Landau-level at a time is responsible for the electron-phonon scattering. This is justified by the condition 5-38. A comparison of figure(41)with the experimental results shown in figure(33) shows that there is good agreement between the period and amplitude of the oscillations. The shape of the oscillations however, are not the same and this may be due to various factors. For example the density of states in a magnetic field is ideally as:

$$\frac{dN}{d\varepsilon} = \left(\frac{2m^*}{\hbar^2}\right)^{\frac{1}{2}} \frac{1}{(2\pi\lambda)^2} \sum_{n,s} \left[\varepsilon - (n+\tfrac{1}{2}\pm\tfrac{1}{2}\gamma s)\hbar\omega_c\right]^{-\frac{1}{2}}$$

The singularities given by this formula when the Fermi level passes through each Landau-level are broadened by the presence of an impurity band which merges with conduction band . The absorption of phonons by electrons in this impurity band has been neglected due to lack of information about the impurity band.

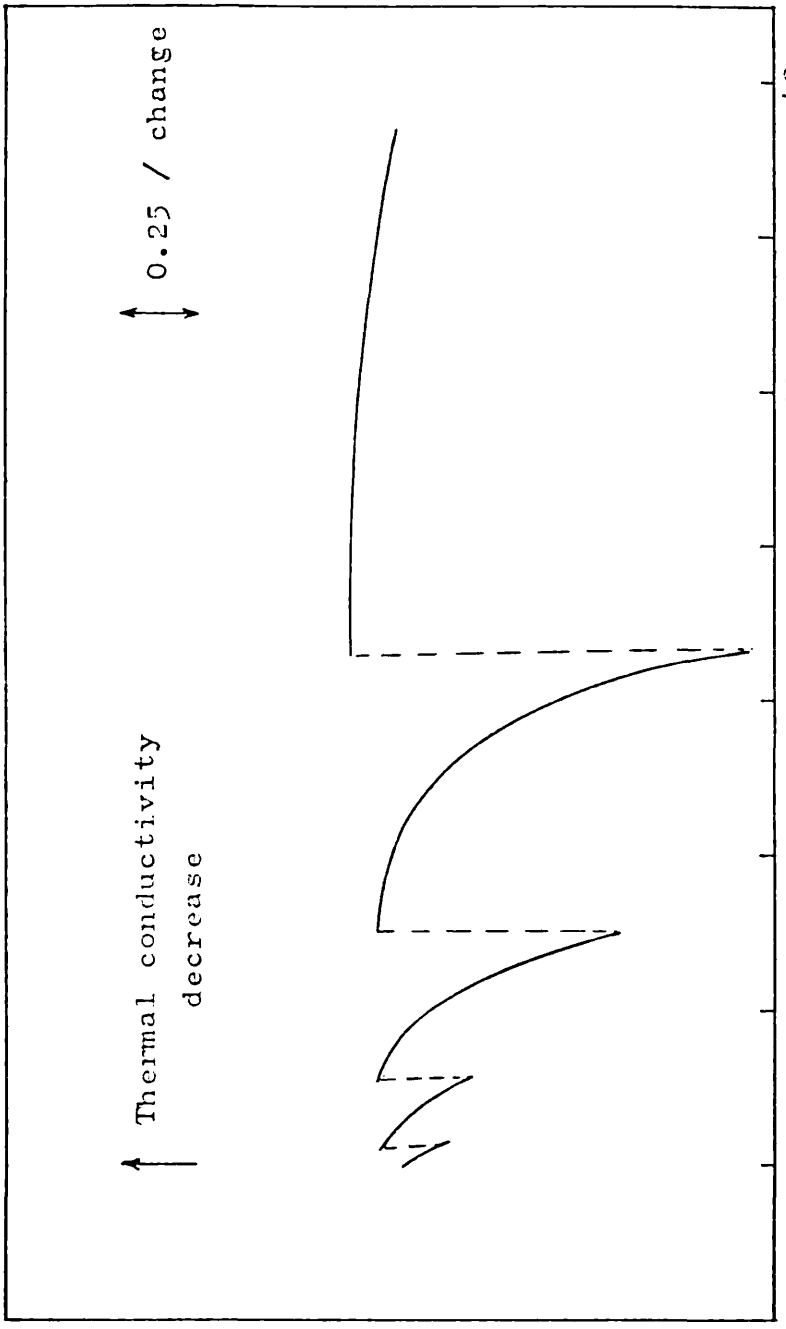

Figure 41. Calculated thermal conductivity for sample D.

CHAPTER 6

The Thermal Conductivity of p-InSb in Magnetic Field

6.1 Introduction

Measurements of the magnetothermal conductivity of two Ge doped p-type indium antimonide specimen have been made in the temperature range 1.2 to3K and in magnetic fields up to 40 kG.

As mentioned before the acceptor ground state in p-InSb is similar to that of Si or Ge which is four fold degenerate, and splits into the two Kramers doublets.

The effect of the magnetic field on the acceptor ground state is to split it into four single states. Since the first excited state is far above the ground state, the thermal phonons in the heat current can only be scattered through transitions within the quartet. When the degeneracy of the ground state is removed by a magnetic field, the conductivity should first fall as the level splittings become comparable to the dominant phonon energies (3.8kT) and then rise rapidly when the splittings become $\gg$ kT. The thermal conductivity of sample F (with acceptor concentration 2.8×10^{15} cm^{-3}) in a magnetic field decreased with increase of the magnetic field up to 38 kG and then approached a minimum at 40 kG. Since this was the highest field attainable the expected rapid rise of thermal conductivity could not be obtained. The observed magnetic field dependence of the conduction is considered to be due to the linear Zeeman effect. This will be discussed in detail in future sections.

6.2 Acceptor Ground States

The wave functions for shallow acceptor states have been briefly explained in section 4. Here they will be treated in more detail. The spin-orbit interaction splits the valence-band edge into a quartet and a doublet corresponding to the total angular momentum $J = \frac{3}{2}$ and $\frac{1}{2}$ states, respectively. The envelopes $F(\bar{r})$ in the wave functions 4.11 can be obtained by expanding in spherical harmonics $Y_{Lm}(\theta, \phi)$[51,52], and only odd L or only even L terms contribute simultaneously since the effective mass Hamiltonian is even under inversion[53], so:

$$F(r) = \sum_{L,m} f^{j}_{Lm}(r)\ Y_{Lm}(\theta, \phi) \qquad (6.1)$$

The acceptor ground state wave functions are largely s-like and in this case the even angular momentum expansion should be used (i.e. L = 0 and L = 2) for s and d-like parts. It is clear from equation (6.1) that if the sum is truncated after L = 2 there are six independent envelopes, one s-like for L = 0 and m = 0, and five d-like corresponding to L = 2 and m = 2, 1, 0, -1, -2. The wave functions of the acceptor ground state quartet ($J = \frac{3}{2}$) corresponding to the magnetic quantum numbers $M_J = \frac{3}{2}, \frac{1}{2}, -\frac{1}{2}, -\frac{3}{2}$ are of particular interest. These can be constructed from products of the s and d-like envelopes and the bases $\phi_j(r)$ in (4.11). For each M_J these products can be arranged to form six independent functions, ϕ_i, each of them satisfies the correct symmetry (Γ_8) of the $J=\frac{3}{2}$ states. Suzuki et al[44] have derived these functions for the axis of quantization along $[001]$ in the bases of (M_L, M_J) for Ge and Si. The

corresponding functions for the axis of quantization along [111] have been derived by Fjeldly et al[55] and are given in table III.

The radial parts are given by

$$R_o(r) = (4/r_1^3)^{\frac{1}{2}} \exp(-r/r_1) \qquad \text{s-like}$$

$$R_1(r) = (8/45r_2^7)^{\frac{1}{2}} r^2 \exp(-r/r_2) \qquad \text{d-like}$$

where r_1 and r_2 are the effective Bohr radii. Then the wave functions of the acceptor ground state can be written in the form

$$\psi = \sum_{i=0}^{5} c_i \phi_i^{M_J}$$

where the c_i's are the amplitude factors. Challis et al[56] have calculated approximate wave functions of acceptor states in the [110] direction.

However, a completely different approach for calculating the shallow acceptor states in semiconductors have been made by Baldereschi et al[57]. In the model used by Baldereschi the strong similarity between impurity centres and atomic and nuclear systems is used. In fact, the impurity centre is described as a particle with effective mass, spin and charge which is bound to the impurity site through a screened Coulomb potential. The acceptor Hamiltonian in the spin-orbit coupling limit, as written by Luttinger[59], is

$$H = (\gamma_1 + \tfrac{5}{2}\gamma_2)\frac{p^2}{2m_o} - \frac{\gamma_o}{m_o}(p_x^2 J_x^2 + p_y^2 J_y^2 + p_z^2 J_z^2) -$$

TABLE III

The functions $\phi_i^{M_J}$ for axis of quantization along $[111]$, with corresponding radial functions

M_J	3/2	1/2	-1/2	-3/2	Radial Parts
$\phi_0^{M_J}$	1	0	0	0	$\sqrt{\frac{1}{4\pi}}\,R_o(r)$
	0	1	0	0	
	0	0	0	0	
	0	0	0	0	
	0	0	1	0	
	0	0	0	1	
$\phi_1^{M_J}$	0	$a^*/2\sqrt{2}$	$-ia/4$	0	$\sqrt{\frac{5}{4\pi}}\,\frac{R_1(r)}{r^2}$
	$\sqrt{3}a/4$	0	$-a/4$	0	
	$i\sqrt{3}a^*/4$	$-a/2\sqrt{2}$	0	0	
	0	0	$a^*/2\sqrt{2}$	$-i\sqrt{3}a/4$	
	0	$a^*/4$	0	$\sqrt{3}a^*/4$	
	0	$ia^*/4$	$-a/2\sqrt{2}$	0	
$\phi_2^{M_J}$	$ib/\sqrt{6}$	$c^*/3$	$i\sqrt{2}c/3$	0	$\sqrt{\frac{5}{4\pi}}\,\frac{R_2(r)}{r^2}$
	$c/\sqrt{6}$	$-2b/3$	$-c^*/3\sqrt{2}$	0	
	$-i\sqrt{2/3}c^*$	$-c/3$	$-b^*/3\sqrt{2}$	0	
	0	$b/3\sqrt{2}$	$c^*/3$	$i\sqrt{2/3}c$	
	0	$c/3\sqrt{2}$	$2b^*/3$	$-c^*/\sqrt{6}$	
	0	$-i\sqrt{2}c^*/3$	$-c/3$	$-ib^*/\sqrt{6}$	
$\phi_3^{M_J}$	0	$-a^*/2\sqrt{2}$	$ia/4$	0	$\sqrt{\frac{5}{4\pi}}\,\frac{R_3(r)}{r^2}$
	$-a/4\sqrt{3}$	0	$a^*/4$	$ia/\sqrt{6}$	
	$ia^*/4\sqrt{3}$	$-a/2\sqrt{2}$	0	$a^*/\sqrt{6}$	
	$-a/\sqrt{6}$	0	$a^*/2\sqrt{2}$	$-ia/4\sqrt{3}$	
	$-ia^*/\sqrt{6}$	$a/4$	0	$a^*/4\sqrt{3}$	
	0	$-ia^*/4$	$a/2\sqrt{2}$	0	
$\phi_4^{M_J}$	$-b/\sqrt{6}$	$-c^*/3$	$-i\sqrt{2}c/3$	0	$\sqrt{\frac{5}{4\pi}}\,\frac{R_4(r)}{r^2}$
	$-c/3\sqrt{6}$	0	$-c^*/3\sqrt{2}$	$-4ic/3\sqrt{3}$	
	$-i\sqrt{\frac{5}{3}}c^*/3$	$-c/3$	$-b^*/\sqrt{2}$	$2c^*/3\sqrt{3}$	
	$-2c/3\sqrt{3}$	$b/\sqrt{2}$	$c^*/3$	$i\sqrt{2/3}c/3$	
	$4ic^*/3\sqrt{3}$	$c/3\sqrt{2}$	0	$c^*/3\sqrt{6}$	
	0	$i\sqrt{2}c^*/3$	$c/3$	$b^*/\sqrt{6}$	
$\phi_5^{M_J}$	0	$-\sqrt{2}c^*/3$	$ic/3$	$-i\sqrt{2/3}b^*$	$\sqrt{\frac{5}{4\pi}}\,\frac{R_5(r)}{r^2}$
	$2c/3\sqrt{3}$	0	$2c^*/3$	$-i\sqrt{\frac{5}{3}}c/3$	
	$ic^*/3\sqrt{3}$	$-\sqrt{2}c/3$	0	$-\sqrt{\frac{5}{3}}c^*/3$	
	$\sqrt{2/3}c/3$	0	$\sqrt{2}c^*/3$	$-ic/3\sqrt{3}$	
	$i\sqrt{\frac{5}{3}}c^*/3$	$-2c/3$	0	$-2c^*/3\sqrt{3}$	
	$i\sqrt{2/3}b$	$-ic^*/3$	$\sqrt{2}c/3$	0	

$$a = x^2 - y^2 - (2i/\sqrt{3})\left[z^2 - (x^2 + y^2)/2\right],\quad b = xy + yz + zx$$

$$\text{and } c = i\left[xy - (x + y)/2\right] + 3z(x - y)/2$$

$$\frac{2\gamma_3}{m_o}\left(\left[P_xP_y\right]\left[J_xJ_y\right] + \left[P_yP_z\right]\left[J_yJ_z\right] + \left[P_zP_x\right]\left[J_zJ_x\right]\right) - \frac{e^2}{\varepsilon_o r} \quad (6.2)$$

when terms linear in $\overline{P}$ are neglected for zinc-blend crystals. Here $\left[ab\right] = (ab + ba)/2$, m_o is the free electron mass, ε_o is the dielectric constant, $\overline{J}$ is the angular momentum operator for a particle with spin $\frac{3}{2}$ and $\overline{P}$ is the hole linear momentum operator. The Hamiltonian (6.2) describes a particle with spin $\frac{3}{2}$ in a Coulomb potential. It is convenient to write (6.2) in such a way that besides having cubic symmetry, it is also spherically invariant[60].

$$H = \left[\frac{\gamma_1}{2m_o}p^2 - \frac{e^2}{\varepsilon_o r}\right] - \frac{3\gamma_3+2\gamma_2}{45m_o}\left(P_q^{(2)}\cdot J_q^{(2)}\right) - \frac{\gamma_3-\gamma_2}{18m_o}\left(\left[P_q^{(2)}xJ_q^{(2)}\right]_{-4}^{4} + \sqrt{\frac{70}{15}}\left[P_q^{(2)}xJ_q^{(2)}\right]_0^4 + \left[P_q^{(2)}xJ_q^{(2)}\right]_4^4\right) \quad (6.3)$$

where the tensor operators $P_q^{(2)}$ and $J_q^{(2)}$ are second rank irreducible components with $q = -2, -1, 0, 1, 2$. Hence a new set of parameters for the description of the acceptor Hamiltonian is described together with γ_1 as:

$$\mu = (6\gamma_3 + 4\gamma_2)/5\gamma_1$$

which gives the strength of the spherical spin-orbit interaction, and

$$\delta = (\gamma_3 - \gamma_2)/\gamma_1$$

which measures the cubic contribution.

In indium antimonide $\varepsilon = 17.9$, $\gamma_1 = 35.08$, $\gamma_2 = 15.64$ and $\gamma_3 = 16.91$[61,62]. Finally Raymond[58] by considering the inversion asymmetry contribution to shallow acceptor

states in InSb presented the wave function ψ_α as

$$\psi_\alpha = \sum_{Lm} f_{Lm}[\alpha, Lm] \tag{6.4}$$

where α, Lm are basis function of the $\overset{Lm}{\alpha}$ representation which is computed from Y_L^m. The function f^α_{Lm} are

$$f^\alpha_{Lm} = \exp(-r/a_{Lm})P_{Lm}(r) \tag{6.5}$$

where P_{Lm} is a polynomial in r.

6.3 The Strain Hamiltonian

From symmetry consideration Hasegawa[45] constructed a strain Hamiltonian for the six state valence band edge in terms of the angular operator $\overline{L}$.

$$H^v_{strain} = D^v_d(e_{xx}+e_{yy}+e_{zz}) + 2D_u\left[L_x^2 - \tfrac{1}{3}L^2)e_{xx} + C.P.\right] + D_{u'}\left[(L_xL_y+L_yL_z)\cdot e_{xy} + C.P.\right] \tag{6.6}$$

where D^v_d, D_u and $D_{u'}$ are the valence band deformation potential constants. L_α is the α-component of the angular momentum operator (α = x,y and z). C.P. denotes cyclic permutation of the indices x,y and z. $e_{\alpha\beta}$ are the strain components defined as

$$e_{\alpha\beta} = \begin{cases} \partial U_\alpha/\partial x_\beta + \partial U_\beta/\partial x_\alpha & \text{for } \alpha \neq \beta \\ \partial U_\alpha/\partial x_\beta & \text{for } \alpha = \beta \end{cases} \tag{6.7}$$

where U_α is the α component of the displacement vector. The first term in Eq. (6.6) gives the shift of the centre of gravity of the valence band edge and since it does not contribute to the splitting, it is disregarded. The strain hamiltonian 6.6 can be used to find the energy split in

the acceptor ground state quartet, and also describes the oscillating strain due to the phonons and the resulting acceptor hole-lattice interaction. These effects requires the calculation of matrix elements of H^{v}_{strain} using the wave functions in the (M_L, M_s) bases. This can be carried out by representing the strain Hamiltonian by a 6 x 6 matrix on the same bases. Since there are no spin operators in H^{v}_{strain}, it can be written in the block form as:

$$H^{v}_{strain} = \begin{bmatrix} H^{v}_{strain}\,(3 \times 3) & 0 \\ 0 & H^{v}_{strain}\,(3 \times 3) \end{bmatrix} \tag{6.8}$$

with the 3 x 3 blocks defined by the L_α representation. $\alpha = 1, 2, 3$ are the three axes of a right handed cartesian coordinate system, with the axis of quantization along $\alpha = 3$.

$$L_1 = \frac{1}{\sqrt{2}}\begin{bmatrix} 0 & 1 & 0 \\ 1 & 0 & 1 \\ 0 & 1 & 0 \end{bmatrix} \qquad L_2 = \frac{1}{\sqrt{2}}\begin{bmatrix} 0 & -i & 0 \\ i & 0 & -i \\ 0 & i & 0 \end{bmatrix}$$

$$L_3 = \begin{bmatrix} 1 & 0 & 0 \\ 0 & 0 & 0 \\ 0 & 0 & -1 \end{bmatrix} \qquad L^2 = \begin{bmatrix} 2 & 0 & 0 \\ 0 & 2 & 0 \\ 0 & 0 & 2 \end{bmatrix} \tag{6.9}$$

For $[001]$ L_α, $\alpha = 1, 2, 3$ are simply the three components L_x, L_y and L_z of Eq. (6.6) respectively. In the case of z'-axis in the $[110]$ direction the choice of perpendicular

axes, x' and y' is immaterial, but a convenient set of direction is $[1\bar{1}0]$ for x' and $00\bar{1}$ for y'. L_x, L_y and L_z in (6.6) should be decomposed along the new coordinate axes, according to

$$L_x = \frac{1}{\sqrt{2}} (L_{x'} + L_{z'})$$

$$L_y = \frac{1}{\sqrt{2}} (-L_{x'} + L_{z'}) \qquad (6.10)$$

$$L_z = -L_{y'}$$

Strain Hamiltonian (6.6) can be written in terms of $\bar{J}$-operators acting only on the four Bloch states defined by $J = \frac{3}{2}$. This form is obtained by projecting H^v_{strain} into J space, while simultaneously relegating all information about the d-like parts of the envelopes to a set of deformation potential parameters D^a_u and $D^a_{u'}$, respectively in Eq. (6.6) (superscript "a" stands for acceptor). Thus only the s-like part of the wave functions are considered explicitly, and the projected portion of the Hamiltonian is written as:

$$H^a_{strain} = \tfrac{2}{3}D^a_u \left[(J_x^2 - \tfrac{1}{3}J^2)e_{xx} + C.P.\right] + \tfrac{1}{3}D^a_{u'} \left[(J_xJ_y + J_yJ_x)e_{xy} + C.P.\right] \qquad (6.11)$$

For oscillating strain like those produced by phonons the deformation potential parameters D^a_u and $D^a_{u'}$ are in general frequency dependent[54]. But these parameters are normally referred to as the deformation potential constants for the acceptor ground state. The connection between the static

D_u^a and $D_{u'}^a$, and the band edge deformation potential constants D_u and $D_{u'}$, can be obtained by comparing the matrix elements of H^a_{strain} (Eq. (6.11)) and H^v_{strain} (Eq. (6.6)) in the static strain limit. Hamiltonian (6.11) can be expanded in terms of the normal phonon modes. But first the displacement vectors $\bar{U}$ of Eq. (6.7) have to be expanded in terms of the vibrational modes of the crystal then the strain components would be substituted in the strain Hamiltonian. A standard procedure[33] leads to

$$U_\alpha = \sum_{\bar{q}t} \left[\frac{\hbar}{2M\omega_{\bar{q}t}}\right]^{\frac{1}{2}} \left[e^{\alpha}_{\bar{q}t}\ e^{i\bar{q}\cdot\bar{r}}\ a_{\bar{q}t} + C.C.\right] \qquad (6.12)$$

where $e^{\alpha}_{\bar{q}t}$ is the α-component of the polarization vector, $\omega_{\bar{q}t}$, the angular frequency, $a^{\dagger}_{\bar{q}t}$ the creation operator and $a_{\bar{q}t}$ the annihilation operator, and all are for accoustical phonons of branch t with wave vector $\bar{q}$. C.C means complex conjugate and M is the mass of the crystal. Using (6.12) and (6.7) the strain components can be easily derived as:

$$e_{\alpha\alpha} = \left[\frac{\hbar}{2M\omega_{\bar{q}t}}\right]^{\frac{1}{2}} \sum_{\bar{q}t} \left[i\ \bar{q}_\alpha\ e^{\alpha}_{\bar{q}t}\ e^{i\bar{q}\cdot\bar{r}}\ a_{\bar{q}t} + C.C.\right]$$

$$e_{\alpha\beta} = \left[\frac{\hbar}{2M\omega_{\bar{q}t}}\right]^{\frac{1}{2}} \sum_{\bar{q}t} \left[i(\bar{q}_\alpha\ e^{\beta}_{\bar{q}t} + \bar{q}_\beta\ e^{\alpha}_{\bar{q}t})e^{i\bar{q}\cdot\bar{r}}\ a_{\bar{q}t} + C.C.\right] \alpha \neq \beta \qquad (6.13)$$

In expression (6.13) it is assumed that the linear long wavelength limit of the phonon dispersion is valid which is a good approximation for the thermal phonon-frequency range considered here. The strain acting on the impurity

site, will split the quartet into two Kramers doublets. The effect of the strain may be considered as a static perturbation potential acting within the ground state if the magnitude of the valence band edge splitting is small compared to the ionization energy of the acceptors. The expansion of (6.11) in the normal vibrational mode will be carried out in appendix 2.

6.4 Zeeman Effect of Acceptor Ground State

The Zeeman effect of the shallow acceptors in semiconductors has been investigated theoretically and experimentally[63,64,68]. Most of the work has been done on acceptor states in germanium and silicon. The theoretical work on this problem has been mostly devoted to perturbation calculation based on the effective-mass approximation to obtain explicit g-values and intensities of the Zeeman components of the optical spectra[65] using four-component wave functions of the Kohn-Schechter type[66,67], and considering only the linear Zeeman effect. However, a group-theoretical treatment based only on symmetry consideration has proved to be capable of explaining the experimental results. For calculating the relative intensities of the Zeeman components the procedure is based on the method developed by Rodrigues, Fisher and Barra[69] for stress-induced components.

The application of a magnetic field $\overline{B}$ introduces new terms in the Hamiltonian of the acceptor holes. These additional terms constitute the Zeeman Hamiltonian

$$H_{Zeeman} = -\mu_B(\overline{L} + 2\overline{s}).\overline{B} - \tfrac{1}{2}m\mu_B^2\left[r^2B^2-(\overline{r}.\ \overline{B})^2\right] \qquad (6.14)$$

where μ_B is the Bohr magneton, m the free electron mass, $\bar{r}$ the position operator of the holes, $\bar{L}$ and $\bar{s}$ are the orbital and the spin angular momenta in units of $\hbar$, respectively. The most general form of the Hamiltonian matrix for a Γ_8 level can be expressed in terms of the angular momentum operator $\bar{J}$ as

$$H_{Zeeman} = \mu_B g_1'(\bar{B}.\bar{J}) + \mu_B g_2'(B_x J_x^3 + B_y J_y^3 + B_z J_z^3) + q_1 B^2 + q_2(\bar{B}.\bar{J})^2 + q_3(B_x^2 J_x^2 + B_y^2 J_y^2 + B_z^2 J_z^2) \quad (6.15)$$

where the parameters g_1', g_2', q_1, q_2 and q_3 depend on the unperturbed wave functions of the acceptor ground state level. The angular momentum matrices are given in (A.1), and the components of $\bar{B}$ refers to the cubic axes x, y, and z of the crystal. Let the orientation of $\bar{B}$ be given by the polar angle β and the azimuthal angle α. That is, $\bar{B} = B\bar{n}$ with

$$\begin{aligned} n_x &= \sin\beta\cos\alpha, \\ n_y &= \sin\beta\sin\alpha \\ n_z &= \cos\beta \end{aligned} \quad (6.16)$$

Then the H_{Zeeman} becomes

$$H_{Zeeman} = \mu_B\left[g_1'(\bar{n}.\bar{J}) + g_2'(n_x J_x^3 + n_y J_y^3 + n_z J_z^3)\right]B + \left[q_1 + q_2(\bar{n}.\bar{J})^2 + q_3(n_x^2 J_x^2 + n_y^2 J_y^2 + n_z^2 J_z^2)\right] B^2 \quad (6.17)$$

For an arbitrary direction of the magnetic field, Eq. (6.17) is not necessarily diagonal in the $J = \frac{3}{2}$ space. The energies of the Zeeman sublevels can be obtained by

diagonalizing the Hamiltonian matrix (6.17). But the eigen functions are no longer defined by the states of $J = \frac{3}{2}$. When the magnetic field is applied in the $[110]$ direction, the Zeeman Hamiltonian in the transformed basis becomes

$$H'_{Zeeman} = \mu_B g'_2 B \left\{ PJ_z + (1/\sqrt{2})(J'^3_x + J'^3_y) + \left[\frac{q_1}{\mu g'_2} + \frac{q_2}{\mu_B g'_2} J_z^2 + \frac{q_3}{2\mu_B g'_2} \right.\right.$$

$$\left.\left. \times \left(\frac{15}{4} - J_z^2\right) \right] B \right\} \qquad (6.18)$$

By using transformation matrix (A.2) and proper unitary transformation to diagonalize the H'_{Zeeman} the energies of the Zeeman sublevels can be derived as[62]

$$E_{+\frac{3}{2}} = \mu_B g'_2 B \left\{ \Delta_+ + \left(\tfrac{1}{2}P + \tfrac{7}{8}\right) + \left[s_1 + \tfrac{3}{4}(s_2 + s_3) \right] B \right\}$$

$$E_{+\frac{1}{2}} = \mu_B g'_2 B \left\{ \Delta_- - \left(\tfrac{1}{2}P + \tfrac{7}{8}\right) + \left[s_1 + \tfrac{3}{4}(s_2 + s_3) \right] B \right\}$$

$$E_{-\frac{1}{2}} = \mu_B g'_2 B \left\{ -\Delta_+ + \left(\tfrac{1}{2}P + \tfrac{7}{8}\right) + \left[s_1 + \tfrac{3}{4}(s_2 + s_3) \right] B \right\} \qquad (6.19)$$

$$E_{-\frac{3}{2}} = \mu_B g'_2 B \left\{ -\Delta_- - \left(\tfrac{1}{2}P + \tfrac{7}{8}\right) + \left[s_1 + \tfrac{3}{4}(s_2 + s_3) \right] B \right\}$$

where $P = g'_1/g'_2$, $s_k = q_k/\mu_B g'_2$ and

$$\Delta_\pm = \left\{ \left[\left(P + \tfrac{7}{8} \right] \pm \left[s_2 + \tfrac{1}{4} s_3 \right] B \right)^2 + \frac{3}{64}(3 \pm 2 s_3 B)^2 \right\}^{\frac{1}{2}} \qquad (6.20)$$

The allowed transition between the levels $\frac{3}{2}$, $\frac{1}{2}$, $-\frac{1}{2}$ and $-\frac{3}{2}$ are numbered 1, 2, 3 and 4 respectively. Using (6.19)

these transition energies in the [110] direction are determined as

$$E_{12} = \mu_B g_2' B \left\{ \Delta_+ - \Delta_- + \left(\frac{g_1'}{g_2'} + \frac{7}{4} \right) \right\}$$

$$E_{13} = 2\mu_B g_2' \Delta_+ B$$

$$E_{24} = -2\mu_B g_2' \Delta_- B \qquad (6.21)$$

$$E_{34} = \mu_B g_2' B \left\{ -\Delta_- + \Delta_+ - \left(\frac{g_1'}{g_2'} + \frac{7}{4} \right) \right\}$$

The magnetic field dependence of the energy splitting $E_{nn'}$ can be calculated by using the resonance field and Eqns. (6.21) which include four parameters g_1', g_2', q_2 and q_3. However, if only linear Zeeman effect is considered here(i.e. $q_2 = q_3 = 0$) the number of parameters reduces to only g_1' and g_2'. According to the theory of the effective mass approximation the ground state of the shallow acceptors in the cubic semiconductors is split due to the initial local fields. The splittings are induced by the static fields which break the tetrahedral symmetry at the acceptor site. In the absence of the external fields, the splitting may be caused by the initial local stresses which are brought about by the randomly distributed crystal imperfections and the dislocations as well as weak correlations among the acceptor impurities[70]. This initial splitting should be considered in calculation of the energy levels.

6.5 Analysis of the Magnetothermal Conductivity of p-InSb

Results of the reduced thermal conductivity (K/K_o) of sample F ($N_A - N_D = 2.84 \times 10^{15}$ cm^{-3}) is presented in figure (42). As one expects the thermal conductivity decreases when the magnetic field is increased, and also when the temperature is raised the effect of the field on thermal conductivity diminishes. The average distance between the impurities for this sample ($d \simeq 8a^*$) satisfies the need to keep $d \gg a^*$ to avoid overlap between neighbouring acceptors so the impurities are considered to be isolated and the theory explained in sections 6.4 is applicable in this case. The g-factors g_1' and g_2' involved in equations (6.21) are not the conventional Zeeman g-factors $g_{\frac{3}{2}}$ and $g_{\frac{1}{2}}$ which are the splitting coefficients of the ground state energy levels. g_{M_J} is defined by:

$$E_{M_J} = M_J \; g_{|M_J|} \mu_B \; B \qquad (6.22)$$

Hence to find $g_{\frac{3}{2}}$ and $g_{\frac{1}{2}}$ in $[110]$ direction, equations (6.21) and (6.22) is used as in the following

$$E_{\frac{3}{2}} - E_{-\frac{3}{2}} = 3g_{\frac{3}{2}}\mu_B B = 2\mu_B g_2' B\left\{\Delta + \left(\frac{1}{2}\frac{g_1'}{g_2'} + \frac{7}{8}\right)\right\} \qquad (6.23)$$

where $\Delta = \Delta_- = \Delta_+$ or simply only the first order terms are taken into account. $g_{\frac{1}{2}}$ can be found in the same way as (6.23) and the simplified expressions are given as

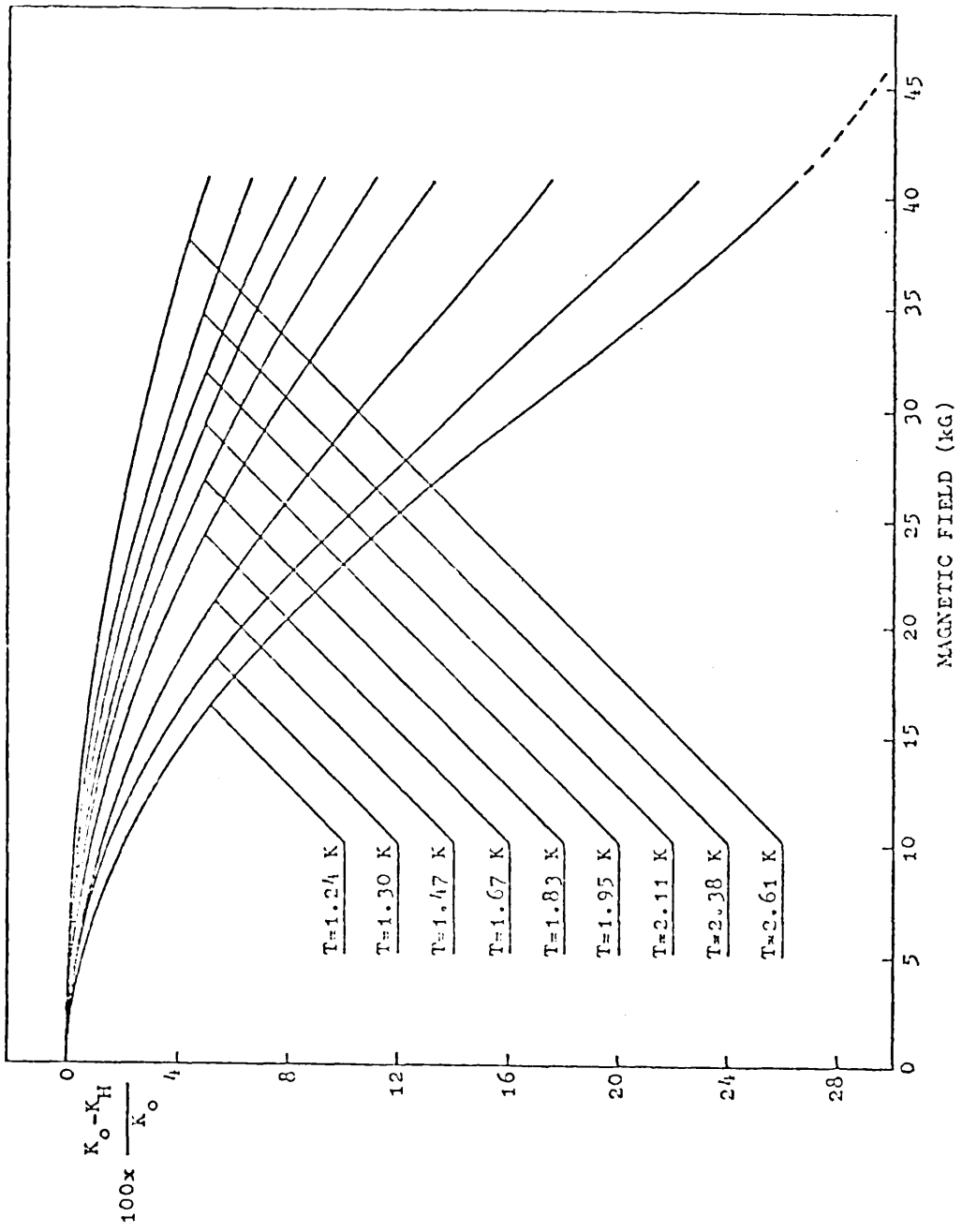

Figure 42. Magnetic field dependence of thermal conductivity of sample F with acceptor concentration $p=2.84\times10^{15}$ cm^{-3} at several temperatures.

$$g_{\frac{3}{2}} = \frac{3}{3}\left\{\left[\left(g_1' + \frac{17}{8}g_2'\right)^2 + \frac{27}{64}g_2'^{\,2}\right]^{\frac{1}{2}} + \left(\frac{1}{2}g_1' + \frac{7}{8}g_2'\right)\right\}$$

$$g_{\frac{1}{2}} = 2\left\{\left[\left(g_1' + \frac{17}{8}g_2'\right)^2 + \frac{27}{64}g_2'^{2}\right]^{\frac{1}{2}} - \left(\frac{1}{2}g_1' + \frac{7}{8}g_2'\right)\right\}$$

An estimation of these g-factors can be made by using approximate resonance field and also the energy of the dominant phonons (i.e. $\Delta E = \hbar\omega = 3.8kT$)[14,48]. As mentioned in section (6.1) a clear minimum of magnetothermal conductivity could not be obtained. However, from the data at the lowest temperature, the position of the minimum could be guessed and the following values are estimated

$$g_2' = 0.38 \qquad \text{and} \qquad g_1' = -0.1$$

and consequently

$$g_{\frac{1}{2}} = 0.93 \qquad \text{and} \qquad g_{\frac{3}{2}} = 0.69$$

The error can be as large as the estimated values. These g-values have been calculated by many authors for Ge and Si[65,44]. A variety of values is obtained according to the choice of the effective mass wave functions and the valence band parameters. But these values are in sharp contrast with the experimental results obtained by Challis et al[14] and Tokumoto[69]. However, direct experimental or theoretical determination of these g-factors for indium antimonide have not been made and the work on optical spectra and the analysis of these presumably would be exceedingly complicated anyway. Since there has not been a source of comparison for the g-factors for indium antimonide the choice of above values is questionable.

The results of sample G ($N_A - N_D = 2.4 \times 10^{17}$ cm^{-3})

is given in Fig. (43). Comparisn of the data obtained for sample F and G reveals that the effect of the magnetic field decreases when the carrier concentration is increased. This can be due to the overlap of the impurity band (IB) of sample G with the valence band (VB). The separation of the impurities in this sample ($d \simeq a^*$) which is a clear indication of the merging of IB with the VB, and so at low magnetic field the hole-phonon interaction is due to the free charge carriers. To check on this the magnetoresistance of this sample was measured (see Figure (44)) and the same behaviour as magnetothermal resistance was observed. So it is concluded that due to the high impurity concentration the hole-phonon interaction is screened due to the condition ($q_{TF} < q < 2k_F$) explained in section 4.1 for zero field thermal conductivity and since only this interaction is affected by the magnetic field the effect in sample G is less than that of sample F.

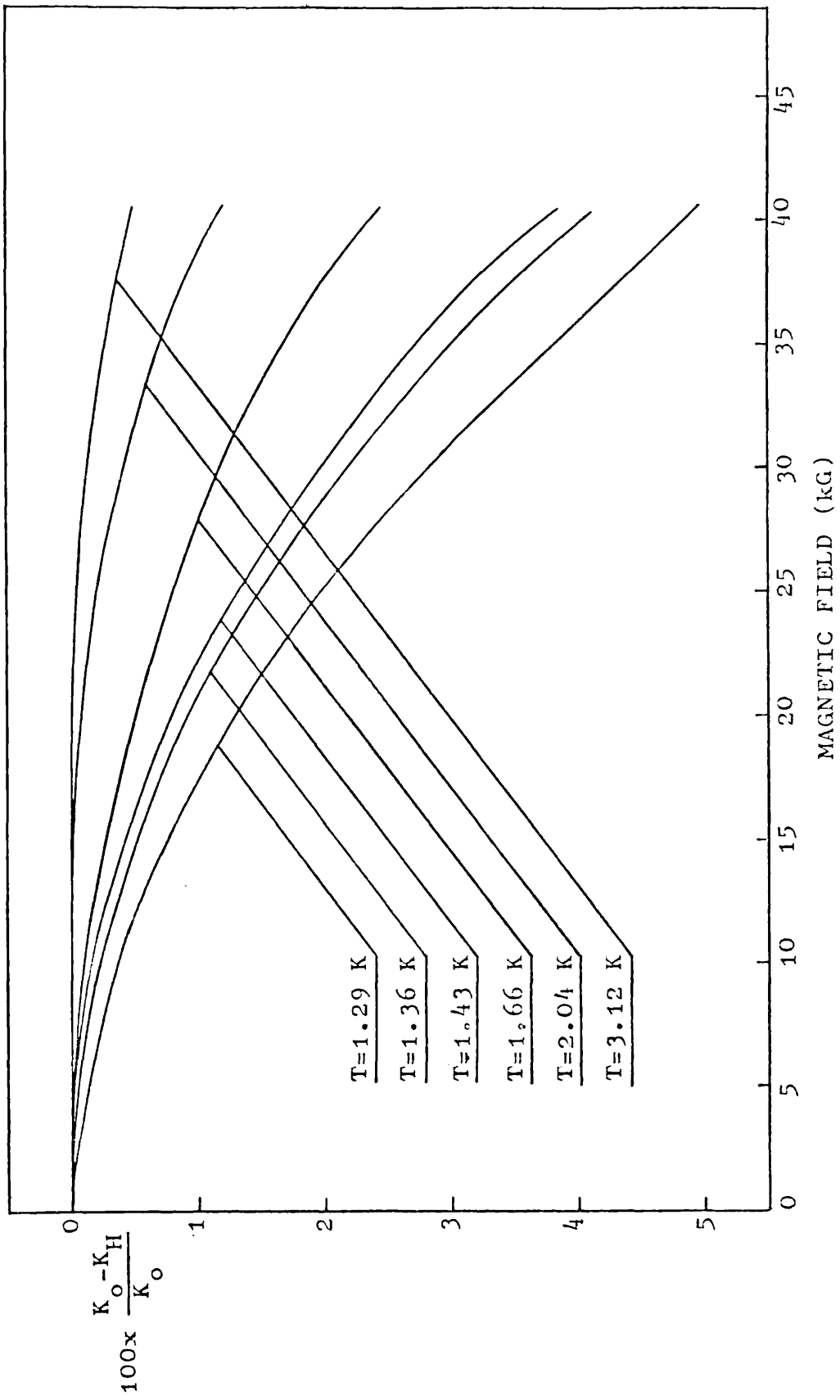

Figure 43. Magnetic field dependence of thermal conductivity of sample G with acceptor concentration $p=2.4\times10^{17}$ cm^{-3} at several temperatures.

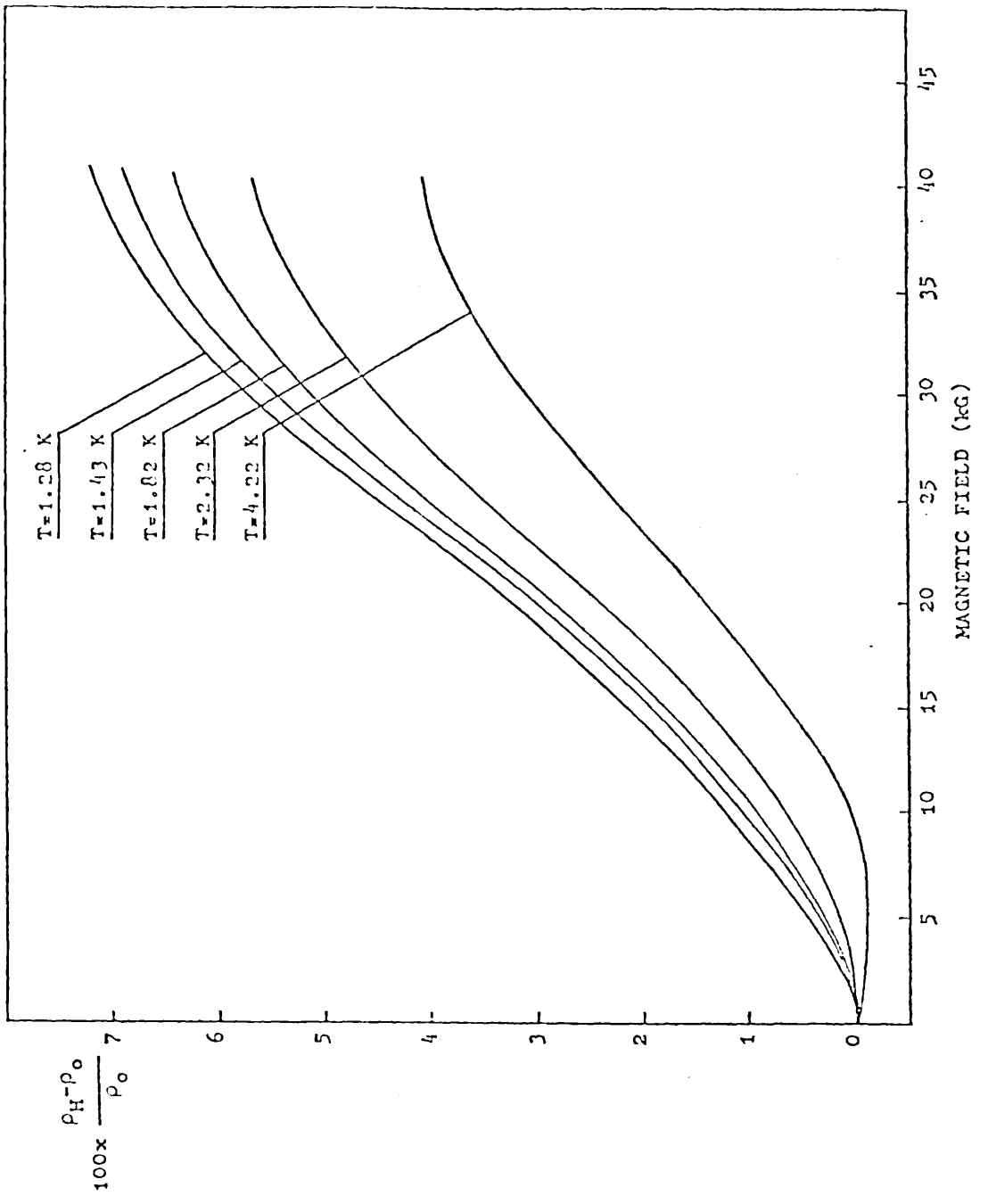

Figure 44.Longitudinal magnetoresistance of sample G with acceptor concentration $p=2.4\times10^{17}$ cm^{-3} at several temperatures.

Conclusion

It has been shown that despite some initial difficulties, the thermal conductivity measurements at liquid helium temperature could be performed automatically by means of a microprocessor based control system providing higher accuracy and quicker data collection than previously possible . The results obtained for both n and p-type indium antimonide single crystals using this system have been analysed by the standard theory of thermal conductivity,and agreed with previous measurements.

In measurements of the thermal conductivity of n-type indium antimonide in a magnetic field the quantum oscillation of the phonon absorption by electrons was explained qualitatively by an electron-phonon interaction Hamiltonian. This oscillation is ascribed to a narrow band of frequencies within the phonon spectrum which are highly absorbed by the electrons. The band is bounded by q_1 and q_2 such that both are less than q_{CR}. These frequencies are independent of temperature. However, the amplitude of thecscillations depend on the temperature being largest when q_1 and q_2 are near the maximum of the phonon spectrum. The oscillatory absorption is associated mainly by the intra Landau level transitions. The period is in close agreement with the de Haas - Shubnikov period. The calculated K determined without any adjustable parameter except those used to derive the zero field thermal conductivity has an oscillation amplitude comparable with

the measured oscillations, but the calculated curves have abrupt changes which are not present in the measured - oscillations. Exact correlation between theory given here and experiment can not be expectd because only one intra Landau level transition has been considered and the - likely distortion of the density of states by impurity level has been ignored. Spot calculation on inter Landau-leve transitions indicate such transitions probably have negligible effect, however the effect of impurity levels blurring the shape at botton of the Landau - level is not known, but may well be the cause of smoothing the oscillations.

The magnetothermal conductivity in p - InSb has been explained by the first order Zeeman splitting of the four fold degenerate acceptor states, similar to that of p-type silicon (i.e. an initial decrease in thermal conductivity with increase of the magnetic field and the exhibition of a broad minimum) . From an estimate of the position of the minimum of the thermal conductivity for InSb Zeeman g - factors have been estimated. The minimum appear to occur at a higher magnetic field than is observed in silicon because the g - factors for indium antimonide is less than that for silicon. An interesting observation is the effect of the magnetic field on thermal conductivity of more heavily doped sample was less than the effect observed in lightly doped sample . This is interpreted as the charge carrier system reacts as a plasma to low-

frquency phonon, and the resulting screening decreases the phonon - charge carrier interaction in more heavily doped samples. However, extension of the investigation in higher magnetic field for p - InSb would be interesting .

APPENDIX 1

The following programme has been developed to be loaded on Keithley- System one for automatic measurements of the thermal conductivity. The main feature of this programme according to the flowchart given in sec.3 is that the ambient temperature of the system is kept constant for the complete measurements of each parameter. All the calculations involved are carried out and then the required data such as temperature difference across the sample, heat gradient, ambient temperature and the thermal conductivity are printed.

DECIMAL STEP	INSTRUCTION CODE	INSTRUCTION MNEMONIC	COMMENTS
0000	066	IND/SYMB	Subroutine "CL"
1	063	CL	
2	271	LDDL xxx	Load DL
3	000	0	
4	272	LDDH xxx	Load DH
5	023		
6	372	STKD	Stack DC
7	371	RCLP	Recall P
8	371		
9	057		
0010	066	IND/SYMB	Subroutine to scan different channels
1	071	Sin^{-1}	
2	266	LDIX	
3	202		Choose slot 2
4	314	OPCB	Output Control Byte
5	266	LDIX	
6	121		C.C.1 normal
7	315	OPDB	Output Data Byte

DECIMAL STEP	INSTRUCTION CODE	INSTRUCTION MNEMONIC	COMMENTS
0013	266	LDIX	
9	202		
0020	314	OPCB	
1	266	LDIX	
2	125		C.C.2 normal
3	315	OPDB	
4	066	SYMB/IND	Symbolic address
5	055		
6	111	↑()	
7	012	.	
8	111	↑()	
9	021	+	
0030	004	4	
1	127	BR	Branch() () to subroutine A^X
2	067		
3	025	A^X	
4	120	↓()()	Store in pointer
5	067	IND/SYMB	
6	377	NOOP	
7	111	↑()	
8	012	.	
9	151		
0040	110	↓()	
1	012	.	
2	111	↑()	
3	022	-	

DECIMAL STEP	INSTRUCTION CODE	INSTRUCTION MNEMONIC	COMMENTS
0044	003	3	
5	022	-	
6	001	1	
7	020	=	
8	126	JU	Jump()() to
9	022	-	
0050	067	IND/SYMB	
1	055		
2	126	JU	Set Flag
3	016	FLAG	
4	067	IND/SYMB	
5	020	=	
6	001	1	
7	000	0	
8	110	↓()	
9	022	-	
0060	004	4	Choose channel
1	001	1	
2	000	0	
3	111	↑()	
4	021	+	
5	011	9	
6	110	↓()	Store in pointer
7	012	.	
8	001	1	
9	000	0	

DECIMAL STEP	INSTRUCTION CODE	INSTRUCTION MNEMONIC	COMMENTS
0070	110	↓()	
1	021	+	
2	003	3	
3	266	LDIX	Choose slot 2
4	202		
5	314	OPCB	Output Control Byte
6	266	LDIX	
7	122		Revers C.C.1
8	315	OPDB	Output Data Byte
9	266	LDIX	
0080	202		
1	314	OPCB	Output Control Byte
2	266	LDIX	
3	126		Revers C.C.2
4	315	OPDB	Output Data Byte
5	266	LDIX	
6	202		
7	314	OPCB	Output Control Byte
8	266	LDIX	
9	065		Revers sample
0090	315	OPDB	Heater current
1	016	FLAG	
2	004	4	Choose channel 3
3	001	1	
4	003	3	
5	105	OUT	
6	001	1	Choose mostsen-sitive range on DVM

DECIMAL STEP	INSTRUCTION CODE	INSTRUCTION MNEMONIC	COMMENTS
0097	003	3	
8	105	OUT	
9	003	3	
0100	107	WAIT	Wait for 3 sec.
1	126	JU	Jump()() to
2	067	IND/SYMB	
3	055		
4	066	IND/SYMB	
5	020	=	
6	166		Reset Flag
7	111	↑()	Store final channel in pointer
8	011	9	
9	110	↓()	
0110	012	.	
1	176		Print a dot line
2	066	IND/SYMB	Subroutine R^o for averaging measured value on each channel
3	072	R^o	
4	121	↑()()	
5	067	IND/SYMB	
6	110	↓()	
7	002	2	
8	001	1	
9	000	0	
0120	113	+	Add ten to pointer
1	012	.	
2	121	↑()()	

DECIMAL STEP	INSTRUCTION CODE	INSTRUCTION MNEMONIC	COMMENTS
0123	067	IND/SYMB	
4	013	-	
5	021	+	
6	111	↑( )	
7	002	2	
8	024	÷	Divide the sum by half
9	002	2	
0130	020	=	
1	120	↓( )( )	Store in main data register for printing
2	067	IND/SYMB	
3	060	PRINT	Print the average value
4	111	↑( )	
5	012	.	
6	111	↑( )	
7	022	-	
8	003	3	
9	126	JU	If all the scanned channels are averaged check for the next decision.
0140	020	=	
1	067	IND/SYMB	
2	047		
3	013	-	
4	011	9	Add nine to pointer
5	113	+	
6	012	.	
7	126	JU	If averaging is not finished continue

DECIMAL STEP	INSTRUCTION CODE	INSTRUCTION MNEMONIC	COMMENTS
0148	067	IND/SYMB	
9	072	R^{o}	
0150	066	IND/SYMB	
1	047		
2	176		Print a dot line
3	011	9	
4	111	↑( )	
5	021	+	
6	011	9	
7	110	↓( )	
8	012	.	
9	022	-	
0160	001	1	Check if the first channel scanned is 1 then go to sub. LG^{-1} to calculate the temperature
1	000	0	
2	02o	=	
3	126	JU	
4	020	=	
5	067	IND/SYMB	
6	051	LG^{-1}	
7	022	-	
8	002	2	
9	000	0	
0170	020	=	
1	126	JU	
2	020	=	
3	067	IND/SYMB	

DECIMAL STEP	INSTRUCTION CODE	INSTRUCTION MNEMONIC	COMMENTS
0174	051	LG^{-1}	
5	066	IND/SYMB	Subroutine to calculate the resistance of each thermometer
6	031		
7	127	BR	
8	067	IND/SYMB	
9	052	F	
0180	120	↓()()	Store R1 in the main data register no. 84
1	010	8	
2	004	4	
3	001	1	
4	177		Print identifier for thermometer 1
5	060	PRINT	
6	127	BR	
7	067	IND/SYMB	
8	052	F	
9	120	↓()()	Store R2 in the main data register no. 85
0190	010	8	
1	005	5	
2	002	2	
3	177		Print identifier for thermometer 2
4	060	PRINT	
5	010	8	
6	111	↑()	
7	022	-	
8	005	5	
9	126	JU	If calculation and print of the value for thermometer R1 and R2 get heater current

DECIMAL STEP	INSTRUCTION CODE	INSTRUCTION MNEMONIC	COMMENTS
0200	021	+	
1	067	IND/SYMB	
2	062	RESET	
3	121	↑()()	
4	001	1	
5	010	8	
6	023	X	Multiply
7	121	↑()()	Get heater voltage
8	001	1	
9	011	9	
0210	023	X	
1	014	EXP	
2	003	3	Calculate the heat current in sampler heater
3	020	=	
4	060	PRINT	
5	120	↓()()	Store in main data storage 86
6	010	8	
7	006	6	
8	066	IND/SYMB	
9	062	RESET	End of the subroutine scan
0220	057	RESUME	
1	066	IND/SYMB	Subroutine to choose channel and range
2	025	A^X	
3	105	OUT	
4	001	1	
5	003	3	
6	110	↓()	

DECIMAL STEP	INSTRUCTION CODE	INSTRUCTION MNEMONIC	COMMENTS
0227	006	6	
8	012	.	Choose most sensitive range on DVM
9	000	0	
0230	000	0	
1	003	3	
2	110	↓( )	
3	010	8	
4	066	IND/SYMB	
5	070	SIN	
6	111	↑( )	
7	006	6	
8	105	OUT	
9	002	2	Wait 2 sec.
0240	107	WAIT	
1	001	1	Read the voltage from the DVM
2	106	READ	
3	110	↓( )	
4	007	7	
5	111	↑( )	
6	010	8	
7	022	-	
8	111	↑( )	Check on the range
9	007	7	
0250	045	X	
1	020	=	If over ranging go to change range

DECIMAL STEP	INSTRUCTION CODE	INSTRUCTION MNEMONIC	COMMENTS
0252	126	JU	
3	022	-	
4	067	IND/SYMB	
5	050	LG	
6	004	4	
7	107	OUT	
8	001	1	Read the final value on DVM
9	106	READ	
0260	057	RESUME	Go back to branch point
1	066	IND/SYMB	
2	050	LG	
3	001	1	Add 1 to scratch pad 6
4	113	+	
5	006	6	
6	001	1	Increment the range
7	000	0	
8	110	↓( )	
9	023	X	
0270	010	8	
1	126	JU	End of subroutine range and channel
2	067	IND/SYMB	
3	070	SIN	
4	066	IND/SYMB	Subroutine 2FUN to calculate the resistance
5	052	F	
6	001	1	

DECIMAL STEP	INSTRUCTION CODE	INSTRUCTION MNEMONIC	COMMENTS
0277	113	+	
8	012	.	
9	121	↑()()	Get the voltage
0280	067	IND/SYMB	
1	110	↓()	
2	002	2	
3	001	1	
4	113	+	
5	012	.	
6	121	↑()()	Get the current
7	067	IND/SYMB	
8	024	÷	
9	111	↑()	
0290	002	2	
1	023	X	
2	014	EXP	
3	003	3	
4	020	=	End of the sub-routine 2FUN
5	057	RESUME	
6	066	IND/SYMB	Subroutine to calculate the temperature
7	022	-	
8	050	LG	Calculate ln R3
9	110	↓()	
0300	006	6	
1	121	↑()()	Get coeficients A_i
2	067	IND/SYMB	
3	110	↓()	

DECIMAL STEP	INSTRUCTION CODE	INSTRUCTION MNEMONIC	COMMENTS
0304	001	1	
5	066	IND/SYMB	Get the loop to calculate sum
6	117	DE.SET	
7	111	↑( )	
8	001	1	
9	111	↑( )	Get $(\ln R)^i * A_i$
0310	023	X	
1	006	6	
2	110	↓( )	
3	010	8	
4	111	↑( )	
5	012	.	Decrease pointer by 1
6	152		
7	110	↓( )	
8	012	.	
9	121	↑( )( )	Calculate $A_i(\ln R)^1 + A_{i-1}$ in the loop
0320	067	IND/SYMB	
1	111	↑( )	
2	021	+	
3	010	8	
4	110	↓( )	
5	001	1	
6	111	↑( )	Subtract 2 from pointer
7	012	.	
8	111	↑( )	
9	022	-	

DECIMAL STEP	INSTRUCTION CODE	INSTRUCTION MNEMONIC	COMMENTS
0330	002	2	
1	126	JU	
2	021	+	
3	067	IND/SYMB	
4	117	DE.SET	
5	111	↑()	Get ln T
6	001	1	
7	051	e^x	Calculate T
8	057	RESUME	Go to branch point

Step 0342 to 0509 the output handler for interface model 7801 - 1722 is stored (See Kiethley instruction manual).

0510	066	IND/SYMB	Subroutine e^x to calculate R3 and subsequently the temperature
1	051	e^x	
2	003	3	
3	177		
4	127	BR	Branch to subroutine 2FUN
5	067	IND/SYMB	
6	052	F	
7	352	ICEX	
8	060	PRINT	Print R3 in ohms
9	110	↓()	
0520	003	3	
1	004	4	
2	000	0	
3	110	↓()	
4	002	2	

DECIMAL STEP	INSTRUCTION CODE	INSTRUCTION MNEMONIC	COMMENTS
0525	004	4	
6	010	8	
7	110	↓( )	
8	012	.	
9	176		Print a dot line
0730	111	↑( )	
1	003	3	
2	127	BR	Branch to subroutine - to calculate temperature
3	067	IND/SYMB	
4	022	-	
5	061	PRINT A	Print the answer
6	176		Print a dot line
7	001	1	
8	001	1	
9	111	↑( )	Add 11 to scratch pad no. 9 and store in the pointer
0740	021	+	
1	011	9	
2	110	↓( )	
3	012	.	
4	126	JU	Jump to subroutine
5	067	IND/SYMB	
6	031		
7	066	IND/SYMB	Subroutine 1/x to reverse the current in thermometers
8	054	1/x	
9	266	LDIX	

DECIMAL STEP	INSTRUCTION CODE	INSTRUCTION MNEMONIC	COMMENTS
0550	202		
1	314	OPCB	
2	266	LDIX	Reverse the current in R1 and R2
3	126		
4	315	OPDB	
5	003	3	Wait 3 seconds
6	107	WAIT	
7	001	1	Read the voltage
8	106	READ	
9	110	↓()	Store in scratch pad no. 5
0560	005	5	
1	266	LDIX	
2	202		Get slot no. 2
3	314	OPCB	
4	266	LDIX	
5	125		Reverse the current in R3
6	315	OPDB	
7	003	3	
8	107	WAIT	Wait 3 seconds
9	001	1	
0570	106	READ	Read the voltage
1	111	↑()	
2	022	-	
3	005	5	
4	024	÷	
5	002	2	

DECIMAL STEP	INSTRUCTION CODE	INSTRUCTION MNEMONIC	COMMENTS
0576	020	=	
7	110	↓( )	End of subroutine 1/x
8	005	5	
9	057	RESUME	
0580	066	IND/SYMB	Start of the main program (i.e. subroutine)
1	030		
2	056	HALT	
3	001	1	Start from channel one
4	110	↓( )	
5	011	9	
6	110	↓( )	
7	012	.	
8	004	4	
9	001	1	
0590	000	0	Store channel selector in scratch pad no. 4
1	110	↓( )	
2	004	4	
3	006	6	Choose channel 6 as the last one to scan in the first round
4	110	↓( )	
5	003	3	
6	110	↓( )	
7	005	5	
8	127	BR	Branch to subroutine scan (i.e. sin^{-1})
9	067	IND/SYMB	
0600	071	Sin^{-1}	
1	266	LDIX	Get slot no.2

DECIMAL STEP	INSTRUCTION CODE	INSTRUCTION MNEMONIC	COMMENTS
0602	202		
3	314	OPCB	Output a control byte
4	266	LDIX	
5	063		Load the latch of sample heater
6	315	OPDB	
7	111	↑( )	
8	000	0	
9	127	BR	Branch to subroutine "CL"
0610	067	IND/SYMB	
1	063	CLEAR	
2	266	LDIX	
3	202		
4	314	OPCB	Output control byte
5	266	LDIX	
6	062		Turn sample heater on
7	315	OPDB	
8	003	3	
9	110	↓( )	Store channel 3 in scratch pad 9 and pointer
0620	011	9	
1	110	↓( )	
2	012	.	
3	004	4	
4	001	1	
5	000	0	
6	110	↓( )	
7	004	4	
8	011	9	
9	110	↓( )	

DECIMAL STEP	INSTRUCTION CODE	INSTRUCTION MNEMONIC	COMMENTS
0630	003	3	
1	110	↓( )	
2	005	5	
3	005	5	Wait 5 seconds
4	107	WAIT	
5	127	BR	Branch to sub - routine scan
6	067	IND/SYMB	
7	071	Sin^{-1}	
8	266	LDIX	
9	202		Get slot no.2
0640	314	OPCB	
1	266	LDIX	
2	061		Turn the sample heater off
3	315	OPDB	
4	005	5	
5	007	7	
6	110	↓( )	
7	012	.	
8	004	4	Get the coeffi- cients of R1
9	011	9	
0650	110	↓( )	
1	002	2	
2	121	↑( )( )	Get R1 from main data register 84
3	010	8	
4	004	4	

DECIMAL STEP	INSTRUCTION CODE	INSTRUCTION MNEMONIC	COMMENTS
0655	127	BR	Branch to subroutine - to calcu -
6	067	IND/SYMB	late T for R1
7	022	-	
8	054	1/x	
9	121	↑()()	
0660	023	X	
1	010	8	
2	004	4	
3	110	↓()	
4	005	5	
5	005	5	
6	007	7	Store 57 in pointer
7	110	↓()	
8	012	.	
9	005	5	Store 50 in scratch pad no. 2
0670	000	0	
1	110	↓()	
2	002	2	
3	121	↑()()	Get main data register no. 84
4	010	8	
5	004	4	
6	127	BR	Branch to subroutine "+" to calculate the slop of thermometers
7	067	IND/SYMB	
8	021	+	
9	111	↑()	

DECIMAL STEP	INSTRUCTION CODE	INSTRUCTION MNEMONIC	COMMENTS
0690	023	X	
1	005	5	
2	120	↓()()	
3	010	8	
4	000	0	
5	006	6	
6	006	6	Store 66 in pointer
7	110	↓()	
8	012	.	
9	005	5	
0690	010	8	Store 58 in scratch pad no. 2
1	110	↓()	
2	002	2	
3	121	↑()()	Get R2
4	010	8	
5	005	5	
6	127	BR	Branch to subroutine "-"
7	067	IND/SYMB	
8	022	-	
9	054	1/x	
0700	121	↑()()	
1	023	X	
2	010	8	
3	005	5	
4	110	↓()	
5	005	5	

DECIMAL STEP	INSTRUCTION CODE	INSTRUCTION MNEMONIC	COMMENTS
0706	006	6	
7	006	6	Store 66 in the pointer
8	110	↓()	
9	012	.	
0710	005	5	
1	011	9	
2	110	↓()	
3	002	2	
4	121	↑()()	Get the coeffi-
5	010	8	cients A_i for R2
6	005	5	
7	127	BR	Branch to subrou-
8	067	IND/SYMB	tine "+"
9	021	+	
0720	111	↑()	
1	023	X	
2	005	5	
3	120	↓()()	Store slope of R2
4	010	8	in main data re-
5	001	1	gister 81
6	023	X	
7	121	↑()()	
8	001	1	
9	005	5	
0730	023	X	Get main data re-
1	026	(	gister 15, to cal- culate alpha

DECIMAL STEP	INSTRUCTION CODE	INSTRUCTION MNEMONIC	COMMENTS
0732	014	EXP	
3	005	5	
4	024	÷	
5	026	(	
6	014	EXP	
7	005	5	
8	021	+	
9	121	↑()()	
0740	010	8	
1	004	4	
2	027	)	
3	027	)	
4	020	=	Store alpha in scratch pad 5
5	110	↓()	
6	005	5	
7	121	↑()()	Get $\frac{\partial R1}{\partial T}$
8	010	8	
9	000	0	
0750	023	X	
1	121	↑()()	
2	001	1	Calculate beta
3	003	3	
4	023	X	
5	026	(	
6	014	EXP	
7	005	5	

DECIMAL STEP	INSTRUCTION CODE	INSTRUCTION MNEMONIC	COMMENTS
0758	024	÷	
9	026	(	
0760	014	EXP	
1	005	5	
2	021	+	
3	121	↑()()	Get R2
4	010	8	
5	005	5	
6	027	)	
7	027	)	
8	021	+	
9	111	↑()	Calculate A*
0770	005	5	
1	024	÷	
2	002	2	
3	024	÷	
4	014	EXP	
5	006	6	
6	020	=	
7	045	X	Store A* in main data register 82
8	120	↓()()	
9	010	8	
0780	002	2	
1	266	LDIX	
2	202		Get slot no.2
3	314	OPCB	Output control byte

DECIMAL STEP	INSTRUCTION CODE	INSTRUCTION MNEMONIC	COMMENTS
0784	266	LDIX	
5	026		Load counter on auxiliary heater
6	315	OPDB	
7	000	0	
8	111	↑( )	
9	021	+	
0790	000	0	
1	127	BR	Branch to subroutine "CL"
2	067	IND/SYMB	
3	063	CLEAR	
4	266	LDIX	
5	202		Get slot no. 2
6	314	OPCB	
7	266	LDIX	
8	030		Select the counter on auxiliary heater
9	315	OPDB	
0800	266	LDIX	
1	202		Get slot no. 2
2	314	OPCB	
3	266	LDIX	
4	022		Turn the auxiliary heater on
5	315	OPDB	
6	004	4	
7	001	1	
8	006	6	
9	127	BR	Branch to subroutine A^X to choose the channel and the range

DECIMAL STEP	INSTRUCTION CODE	INSTRUCTION MNEMONIC	COMMENTS
0810	067	IND/SYMB	
1	025	A^x	
2	011	9	
3	110	↓( )	
4	004	4	
5	066	IND/SYMB	Symnolic address
6	116		
7	127	BR	Branch to subroutine 1/x to reverse the current in R1, R2 and R3
8	067	IND/SYMB	
9	054	1/x	
0820	121	↑( )( )	
1	022	-	
2	001	1	
3	006	6	
4	126	JU	Routin to adjust the temperature
5	022	-	
6	067	IND/SYMB	
7	060	PRINT X	
8	111	↑( )	
9	005	5	
0830	022	-	
1	121	↑( )( )	
2	001	1	
3	006	6	
4	022	-	
5	121	↑( )( )	
6	010	8	

DECIMAL STEP	INSTRUCTION CODE	INSTRUCTION MNEMONIC	COMMENTS
0837	007	7	Check the error in temperature
8	020	=	
9	126	JU	
0840	022	-	If there is no error, go to ad-
1	067	IND/SYMB	dress "PRINTA"
2	061	PRINT A	
3	266	LDIX	
4	202		Get slot no. 2
5	314	OPCB	
6	266	LDIX	
7	041		Counter up(i.e. increase the tem-
8	315	OPDB	perature)
9	126	JU	Go to address
0850	067	IND/SYMB	
1	116		
2	066	IND/SYMB	Symbolic address "PRINTX"
3	060	PRINT X	
4	266	LDIX	
5	202		Get slot no. 2
6	314	OPCB	
7	266	LDIX	
8	042		Count douwn(i.e. decrease heat)
9	315	OPDB	
0860	126	JU	Go to address
1	067	IND/SYMB	
2	116		
3	066	IND/SYMB	Symbolic address "PRINTX"

DECIMAL STEP	INSTRUCTION CODE	INSTRUCTION MNEMONIC	COMMENTS
0864	061	PRINT A	
5	266	LDIX	
6	202		Get slot no. 2
7	314	OPCB	Output control byte
8	266	LDIX	
9	043		Advance divider
0870	315	OPDB	Output data byte
1	127	BR	Branch to subroutine "1/x" to reverse the current
2	067	IND/SYMB	
3	054	1/x	
4	121	↑()()	
5	022	-	
6	001	1	
7	006	6	
8	022	-	
9	121	↑()()	Check for temperature to be controlled to best stability
0880	010	8	
1	010	8	
2	020	=	
3	126	JU	If control is ok then go to address π
4	022	-	
5	067	IND/SYMB	
6	015	π	
7	111	↑()	
8	004	4	
9	152		Increament scratch pad no. 4

DECIMAL STEP	INSTRUCTION CODE	INSTRUCTION MNEMONIC	COMMENTS
0890	110	↓( )	
1	004	4	
2	126	JU	If temperature is checked go to address "PRINTA"
3	021	+	
4	067	IND/SYMB	
5	061	PRINT A	
6	126	JU	Go to address
7	067	IND/SYMB	
8	116		
9	066	IND/SYMB	Symbolic address π
0900	015	π	
1	002	2	
2	001	1	
3	110	↓( )	
4	011	9	
5	110	↓( )	
6	012	.	
7	003	3	
8	011	9	
9	000	0	Store 390 in scratch pad no.4
0910	110	↓( )	
1	004	4	
2	002	2	
3	007	7	Store 427 in scratch pad no. 3
4	110	↓( )	

DECIMAL STEP	INSTRUCTION CODE	INSTRUCTION MNEMONIC	COMMENTS
0915	003	3	
6	007	7	
7	110	↓()	Store 7 in scratch pad no.5
8	005	5	
9	127	BR	Branch to subroutine scan
0920	067	IND/SYMB	
1	071	Sin^{-1}	
2	266	LDIX	
3	202		Get slot no.2
4	314	OPCB	
5	266	LDIX	
6	021		Turn auxiliary heater off
7	315	OPDB	
8	266	LDIX	
9	202		Get slot no.2
0930	314	OPCB	
1	266	LDIX	
2	044		Reset the divider
3	315	OPDB	
4	121	↑()()	
5	003	3	
6	007	7	
7	121	↑()()	
8	022	-	
9	001	1	

DECIMAL STEP	INSTRUCTION CODE	INSTRUCTION MNEMONIC	COMMENTS
0940	007	7	Calculate V
1	045	X	
2	060	PRINT X	Print V
3	121	↑()()	
4	024	÷	
5	010	8	Calculate T
6	002	2	
7	060	PRINT X	Print T in mK
8	054	1/x	
9	121	↑()()	
0950	023	X	Get the heat current
1	010	8	
2	006	6	
3	121	↑()()	Get 1/A for the sample
4	023	X	
5	011	9	
6	000	0	Calculate and print thermal conductivity
7	061	PRINT A	
8	065	ADV	Advance the paper
9	126	JU	
0960	067	IND/SYMB	Go to the beginning of the progrm.
1	030		
2	066	IND/SYMB	
3	021	+	Subroutine to calculate $\frac{R}{T}$
4	050	ln	
5	110	↓()	
6	006	6	

DECIMAL STEP	INSTRUCTION CODE	INSTRUCTION MNEMONIC	COMMENTS
0967	010	8	
8	110	↓()	
9	004	4	
0970	121	↑()()	
1	067	IND/SYMB	
2	111	↑()	
3	023	X	
4	004	4	
5	110	↓()	
6	001	1	
7	066	IND/SYMB	Symbolic address "$\dot{\dot{\cdot}}$"
8	024	$\dot{\dot{\cdot}}$	
9	111	↑()	
0980	001	1	
1	111	↑()	
2	023	X	
3	006	6	
4	110	↓()	
5	010	8	
6	001	1	
7	013	CH.SIGN	
8	113		Decreament pointer
9	012	.	
0990	113		Increament scratch pad no. 4
1	004	4	

DECIMAL STEP	INSTRUCTION CODE	INSTRUCTION MNEMONIC	COMMENTS
0992	121	↑( )( )	
3	067	IND/SYMB	
4	111	↑( )	
5	023	X	
6	004	4	
7	111	↑( )	
8	021	+	
9	010	8	
1000	110	↓( )	
1	001	1	
2	111	↑( )	
3	012	.	
4	111	↑( )	
5	022	-	
6	002	2	
7	126	JU	If the condition satisfies, go to
8	021	+	subroutine" "
9	067	IND/SYMB	
1010	024	÷	
1	111	↑( )	
2	001	1	
3	054	1/x	Go to branch print
4	057	RESUME	

APPENDIX 2

To carry out the expansion of the strain Hamiltonian in terms of the strain components, the angular momentum operators $\overline{J}_\alpha$ (A.1)

$$J_1 = \begin{bmatrix} 0 & \frac{\sqrt{3}}{2} & 0 & 0 \\ \frac{\sqrt{3}}{2} & 0 & 1 & 0 \\ 0 & 1 & 0 & \frac{\sqrt{3}}{2} \\ 0 & 0 & \frac{\sqrt{3}}{2} & 0 \end{bmatrix} \qquad J_2 = \begin{bmatrix} 0 & -i\frac{\sqrt{3}}{2} & 0 & 0 \\ -i\frac{\sqrt{3}}{2} & 0 & -i & 0 \\ 0 & i & 0 & -i\frac{\sqrt{3}}{2} \\ 0 & 0 & i\frac{\sqrt{3}}{2} & 0 \end{bmatrix}$$

$$J_3 = \frac{1}{2}\begin{bmatrix} 3 & 0 & 0 & 0 \\ 0 & 1 & 0 & 0 \\ 0 & 0 & -1 & 0 \\ 0 & 0 & 0 & -3 \end{bmatrix} \qquad J^2 = \frac{15}{4}\begin{bmatrix} 1 & 0 & 0 & 0 \\ 0 & 1 & 0 & 0 \\ 0 & 0 & 1 & 0 \\ 0 & 0 & 0 & 1 \end{bmatrix} \qquad (A.1)$$

must be decomposed of J_x, J_y and J_z in a coordinate system with $\alpha = 3$ along $[110]$ (z'-direction). The transformation matrix is obtained by two successive rotations about the z-axis by $\pi/4$ and about x, by $\pi/2$.

$$T = \begin{bmatrix} \frac{\sqrt{2}}{2} & 0 & \frac{\sqrt{2}}{2} \\ -\frac{\sqrt{2}}{2} & 0 & \frac{\sqrt{2}}{2} \\ 0 & -1 & 0 \end{bmatrix} \qquad (A.2)$$

Then for a right-handed cartesian coordinate system, the components of $\overline{J}$ are:

$$J_x = \frac{1}{\sqrt{2}}\begin{bmatrix} \frac{3}{2} & \sqrt{\frac{3}{2}} & 0 & 0 \\ \sqrt{\frac{3}{2}} & \frac{1}{2} & 1 & 0 \\ 0 & 1 & -\frac{1}{2} & \sqrt{\frac{3}{2}} \\ 0 & 0 & \sqrt{\frac{3}{2}} & -\frac{3}{2} \end{bmatrix} \qquad J_y = \frac{1}{\sqrt{2}}\begin{bmatrix} \frac{3}{2} & -\sqrt{\frac{3}{2}} & 0 & 0 \\ -\sqrt{\frac{3}{2}} & \frac{1}{2} & -1 & 0 \\ 0 & -1 & -\frac{1}{2} & -\sqrt{\frac{3}{2}} \\ 0 & 0 & -\sqrt{\frac{3}{2}} & -\frac{3}{2} \end{bmatrix}$$

$$J_z = \begin{bmatrix} 0 & i\sqrt{\frac{3}{2}} & 0 & 0 \\ -i\sqrt{\frac{3}{2}} & 0 & i & 0 \\ 0 & -i & 0 & i\sqrt{\frac{3}{2}} \\ 0 & 0 & -i\sqrt{\frac{3}{2}} & 0 \end{bmatrix} \qquad \text{(A.3)}$$

and J^2 is the same as in (A.1). Hamiltonian (6.11) can be written as:

$$H = \tfrac{2}{3}D_u^a\left[(J_x^2-\tfrac{1}{3}J^2)e_{xx}+(J_y^2-\tfrac{1}{3}J^2)e_{yy}+(J_z^2-\tfrac{1}{3}J^2)e_{zz}\right]+$$

$$\tfrac{1}{3}D_u^a,\left[(J_xJ_y+J_yJ_x)e_{xy}+(J_yJ_z+J_zJ_y)e_{yz}+(J_zJ_x+J_xJ_z)e_{zx}\right] \qquad \text{(A.4)}$$

H was derived by substitution (A.3) in (A.4) and is as in (A.5) overleaf.

As previously mentioned, any strain of lower symmetry than the acceptor ground state when acting on the impurity site will split the quartet level into two Kramers doublet $M_J = \pm 3/2$ and $M_J = \pm \frac{1}{2}$, with the separation, Δ, given by

$$\Delta = \langle \varphi^{3/2} | H_{strain} | \varphi^{3/2} \rangle - \langle \varphi^{\frac{1}{2}} | H_{strain} | \varphi^{\frac{1}{2}} \rangle$$

where $\varphi^{M/J}$ are the wave functions. The matrix element will contain integrals, over all space, of products between the

(A.5)

$$
\begin{bmatrix}
\frac{D_u^a}{6}e_{xx} + \frac{D_u^a}{6}e_{yy} - \frac{D_u^a}{3}e_{zz} + \frac{D_{u'}^a}{2}e_{xy} & \frac{\sqrt{3}}{3}D_u^a e_{xx} - \frac{\sqrt{3}}{3}D_u^a e_{yy} + \frac{\sqrt{3}}{3\sqrt{2}}iD_{u'}^a e_{yz} & \frac{\sqrt{3}}{6}D_u^a e_{xx} + \frac{\sqrt{3}}{6}D_u^a e_{yy} - \frac{\sqrt{3}}{3}D_u^a e_{zz} & 0 \\
 & + \frac{\sqrt{3}}{3\sqrt{2}}iD_{u'}^a e_{zx} & - \frac{\sqrt{3}}{6}D_{u'}^a e_{xy} - \frac{\sqrt{3}}{3\sqrt{2}}iD_{u'}^a e_{yz} + \frac{\sqrt{3}}{3\sqrt{2}}iD_{u'}^a e_{zx} & \\
\frac{\sqrt{3}}{3}D_u^a e_{xx} - \frac{\sqrt{3}}{3}D_u^a e_{yy} - \frac{\sqrt{3}}{3\sqrt{2}}iD_{u'}^a e_{yz} & - \frac{D_u^a}{6}e_{xx} - \frac{D_u^a}{6}e_{yy} + \frac{D_u^a}{3}e_{zz} - \frac{D_{u'}^a}{2}e_{xy} & 0 & \frac{\sqrt{3}}{6}D_u^a e_{xx} + \frac{\sqrt{3}}{6}D_u^a e_{yy} - \frac{\sqrt{3}}{3}D_u^a e_{zz} \\
- \frac{\sqrt{3}}{3\sqrt{2}}iD_{u'}^a e_{zx} & & & - \frac{\sqrt{3}}{6}D_{u'}^a e_{xy} - \frac{\sqrt{3}}{3\sqrt{2}}iD_{u'}^a e_{yz} + \frac{\sqrt{3}}{3\sqrt{2}}iD_{u'}^a e_{zx} \\
\frac{\sqrt{3}}{6}D_u^a e_{xx} + \frac{\sqrt{3}}{6}D_u^a e_{yy} - \frac{\sqrt{3}}{3}D_u^a e_{zz} & 0 & - \frac{D_u^a}{6}e_{xx} - \frac{D_u^a}{6}e_{yy} + \frac{D_u^a}{3}e_{zz} - \frac{D_{u'}^a}{2}e_{xy} & - \frac{\sqrt{3}}{3}D_u^a e_{xx} + \frac{\sqrt{3}}{3}D_u^a e_{yy} - \frac{\sqrt{3}}{3\sqrt{2}}iD_{u'}^a e_{yz} \\
- \frac{\sqrt{3}}{6}D_{u'}^a e_{xy} + \frac{\sqrt{3}}{3\sqrt{2}}iD_{u'}^a e_{yz} - \frac{\sqrt{3}}{3\sqrt{2}}iD_{u'}^a e_{zx} & & & - \frac{\sqrt{3}}{3\sqrt{2}}iD_{u'}^a e_{zx} \\
0 & \frac{\sqrt{3}}{6}D_u^a e_{xx} + \frac{\sqrt{3}}{6}D_u^a e_{yy} - \frac{\sqrt{3}}{3}D_u^a e_{zz} & - \frac{\sqrt{3}}{3}D_u^a e_{xx} + \frac{\sqrt{3}}{3}D_u^a e_{yy} & \frac{D_u^a}{6}e_{xx} + \frac{D_u^a}{6}e_{yy} - \frac{D_u^a}{3}e_{zz} + \frac{D_{u'}^a}{2}e_{xy} \\
 & - \frac{\sqrt{3}}{6}D_{u'}^a e_{xy} + \frac{\sqrt{3}}{3\sqrt{2}}iD_{u'}^a e_{yz} - \frac{\sqrt{3}}{3\sqrt{2}}iD_{u'}^a e_{zx} & + \frac{\sqrt{3}}{3\sqrt{2}}iD_{u'}^a e_{yz} + \frac{\sqrt{3}}{3\sqrt{2}}iD_{u'}^a e_{zx} &
\end{bmatrix}
$$

Expansion of strain hamiltonian in terms of the normal vibrational modes in $[110]$ direction.

various s- and d-like angular parts of the wave functions, their radial parts and the phase factor $e^{i\bar{q}\cdot\bar{r}}$ from the Hamiltonian (A.3). These integrals are quite complicated and involved. However the essential information can be obtained by taking the angular average overall directions of $\bar{q}$ before doing the spatial integrals of the matrix elements. This corresponds to considering:

$$e^{i\bar{q}\cdot\bar{r}} \longrightarrow \frac{\sin 2qr}{qr}$$

The spatial integrals involving the s-like part is unaffected by the above substitution and has the form

$$f = \int d^3r R_o^2 \, e^{i\bar{q}\cdot\bar{r}} = (1 + (qr_1/2)^2)^{-2}$$

The other integrals over a cross product between an s-like and a d-like part are given by reference 18. So with the axis of quantization chosen along the [110] direction the matrix elements can be obtained by

$$\langle n | H_{strain} | n' \rangle = \sum_{qt} \left[\frac{\hbar\omega_{qt}}{2Mv_t^2}\right]^{\frac{1}{2}} (\tfrac{3}{5} D^a_{u'}) (a_{qt} + a^*_{qt}) C^{nn'}_{qt} f(q)$$

where $C^{nn'}_{qt}$ are referred to as coupling parameters, and nn' represent the states $M_J = 3/2, \frac{1}{2}, -\frac{1}{2}, -3/2$.

REFERENCES

1. T.H. Geballe, J. Appl. Phys. 30, 1153 (1959).
2. L.J. Challis, J.D.N. Cheeke, and J.B. Harness, Phil. Mag. 7, 1941 (1962).
3. L.J. Challis, J.D. Cheeke, and D.J. Williams, in Proceedings of the Ninth International Conference on Low Temperature Physics (Plenum, New York, 1965), p.1145.
4. M.G. Holland, Phys. Rev. 134, A471 (1969).
5. V.V. Kosarev, P.V. Tamarin, and S.S. Shalyt, Phys. Stat. Sol. (b) 44, 525 (1971).
6. V.V. Kosarev, Soviet Physics JETP 33, 793 (1971).
7. C.R. Crosby and C.G. Grenier, Phys. Rev. B4, 1258 (1971).
8. J.A. Carruthers, T.H. Geballe, H.M. Rosenberg and J.M. Ziman, Proc. Roy. Soc. (London) A238, 502 (1957).
9. J.A. Carruthers, J.F. Cochran, and K. Mendelssohn, Cryogenics 2, 160 (1962).
10. K. Hilsum and A. Rose-Innes, Semiconducting III-V Compounds, p.75, Pergamon Press (1961).
11. H. Fritzsche and K. Lark-Horovitz, Phys. Rev. 99, 2, 400 (1955).
12. E.O. Kane, J. Phys. Chem. Solids 1, 249.
13. L.J. Challis and L. Halbo, Phys. Rev. Lett. 28, 13, 816 (1972).
14. L.J. Challis, S.C. Haseler and A. Ramadane, J. Phys. C, 11, 4695 (1978).
15. H. Tokumoto and T. Ishiguro, Phys. Rev. B, 15, 2099 (1977).

16. D.N. Nasledov, J. Chim. Phys. 57, 479 (1960).

17. Y. Yafet, R.W. Keyes and E.N. Addams, J. Phys. Chem. Solids 1, 137 (1956).

18. K. Suzuki and N. Mikoshiba, Phys. Rev. B, 3, 8, 2550 (1971).

19. J. Callaway, Phys. Rev. 113, 4, 1046 (1959).

20. R.F. Potter, Phys. Rev. 103, 47 (1956).

21. P. Peierls, Ann. Physik 3, 1055 (1929).

22. D. Huet, B. Pannetier, F.R. La dan and J.P. Maneval, le J. de Phys. 37, 521 (1976).

23. R. Berman, F.E. simon, and J.M. Ziman, Proc. Roy. Soc. (London) 220A, 171 (1953).

24. P.G. Klemens, Proc. Phys. Soc. (London) 68, 1113, (1955).

25. G.A. Slack, Phys. Rev. 126, 427 (1962).

26. P.G. Klemens, in Solid State Physics, vol. 7, edited by F. Seitz and D. Turnball (Academic, New York, 1958), p.1.

27. R.O. Pohl, Phys. Rev. Letts. 8, 481 (1962).

28. R.W. Keyes, Phys. Rev. 122, 1171 (1961).

29. E. Fagen, J.F. Goff and N. Pearlman, Phys. Rev. 94, 1415 (1954).

30. J.M. Ziman, Phil. Mag. 1, 191 (1956); Electrons and Phonons (Oxford U.P., London 1960), pp. 329.

31. A. Sommerfeld, Ann. of Physik 11, 257 (1931); V.A. Yakovlev, Fiz. Tverd. Tela 2, 1624 (1960); 4, 1046 (1962) [Sov. Phys. Solid State 2, 1471 (1961)].

32. J.C. Pyle, Proc. Cambr. Phil. Soc. 53, 508 (1957).

33. G. Weinreich, Solids: Elementary Theory for Advanced Students, (John Wiley and Sons, Inc. New York, 1965).

34. A.K. Betts, Dept. of Physics, Bedford College.

35. G.L. Slonimski, Zh. eksper. teor. Fiz 7, 1457 (1937).

36. R. Orbach and L.A. Vredevoe, Physics 1, 91 (1964).

37. D.R. Frankl and G.J. Campisi, Proc. Int. Conf. Phonon Scattering in Solids, Paris, 1972, p.88.

38. W. Szymanska, J.P. Maneval, Solid State Commun., 8, 879 (1970).

39. J. Bardeen, Phys. Rev. 52, 688 (1937).

40. G. Arlt, P. Quadflieg, Phys. Status Solidi 25, 323 (1968).

41. A. Zawadski, Adv. Phys. 23, 435 (1974).

42. D. Thand, Phys. Stat. Sol. 42, K61 and K65 (1970)

43. W.H. Kleiner and L.M. Roth, Phys. Rev. Lett. 2, 334 (1959).

44. K. Suzuki, M. Okazaki and H. Hasegawa, J. Phys. Soc. Japan 19, 930 (1964).

45. H. Hasegawa, Phys. Rev. 129, 1029 (1963).

46. A. Griffin and P. Carruthers, Phys. Rev. 131, 5, 1976 (1963).

47. A.W. Overhauser and A.M. Graaf, Phys. Rev. Lett. 22, 127 (1969).

48. H. Tokumoto, Electrotechical Laboratory 768 (1976).

49. L.M. Roth and P.N. Argyres, Semiconductors and Semimetals (Academic, New York, 1966), vol. 1, p.159.

50. R.K. Willardson and A.C. Beer, Semiconductors and Semimetals, vol. 1, p.163 (Academic Press, 1966).

51. W. Kohn and D. Schechter, Phys. Rev. 99, 1903 (1955); D. Schechter, J. Phys. Chem. Solid 23, 237 (1962).

52. H. Tokumoto, F. Ishiguro, R. Inaba, K. Kajimura, K. Suzuki, and N. Mikoshiba, Phys. Rev. Lett. 32, 717 (1974).

53. W. Kohn, in Solid State Physics, vol. 5, p. 257 (Academic Press, New York, 1967) edited by F. Seitz and D. Turnbull.

54. K. Suzuki, N. Mikoshiba, Phys. Rev.B4, 2822 (1971).

55. T. Fjeldby, T. Ishiguro and C.Elbaum, Phys. Rev. B7, 1392 (1973); T. Ishiguro, T.A. Fjeldly and C. Elbaum, Phys. Rev. Lett. 27, 667 (1971).

56. L.J. Challis and S.C. Haseler, J. Phys, C, 11, 4681 (1978).

57. A. Baldereschi and N.O. Lipari, Phys. Rev. B, 8, 6, 2697 (1973).

58. F. Raymond, Solid State Comm., 18, 2, 171 (1976).

59, J.M. Luttinger, Phys. Rev. 102, 1030 (1956).

60. N.O. Lipari and A. Baldereschi, Phys. Rev. Lett. 25, 24, 1660 (1970).

61. M. Hass and B.N. Henvis, J. Phys, Chem. Solids, 23, 1099 (1962).

62. D.M. Bagguley, M.L. Robinson and R.A. Stradling, Phys. Lett. 6, 143 (1963).

63. A.K. Bhattachaijee and S. Rodriguez, Phys. Rev. B, 6, 10, 3836 (1972).

64. H. Tokumoto and T. Ishiguro, Phys. Rev. B, 15, 2099 (1977).

65. G.L. Bir, E.J. Butikov, and G.E. Rikus, J. Phys. Chem. Solids, 24, 1467 (1963).

66. W. Kohn and D. Schechter, Phys. Rev. 99, 1903 (1955).

67. D. Schechter, J. Phys. Chem. Solids 23, 237 (1962).

68. S. Zwerdling, K.J. Button, and B. Lax, Phys. Rev. 118, 975 (1960).

69. S. Rodrigues, P. Fisher, and F. Barra, Phys. Rev. B. 5,